

From many-body systems to the one-body force and torque balance equations in and out of equilibrium

Von der Universität Bayreuth
zur Erlangung des Grades eines
Doktors der Naturwissenschaften (Dr. rer. nat.)
genehmigte Abhandlung

von

Johannes Renner

aus Bayreuth

1. Gutachter Prof. Dr. Daniel de las Heras
2. Gutachter Prof. Dr. José Manuel Romero Enrique

Tag der Einreichung: 14.07.2023

Tag des Kolloquiums: 04.10.2023

From many-body systems to the one-body force and torque balance equations in and out of equilibrium

Von der Universität Bayreuth
zur Erlangung des Grades eines
Doktors der Naturwissenschaften (Dr. rer. nat.)
genehmigte Abhandlung

von

Johannes Renner

aus Bayreuth

1. Gutachter Prof. Dr. Daniel de las Heras
2. Gutachter Prof. Dr. José Manuel Romero Enrique

Tag der Einreichung: 14.07.2023

Tag des Kolloquiums: 04.10.2023

Abstract

This theoretical thesis studies many-body systems of interacting particles in and out of equilibrium. To rationalize the physics of many-body systems it is necessary to coarse grain their large number of degrees of freedom. By coarse graining the degrees of freedom of all except one particle, an exact one-body force balance equation resolved in space and in time arises. In systems made of anisotropic particles, the force balance equation is complemented with an exact one-body torque balance equation. The force and the torque balance equations contain several contributions such as internal, external, and transport terms, that together determine the physics of the system at the one-body level. This includes for example the dynamical evolution of the one-body fields, such as the density and the velocity profiles, in non-equilibrium systems.

Using computer simulations we study many-body systems of isotropic and anisotropic particles following Newtonian, Langevin and Brownian dynamics. We sample all terms contributing to the one-body balance equations and use the results to formulate accurate approximations to the unknown contributions, such as the internal force field. Besides this, we also develop computer simulation methods based on the exact one-body force and torque balance equations. These methods allow us to find the external force that generates the desired time evolution, as well as to improve the sampling efficiency of the orientational distribution function in systems of anisotropic particles.

First, we develop a custom flow method for molecular dynamics simulations of isotropic particles. Custom flow is based on the force balance equation and it finds numerically the external force field that generates the desired, prescribed, dynamics of the system. For given space and time resolved density and velocity profiles, custom flow finds iteratively the space and time resolved external force field that generates such one-body kinematic fields. Beyond its practical applications in computer simulations, custom flow also demonstrates numerically the fundamental mapping between the internal force field and the one-body kinematic fields postulated in power functional theory. We demonstrate the validity of the method with several test cases which include a slow-motion dynamics of a non-equilibrium process and the complete prescription of the time evolution between two equilibrium states. We also show that custom flow can be used together with thermostat algorithms designed to control the temperature.

We use custom flow to investigate in detail the unknown contributions to the one-body force balance equation, namely the internal force field and the momentum transport term, the latter is given by the divergence of the kinetic stress tensor. With custom flow we design two model flows: a pure shear flow and a pure bulk (compressible) flow. In both cases the current factorizes into temporal and spatial parts, being the temporal part common to both flows. Moreover, the density profile remains stationary during the whole time evolution. These imposed flow characteristics help us to rationalize and to construct accurate approximations for both the internal force field and the transport term.

We demonstrate that the internal force field contains superadiabatic contributions that are generated by the flow, and are hence genuine non-equilibrium forces. The superadiabatic forces can be split into structural and viscous components, depending on their behaviour upon flow reversal. Moreover, we unambiguously demonstrate that the acceleration field contributes to generate the superadiabatic forces,

in agreement with the predictions of power functional theory. The behaviour of the kinematic stress tensor in non-equilibrium is rather complex. We split it into an idealized term that is generated by the velocity profile only, and an excess term that contains the velocity fluctuations. A detailed analysis shows that the excess term contains also viscous and structural components.

Beyond isotropic systems, we also study systems with orientational degrees of freedom. Based on the one-body torque balance equation for many-body systems of interacting anisotropic particles, we develop a torque sampling method to measure with high efficiency the orientational distribution function in computer simulations. The method samples the torques acting on each particle, and uses them to construct the orientational distribution function via the exact torque balance equation. We demonstrate the advantage of the torque sampling method by testing it against the traditional counting method in several model situations. We consider cases that differ in the overall density, the dimensionality, the type of dynamics, the type of orientational order, and the interparticle interaction potential. In all cases torque sampling delivers better results than the counting method. Moreover, the accuracy in torque sampling is independent of the angular resolution of the bin. Hence, it is possible to sample the orientational distribution function with arbitrarily small angular resolutions.

Kurzfassung

In dieser theoretischen Dissertation untersuchen wir Vielteilchensysteme, bestehend aus miteinander wechselwirkenden Teilchen, im Gleichgewicht und im Nichtgleichgewicht. Um die Physik von Vielteilchensystemen verständlich darzustellen, ist es notwendig die große Anzahl an Freiheitsgraden zu reduzieren. Integriert man über alle Freiheitsgrade bis auf die eines Teilchens, ergibt sich eine exakte Gleichung für das Einteilchenkräftegleichgewicht abhängig von Raum und Zeit. In Systemen mit anisotropen Teilchen ergibt sich zusätzlich zum Kräftegleichgewicht noch eine exakte Gleichung für das Drehmomentengleichgewicht. Die Gleichungen für Kräfte- und Drehmomentengleichgewicht beinhalten mehrere Beiträge, wie interne und externe Terme sowie Transportterme, die zusammen die Physik des Systems auf dem Einteilchenniveau bestimmen. Dies beinhaltet zum Beispiel die Zeitentwicklung der Einteilchenfelder, wie Dichte- und Geschwindigkeitsprofil, in Nichtgleichgewichtssystemen.

Wir verwenden Computersimulationen, um Vielteilchensysteme isotroper und anisotroper Teilchen zu untersuchen. Die Teilchen bewegen sich gemäß Newtonscher, Langevin und Brownscher Dynamik. Wir sampeln alle Terme, die zu den Einteilchengleichgewichtsgleichungen beitragen, und verwenden die Resultate, um genaue Näherungen für die unbekanntten Beiträge zu formulieren, zum Beispiel für das interne Kraftfeld. Desweiteren entwickeln wir Methoden für Computersimulationen basierend auf den Gleichungen fürs Kräfte- und Drehmomentengleichgewicht. Diese Methoden erlauben es uns das externe Kraftfeld zu bestimmen, das eine gewünschte Zeitentwicklung der Dichte und des Stromes generiert, sowie die Samplingeffizienz der Orientierungsverteilungsfunktion in Systemen mit anisotropen Teilchen zu verbessern.

Als Erstes entwickeln wir eine custom flow Methode für Molekulardynamik Simulationen isotroper Teilchen. Custom flow basiert auf der Gleichung fürs Kräftegleichgewicht und findet numerisch das externe Kraftfeld, das die gewünschte Dynamik des Systems generiert. Für gegebene, in Raum und Zeit aufgelöste, Dichte- und Geschwindigkeitsprofile findet custom flow iterativ das zugehörige, in Raum und Zeit aufgelöste, externe Kraftfeld. Über die praktische Anwendung in Computersimulationen hinaus zeigt custom flow numerisch die fundamentale Abbildung zwischen dem internen Kraftfeld und den kinematischen Einteilchenfeldern, welche von der Powerfunktionaltheorie vorausgesagt wird. Wir validieren die Methode mit mehreren Testfällen, welche eine verlangsamte Dynamik eines Nichtgleichgewichtsprozesses und eine komplett vorgeschriebene Zeitentwicklung zwischen zwei Gleichgewichtszuständen beinhaltet. Ferner zeigen wir, dass custom flow zusammen mit Thermostatalgorithmen verwendet werden kann, welche die Temperatur in einem System kontrollieren.

Als Nächstes benutzen wir custom flow, um die unbekanntten Beiträge zum Kräftegleichgewicht detailliert zu untersuchen. Diese Beiträge sind das interne Kraftfeld und der Impulstransportterm, wobei letzterer durch die Divergenz des kinetischen Spannungstensors gegeben ist. Wir designen mit custom flow zwei Modellflüsse: einen reinen Scherfluss und einen reinen kompressiblen Fluss. In beiden Fällen faktorisiert der Strom in einen zeitlichen und einen örtlichen Teil, wobei der zeitliche Teil für beide Flüsse gleich ist. Ferner bleibt das Dichteprofil für die komplette Zeitentwicklung stationär. Diese vorgegebenen Flusseigenschaften helfen uns das interne Kraftfeld und den Transportterm zu verstehen und genaue Näherungen

zu konstruieren.

Wir zeigen, dass das interne Kraftfeld superadiabatische Beiträge beinhaltet, die durch den Fluss erzeugt wurden und daher Nichtgleichgewichtskräfte sind. Abhängig vom Verhalten der superadiabatischen Kräfte bei Flussumkehr können diese in strukturelle und viskose Komponenten aufgespalten werden. Desweiteren zeigen wir eindeutig, dass das Beschleunigungsfeld zur Erzeugung der superadiabatischen Kraft beiträgt, wie von der Powerfunktionaltheorie vorhergesagt. Das Verhalten des kinematischen Spannungstensors ist im Nichtgleichgewicht komplex. Wir teilen ihn in einen faktorierten Term, der nur vom Geschwindigkeitsprofil erzeugt wird, und einen Exzessterm, der die Geschwindigkeitsfluktuationen beinhaltet, auf. Eine detaillierte Analyse zeigt, dass der Exzessterm auch viskose und strukturelle Komponenten enthält.

Über isotrope Systeme hinausgehend betrachten wir Systeme mit Orientierungsfreiheitsgraden. Basierend auf der Einteilchengleichung fürs Drehmomentengleichgewicht von Vielteilchensystemen wechselwirkender anisotroper Teilchen entwickeln wir eine Samplingmethode, um die Orientierungsverteilungsfunktion mit hoher Effizienz in Computersimulationen zu messen. Die Methode sampled die auf jedes Teilchen wirkenden Drehmomente und nutzt sie, um die Orientierungsverteilungsfunktion mithilfe der Gleichung fürs Drehmomentengleichgewicht zu berechnen. Wir zeigen die Vorteile der auf Drehmomente basierenden Samplingmethode auf, indem wir sie mit der traditionellen Zählmethode für mehrere Modellsituationen vergleichen. Wir betrachten Fälle, die sich in der Dichte, der Dimensionalität, der Art der Dynamik, der Orientierungsordnung und dem Wechselwirkungspotential unterscheiden. In allen Fällen liefert die auf Drehmomenten basierte Samplingmethode bessere Resultate als die Zählmethode. Ferner hängt erstere nicht von der Winkelauflösung des Rasters ab, was es ermöglicht die Orientierungsverteilungsfunktion mit beliebig kleinem Winkelabstand zu sampeln.

Contents

1	Introduction	1
1.1	One-body description of many-body systems	1
1.1.1	Anisotropic particles	1
1.1.2	Many-body dynamics	3
1.1.3	From many-body equations of motion to one-body force and torque balance equations	5
1.1.4	Navier-Stokes equation	9
1.1.5	Power functional theory	11
1.2	Theoretical approaches and simulation techniques in many-body systems	13
1.2.1	Force sampling methods with reduced variance	13
1.2.2	Custom flow	15
1.2.3	Memory effects	17
1.2.4	Thermostats	18
2	Overview of the publications	20
2.1	Custom flow in molecular dynamics	21
2.2	Shear and bulk acceleration viscosities in simple fluids	21
2.3	Reduced-variance orientational distribution functions from torque sampling	22
2.4	Outlook	23
2.5	Author contributions	26
	Bibliography	27
3	Publications	34
	Custom flow in molecular dynamics	35
	Shear and bulk acceleration viscosities in simple fluids	47
	Reduced-variance orientational distribution functions from torque sampling	61
	Appendices	74
A	Derivation of the one-body force balance equation	74
B	Derivation of the one-body torque balance equation	75
C	Inertia tensor of anisotropic particles	75

1 Introduction

To understand the physics of many-body systems it is necessary to reduce the amount of information provided by the huge number of degrees of freedom of the system. By integrating out over the degrees of freedom of all but one particle, it is possible to formulate exact one-body force and torque balance equations. These balance equations can then be used to understand the equilibrium and dynamical properties of many-body systems at the one-body level.

This thesis is devoted to the study of many-body systems of interacting particles at the one-body level. We develop methods based on the one-body force and torque balance equations. In particular, custom flow for molecular dynamics (MD) [1, 2] and reduced variance sampling of the orientational distribution function [3]. The methods help us to analyse the internal interactions and transport processes on the one-body level, including memory effects [2, 4].

This introductory chapter starts by discussing the many-body dynamics of isotropic and anisotropic particles. We show how to integrate out degrees of freedom to reduce the description of the system to one-body fields that are governed by exact force and torque balance equations. We also summarize the alternative approach of continuum mechanics, which uses symmetry arguments and approximations to obtain the relevant one-body equations of motion. One goal of this work is to describe the one-body dynamics using the framework of power functional theory [5], which we introduce in this chapter. Furthermore, several methods and techniques related to the work done in this thesis are also described. We recapitulate force sampling methods with reduced variance [6, 7], and explain the custom flow method for Brownian dynamics [8]. We also discuss memory effects in various frameworks, and introduce briefly the role of thermostats in many-body computer simulations.

1.1 One-body description of many-body systems

1.1.1 Anisotropic particles

In order to understand and theoretically describe a physical system, one needs to isolate the relevant physical effects and find the corresponding variables that generate and control those effects. Therefore, it is advisable to start with a simple model of the system and identify its basic effects. To later reach an accurate and realistic description, one can add properties to the basic model and check its agreement with the real physical system.

The simplest type of interacting particles are isotropic particles, i.e. particles with spherical symmetry, that interact with each other based solely on their relative distance. In Refs. [1, 2] we investigate many-body systems of isotropic particles interacting via the Weeks-Chandler-Andersen potential [9], i.e. only the repulsive interaction of the Lennard-Jones potential. Even this, arguably simple, particle model creates complex dynamical behaviour on the one-body level. In nature, most particles additionally interact with each other depending also on their relative orientation. Examples range from relatively simple molecules such as water and air molecules (excluding inert gases) to complex proteins and liquid crystals. Therefore, it is necessary to go beyond simple (isotropic) particle models and develop the appropriate theoretical descriptions and methods by incorporating the orientational degrees of freedom of the system [3].

Particle anisotropy plays a major role in colloidal science. In Fig. 1 several

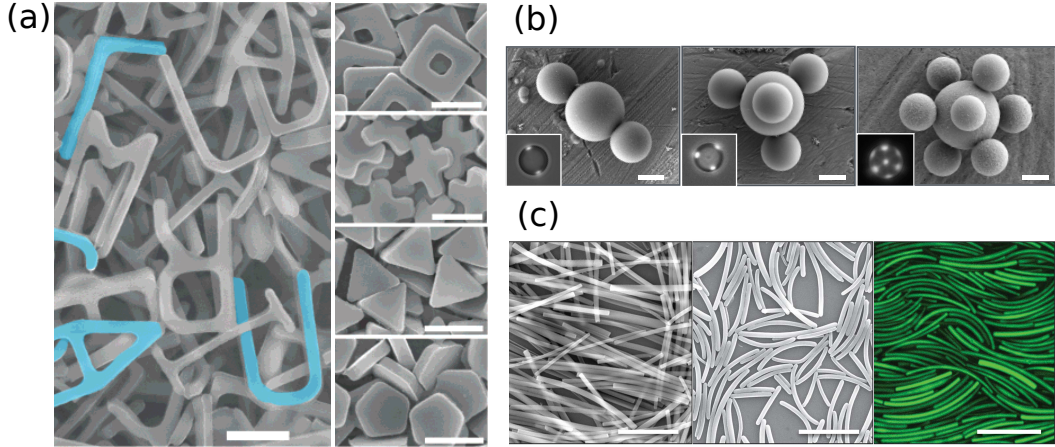


Figure 1: (a) Colloidal particles of different shapes created with photo lithography. The white scale bar indicates a length of $3\ \mu\text{m}$. Adapted with permission from Ref. [19]. Copyright © 2007 American Chemical Society. (b) Patchy colloids with multiple interaction sites created with colloidal fusion. The white scale bar indicates a length of $1\ \mu\text{m}$. The insets show the fluorescent patches of the particles. Reproduced with permission from Ref. [20]. Copyright © 2017 Springer Nature. (c) Different stages of producing banana shaped colloidal particles. The white scale bar indicates a length of $10\ \mu\text{m}$. Reprinted with permission from Ref. [21]. Copyright © 2020 AAAS.

examples of anisotropic colloidal particles are shown. The microscopic interaction potential determines the collective behaviour such as the self assembly of colloidal particles [10]. The interaction between colloidal particles can be anisotropic due to the particle shape, see e.g. Fig. 1 (a) and (c), but also due to directional bonding, see Fig. 1 (b). One example of the latter are patchy colloids. These are particles with designated sites on their surface, called patches, through which patchy colloids interact with each other. An overview of different types and models is given in Ref. [11]. Patchy colloids can be used to construct simple models for water [12] or silica [13]. The particle core can be represented by a hard sphere and the interaction sites for hydrogen or valence bonds are patches on the surface with the respective geometry. Another example of anisotropic particles are proteins, which have complicated structures built of hundreds of amino acids. It is very time consuming to simulate the structures formed by the vast amount of occurring proteins. Instead, one can use simple models by approximating the shape of the protein as a hard body and the interaction sites with patches [14, 15].

Another important class of anisotropically shaped particles are liquid crystals which often possess a rich phase behaviour [16]. Liquid crystal particles can have either an elongated or a disk-like shape. They form several bulk phases characterized by their positional and orientational order. In a nematic phase, for example, the particles exhibit orientational order while having no positional order. In a smectic phase there is orientational order and additionally positional order in one spatial dimension along which the particles form layers. Liquid crystals have several applications as displays [17] and in pharmacy as drug delivery systems [18].

In hard systems, the structure formed is purely determined by the shape of the particles. For example, in Ref. [22] the optimal packing of superdisks is investigated. Superdisks are described by $|x_1|^{2d} + |x_2|^{2d} \leq 1$ with the coordinates x_i and the

deformation parameter d (for circles $d = 1$). Ref. [23] investigates the highest packing fraction of Platonic and Archimedean solids. Hard kites form orientationally ordered phases with different symmetries of the orientation field depending on the packing fraction and their interior angles [24]. A 2d fluid of hard right isosceles triangles self assembles into larger clusters forming liquid-crystal phases with tetratic and octatic ordering [25, 26].

1.1.2 Many-body dynamics

In this thesis, we make use of three many-body simulation techniques: molecular dynamics (MD), Langevin dynamics (LD), and over-damped Brownian dynamics (BD). In the following we summarize each technique and provide their respective many-body equations of motion.

Molecular dynamics. In MD, a system of N anisotropic particles with uniaxial symmetry (i.e. the particles are rotationally symmetric around an orientational unit vector \mathbf{u}) with mass m and inertia tensor \mathbf{I} is characterized by the Hamiltonian H given by

$$\mathcal{H}(\mathbf{r}^N, \mathbf{p}^N, \mathbf{u}^N, \mathbf{p}^{\mathbf{u},N}) = \sum_i \left[\frac{1}{2m} \mathbf{p}_i^2 + \frac{1}{2} \mathbf{p}_i^{\mathbf{u}} \cdot \mathbf{I}^{-1} \cdot \mathbf{p}_i^{\mathbf{u}} + V_{\text{ext}}(\mathbf{r}_i, \mathbf{u}_i) \right] + U(\mathbf{r}^N, \mathbf{u}^N). \quad (1)$$

Here, the sum runs over all particles in the system with \mathbf{r}_i and \mathbf{p}_i the position and the momentum of particle i , respectively. Furthermore, \mathbf{u}_i and $\mathbf{p}_i^{\mathbf{u}}$ are the orientation vector and the canonical angular momentum of particle i , respectively. The canonical angular momentum is given by

$$\mathbf{p}_i^{\mathbf{u}} = \dot{\mathbf{u}}_i \cdot \mathbf{I}. \quad (2)$$

The angular velocity of particle i is given by

$$\boldsymbol{\omega}_i = \mathbf{u}_i \times \dot{\mathbf{u}}_i. \quad (3)$$

The overdot indicates a time derivative. Calculating the cross product $\boldsymbol{\omega}_i \times \mathbf{u}_i$ using Eq. (3) and exploiting the Graßmann identity with $\mathbf{u}_i \cdot \dot{\mathbf{u}}_i = 0$ (which follows from the vanishing time derivative of $\mathbf{u}_i \cdot \mathbf{u}_i = 1$) we obtain

$$\dot{\mathbf{u}}_i = \boldsymbol{\omega}_i \times \mathbf{u}_i. \quad (4)$$

The external potential V_{ext} and the total potential energy U in Eq. (1) depend in general on both position and orientation. We use here the shorthand notation for positions $\mathbf{r}^N = \mathbf{r}_1, \mathbf{r}_2, \dots, \mathbf{r}_N$ and for orientations $\mathbf{u}^N = \mathbf{u}_1, \mathbf{u}_2, \dots, \mathbf{u}_N$. A detailed derivation of the Hamiltonian and the angular canonical momentum exploiting the rotational symmetry around \mathbf{u}_i is provided in Appendix C.

Hamilton's equation of motion for the spatial degrees of freedom are then given by

$$\frac{\partial \mathcal{H}}{\partial \mathbf{r}_i} = -\frac{d\mathbf{p}_i}{dt}, \quad (5)$$

$$\frac{\partial \mathcal{H}}{\partial \mathbf{p}_i} = \frac{d\mathbf{r}_i}{dt}. \quad (6)$$

Hence, using the Hamiltonian in Eq. (1) we obtain the translational equations of motion for particle i

$$\dot{\mathbf{r}}_i = \frac{\mathbf{P}_i}{m}, \quad (7)$$

$$\dot{\mathbf{p}}_i = \mathbf{f}_i, \quad (8)$$

with $\mathbf{f}_i = -\nabla_i(V_{\text{ext}} + U)$ the force on particle i due to external $-\nabla_i V_{\text{ext}}$ and internal $-\nabla_i U$ contributions. Here, ∇_i denotes the derivative with respect to \mathbf{r}_i . Hamilton's equation of motion for the orientational degrees of freedom are given by

$$\frac{\partial \mathcal{H}}{\partial \mathbf{u}_i} = -\frac{d\mathbf{p}_i^{\mathbf{u}}}{dt}, \quad (9)$$

$$\frac{\partial \mathcal{H}}{\partial \mathbf{p}_i^{\mathbf{u}}} = \frac{d\mathbf{u}_i}{dt}. \quad (10)$$

Calculating the corresponding derivatives in Eqs. (9) and (10) and multiplying by $\mathbf{u}_i \times$, we arrive at the equations of motion for the orientational degrees of freedom

$$\mathbf{u}_i \times \dot{\mathbf{p}}_i^{\mathbf{u}} = \mathbf{t}_i, \quad (11)$$

$$\mathbf{u}_i \times \mathbf{p}_i^{\mathbf{u}} = \mathbf{I} \cdot \boldsymbol{\omega}_i, \quad (12)$$

with $\mathbf{t}_i = -\mathbf{u}_i \times \nabla_{\mathbf{u}_i}(V_{\text{ext}} + U)$ the torque on particle i due to external and internal contributions. Here, $\nabla_{\mathbf{u}_i}$ is the nabla operator acting on the components of the orientation vector \mathbf{u}_i of particle i . Note that the angular momentum $\mathbf{L}_i = \mathbf{u}_i \times \mathbf{p}_i^{\mathbf{u}}$ is perpendicular to the canonical angular momentum. We focus here on rotationally symmetric particles around an axis \mathbf{u}_i . In Ref. [27] a general derivation of the equations of motion for a rigid body with arbitrary shape is given. In molecular dynamics, the particles are not subject to friction or stochastic processes and therefore follow deterministic trajectories. In Refs. [1, 2, 4] we use the velocity-Verlet algorithm [28] to propagate the particles in time and space according to the many-body equations of motion.

Langevin dynamics. LD can be viewed as an extension of MD. The particles are immersed in a solvent that is only implicitly described by a friction force and a stochastic force. The equation of motion for the translational degrees of freedom of the i -th particle in LD is

$$m\dot{\mathbf{v}}_i = \mathbf{f}_i - \gamma\mathbf{v}_i + \mathbf{f}_i^{\text{rand}}, \quad (13)$$

with γ the translational friction coefficient against the implicit solvent and $\mathbf{f}_i^{\text{rand}}$ the stochastic force that models collisions between the particles and the molecules of the solvent. Here, we choose a scalar γ independent of the orientation since we use LD only in equilibrium situations. If one is also interested in dynamical properties, the friction can be generalized to a second rank tensor that depends on the particle orientation.

For the orientational degrees of freedom we obtain for particle i the equation of motion

$$\mathbf{I} \cdot \dot{\boldsymbol{\omega}}_i = \mathbf{t}_i - \gamma_r \boldsymbol{\omega}_i + \mathbf{t}_i^{\text{rand}}, \quad (14)$$

with γ_r the rotational friction coefficient and $\mathbf{t}_i^{\text{rand}}$ a stochastic torque due to the implicit solvent.

Both the stochastic force and torque have no drift and the strength of the fluctuations is determined by fluctuation dissipation theorems [29]:

$$\langle \mathbf{f}_i^{\text{rand}} \rangle = 0, \quad (15)$$

$$\langle \mathbf{f}_i^{\text{rand}} \mathbf{f}_k^{\text{rand}} \rangle = 2\gamma k_B T \delta_{ik} \delta(t - t') \mathbf{1}, \quad (16)$$

$$\langle \mathbf{t}_i^{\text{rand}} \rangle = 0, \quad (17)$$

$$\langle \mathbf{t}_i^{\text{rand}} \mathbf{t}_k^{\text{rand}} \rangle = 2\gamma_r k_B T (\mathbf{1} - \mathbf{u}_i \mathbf{u}_k) \delta_{ik} \delta(t - t'), \quad (18)$$

with t the time, k_B the Boltzmann constant, T absolute temperature, δ_{ik} the Kronecker delta, $\delta(\cdot)$ the Dirac delta distribution, and $\mathbf{1}$ the identity matrix. To numerically evolve the system in time, we use the integrator presented in Ref. [30] which adds friction to the velocity-Verlet algorithm.

Overdamped Brownian dynamics. Starting from LD and taking the overdamped limit, i.e. vanishing inertial forces as compared to frictional forces, yields BD. The equations of motion for the i -th particle are

$$\gamma \mathbf{v}_i = \mathbf{f}_i + \mathbf{f}_i^{\text{rand}}, \quad (19)$$

$$\gamma_r \boldsymbol{\omega}_i = \mathbf{t}_i + \mathbf{t}_i^{\text{rand}}, \quad (20)$$

with the same definitions of the random force and the random torque as those provided in Eqs. (15)-(18). We use the Euler algorithm to propagate the particles according to the many-body equations of motion (19) and (20). Recently, an efficient adaptive BD algorithm has been developed [31].

1.1.3 From many-body equations of motion to one-body force and torque balance equations

At the many-body level we have access to the degrees of freedom of each particle. In order to make sense of such an amount of information, we need to reduce it to a level that we can understand without losing the relevant information to describe the physics. To this end, we focus here on one-body quantities that are defined by averages, see e.g. Ref. [32]. In molecular dynamics, the average is calculated as:

$$\langle \rangle = \int d\mathbf{r}^N \int d\mathbf{p}^N \int d\mathbf{u}^N \int d\mathbf{p}^{\mathbf{u},N} \phi(\mathbf{r}^N, \mathbf{p}^N, \mathbf{u}^N, \mathbf{p}^{\mathbf{u},N}, t), \quad (21)$$

with the integrals spanning the whole phase space and the superscript N denoting all particles, i.e. $d\mathbf{r}^N = d\mathbf{r}_1 d\mathbf{r}_2 \dots d\mathbf{r}_N$. The many-body probability distribution $\phi(\mathbf{r}^N, \mathbf{p}^N, \mathbf{u}^N, \mathbf{p}^{\mathbf{u},N}, t)$ is normalized to one

$$\int d\mathbf{r}^N \int d\mathbf{p}^N \int d\mathbf{u}^N \int d\mathbf{p}^{\mathbf{u},N} \phi(\mathbf{r}^N, \mathbf{p}^N, \mathbf{u}^N, \mathbf{p}^{\mathbf{u},N}, t) = 1. \quad (22)$$

The time evolution of the many-body probability distribution is governed by the Liouville equation

$$\frac{\partial \phi}{\partial t} + \sum_i \left(\frac{\partial \phi}{\partial \mathbf{r}_i} \cdot \dot{\mathbf{r}}_i + \frac{\partial \phi}{\partial \mathbf{p}_i} \cdot \dot{\mathbf{p}}_i + \frac{\partial \phi}{\partial \mathbf{u}_i} \cdot \dot{\mathbf{u}}_i + \frac{\partial \phi}{\partial \mathbf{p}_i^{\mathbf{u}}} \cdot \dot{\mathbf{p}}_i^{\mathbf{u}} \right) = 0. \quad (23)$$

one-body quantity	Q	q_i
density	ρ	1
current	\mathbf{J}	\mathbf{v}_i
angular current	\mathbf{J}_ω	$\boldsymbol{\omega}_i$
kinetic stress tensor	$\boldsymbol{\tau}$	$-m\mathbf{v}_i\mathbf{v}_i$
angular kinetic stress tensor	$\boldsymbol{\tau}_\omega$	$\boldsymbol{\omega}_i\boldsymbol{\omega}_i$
coupling tensor	\mathbf{C}	$\mathbf{v}_i\boldsymbol{\omega}_i$
force density	\mathbf{F}	\mathbf{f}_i
torque density	\mathbf{T}	\mathbf{t}_i
internal force density	\mathbf{F}_{int}	$-\nabla_i U$
external force density	\mathbf{F}_{ext}	$-\nabla_i V_{\text{ext}}$
internal torque density	\mathbf{T}_{int}	$-\hat{\mathbf{R}}_i U$
external torque density	\mathbf{T}_{ext}	$-\hat{\mathbf{R}}_i V_{\text{ext}}$

Table 1: Definition of one-body quantities via Eq. (24). The dyadic product between two vectors \mathbf{a} and \mathbf{b} is indicated by \mathbf{ab} . Note that all one-body quantities $Q(\mathbf{r}, \mathbf{u}, t)$ depend on a generic position \mathbf{r} and orientation \mathbf{u} , as well as explicitly on time.

This gives us the tools to define microscopically resolved one-body quantities via

$$Q(\mathbf{r}, \mathbf{u}, t) = \left\langle \sum_i q_i \delta(\mathbf{r} - \mathbf{r}_i) \delta(\mathbf{u} - \mathbf{u}_i) \right\rangle, \quad (24)$$

with δ the Dirac delta distribution and q_i a generic property of particle i such as its velocity. The resulting one-body quantity has therefore the units of density times the units of q_i . In Table 1 the definitions for several one-body quantities relevant for our work are given. In simulations, the average denoted by $\langle \rangle$ is sampled over different initial microstates (in MD, LD, and BD) and also over different realizations of the thermal noise (in LD and BD). In equilibrium and in steady state, we can also average over time.

From these averages useful balance equations can be constructed. The continuity equation, for example, can be obtained by time deriving the one-body density

$$\dot{\rho}(\mathbf{r}, \mathbf{u}, t) = \left\langle \sum_i \left[\delta(\mathbf{u} - \mathbf{u}_i) \frac{\partial \delta(\mathbf{r} - \mathbf{r}_i)}{\partial(\mathbf{r} - \mathbf{r}_i)} \cdot \frac{d(\mathbf{r} - \mathbf{r}_i)}{dt} + \delta(\mathbf{r} - \mathbf{r}_i) \frac{\partial \delta(\mathbf{u} - \mathbf{u}_i)}{\partial(\mathbf{u} - \mathbf{u}_i)} \cdot \frac{d(\mathbf{u} - \mathbf{u}_i)}{dt} \right] \right\rangle. \quad (25)$$

The generic variables \mathbf{r} and \mathbf{u} do not depend on time. Furthermore, we can rewrite the partial derivatives acting on the Dirac distribution as the Nabla operator ∇ and the differential operator on the unit sphere ∇_u . Hence, we obtain

$$\dot{\rho} = - \left\langle \sum_i \nabla \cdot \delta(\mathbf{r} - \mathbf{r}_i) \delta(\mathbf{u} - \mathbf{u}_i) \mathbf{v}_i \right\rangle - \left\langle \sum_i \dot{\mathbf{u}}_i \cdot \nabla_u \delta(\mathbf{u} - \mathbf{u}_i) \delta(\mathbf{r} - \mathbf{r}_i) \right\rangle. \quad (26)$$

The Nabla operator acting on the generic position \mathbf{r} can be pulled out of the average since the integrals in the average $\langle \rangle$ depend on all particle positions but not on \mathbf{r} . Furthermore, making use of Eq. (4) we arrive at

$$\dot{\rho} = - \nabla \cdot \left\langle \sum_i \delta(\mathbf{r} - \mathbf{r}_i) \delta(\mathbf{u} - \mathbf{u}_i) \mathbf{v}_i \right\rangle - \left\langle \sum_i (\boldsymbol{\omega}_i \times \mathbf{u}_i) \cdot \nabla_u \delta(\mathbf{u} - \mathbf{u}_i) \delta(\mathbf{r} - \mathbf{r}_i) \right\rangle. \quad (27)$$

Using the definition of the current $\mathbf{J}(\mathbf{r}, \mathbf{u}, t)$, see Table 1, and changing the order of the triple dot product yields

$$\dot{\rho} = -\nabla \cdot \mathbf{J} - \left\langle \sum_i (\mathbf{u}_i \times \nabla_u) \cdot \boldsymbol{\omega}_i \delta(\mathbf{u} - \mathbf{u}_i) \delta(\mathbf{r} - \mathbf{r}_i) \right\rangle. \quad (28)$$

Due to the Dirac distribution on the orientations there is only a contribution to the average provided that $\mathbf{u} = \mathbf{u}_i$ and hence, we can pull the rotation operator $\hat{\mathbf{R}} = \mathbf{u} \times \nabla_u$ out of the average and obtain

$$\dot{\rho} = -\nabla \cdot \mathbf{J} - \hat{\mathbf{R}} \cdot \left\langle \sum_i \boldsymbol{\omega}_i \delta(\mathbf{u} - \mathbf{u}_i) \delta(\mathbf{r} - \mathbf{r}_i) \right\rangle. \quad (29)$$

Finally, inserting the definition of the angular current $\mathbf{J}_\omega(\mathbf{r}, \mathbf{u}, t)$, see Table 1, we arrive at the continuity equation

$$\dot{\rho} = -\nabla \cdot \mathbf{J} - \hat{\mathbf{R}} \cdot \mathbf{J}_\omega. \quad (30)$$

We are particularly interested in the one-body force and torque density balance equations. Time deriving the current yields the force density balance equation for MD [5, 33]

$$m\dot{\mathbf{J}} = \mathbf{F}_{\text{ext}} + \mathbf{F}_{\text{int}} + \nabla \cdot \boldsymbol{\tau} - m\hat{\mathbf{R}} \cdot \mathbf{C}. \quad (31)$$

Analogous steps compared to the derivation of the continuity equation need to be performed. A detailed derivation is provided in Appendix A. Here, \mathbf{F}_{ext} is the external force density, \mathbf{F}_{int} is the internal force density, $\boldsymbol{\tau}$ is the kinetic stress tensor, and \mathbf{C} is the coupling tensor, see Table 1.

We split the kinetic stress tensor into a factorized term $\boldsymbol{\tau}_{\text{id}}(\mathbf{r}, \mathbf{u}, t) = -m\mathbf{v}\mathbf{v}\rho$ with the velocity field $\mathbf{v} = \mathbf{J}/\rho$ and the remaining excess contribution $\boldsymbol{\tau}_{\text{exc}}(\mathbf{r}, \mathbf{u}, t) = \boldsymbol{\tau} - \boldsymbol{\tau}_{\text{id}}$. Hence, we can rewrite the force density balance as

$$m\dot{\mathbf{J}} + m\nabla \cdot (\mathbf{v}\mathbf{v}\rho) = \mathbf{F}_{\text{ext}} + \mathbf{F}_{\text{int}} + \nabla \cdot \boldsymbol{\tau}_{\text{exc}} - m\hat{\mathbf{R}} \cdot \mathbf{C}. \quad (32)$$

The force balance equation relates the current to the forces acting on the system and the momentum transport present in the system. The current is obtained by the time integral over the whole history of forces and momentum transport. Note that for anisotropic particles there is in general also a coupling between the momentum and the angular momentum via the coupling tensor \mathbf{C} .

The corresponding one-body torque density balance equation in MD for the orientational degrees of freedom follows by time deriving the angular current [3]

$$\dot{\mathbf{J}}_\omega \cdot \mathbf{I} = \mathbf{T}_{\text{ext}} + \mathbf{T}_{\text{int}} - \nabla_{\mathbf{r}} \cdot \mathbf{C}^t \cdot \mathbf{I} - \hat{\mathbf{R}} \cdot \boldsymbol{\tau}_\omega \cdot \mathbf{I}. \quad (33)$$

A detailed derivation is provided in Appendix B. Here, \mathbf{T}_{ext} is the external torque density, \mathbf{T}_{int} is the internal torque density, and $\boldsymbol{\tau}_\omega$ is the angular kinetic stress tensor, see Table 1. The torque balance equation relates the angular current to the torques acting on the system and the angular momentum transport present in the system. The angular current is obtained by the time integral over the whole history of forces and momentum transport. The angular momentum is coupled to the momentum via the coupling tensor \mathbf{C} .

Equilibrium. Next, we derive the equilibrium one-body force and torque density balance equations starting from the non-equilibrium equations (31) and (33). In equilibrium there is no time dependence. Furthermore, the currents vanish, i.e. $\mathbf{J} = 0$ and $\mathbf{J}_\omega = 0$, and the coupling tensor also vanishes, $\mathbf{C} = 0$, since the velocity and the angular velocity are uncorrelated in equilibrium. Hence, we conclude that in equilibrium

$$0 = \mathbf{F}_{\text{ext}} + \mathbf{F}_{\text{int}} + \nabla \cdot \boldsymbol{\tau}, \quad (34)$$

$$0 = \mathbf{T}_{\text{ext}} + \mathbf{T}_{\text{int}} - \hat{\mathbf{R}} \cdot \boldsymbol{\tau}_\omega \cdot \mathbf{I}. \quad (35)$$

Moreover, in equilibrium it is possible to simplify the momentum and the angular momentum transport terms $\boldsymbol{\tau}$ and $\boldsymbol{\tau}_\omega$, respectively. We use the equipartition theorem [34] given by

$$\left\langle b^j \frac{\partial \mathcal{H}}{\partial b^k} \right\rangle = \delta_{jk} k_B T, \quad (36)$$

with b_j the j -th component of a vector appearing in the Hamiltonian, such as e.g. the momentum and the canonical angular momentum. For finite systems there might be small temperature differences depending on the selected statistical ensemble [35]. Only in the thermodynamic limit the different ensembles lead to identical results. Using the Hamiltonian given in Eq. (1), and the equipartition theorem, Eq. (36), for the components of the momentum

$$\left\langle p^j \frac{\partial \mathcal{H}}{\partial p^k} \right\rangle = \left\langle p^j \frac{p^k}{m} \right\rangle = \quad (37)$$

$$\left\langle m v^j v^k \right\rangle = \delta_{jk} k_B T, \quad (38)$$

and for the canonical angular momentum

$$\left\langle p^{\mathbf{u},j} \frac{\partial \mathcal{H}}{\partial p^{\mathbf{u},k}} \right\rangle = \left\langle \sum_{m=1}^3 p^{\mathbf{u},j} (\Gamma^{km})^{-1} p^{\mathbf{u},m} \right\rangle = \quad (39)$$

$$\left\langle \sum_{m=1}^3 \omega^m \Gamma^{mj} \omega^k \right\rangle = \delta_{jk} k_B T, \quad (40)$$

where we have used the two representations of the rotation energy described in Appendix C. Hence, using Eq. (38) to rewrite the kinetic stress tensor in Eq. (34) we arrive at the equilibrium one-body force density balance equation

$$0 = \mathbf{F}_{\text{ext}} + \mathbf{F}_{\text{int}} - k_B T \nabla \rho. \quad (41)$$

Using Eq. (40) to rewrite the angular kinetic stress tensor in Eq. (35) we obtain the equilibrium one-body torque density balance equation

$$0 = \mathbf{T}_{\text{ext}} + \mathbf{T}_{\text{int}} - k_B T \hat{\mathbf{R}} \rho. \quad (42)$$

Brownian dynamics. In BD, the non-equilibrium one-body force density balance equation is given by [5]

$$\gamma \mathbf{J} = \mathbf{F}_{\text{ext}} + \mathbf{F}_{\text{int}} - k_B T \nabla \rho. \quad (43)$$

Compared to MD, the transport term, $\nabla \cdot \boldsymbol{\tau}$, reduces to the ideal diffusive part, $-k_B T \nabla \rho$, in BD for both equilibrium and non-equilibrium situations.

For orientational degrees of freedom in BD we have additionally the non-equilibrium one-body torque density balance equation [3] given by

$$\gamma_r \mathbf{J}_\omega = \mathbf{T}_{\text{ext}} + \mathbf{T}_{\text{int}} - k_B T \hat{\mathbf{R}} \rho. \quad (44)$$

In MD, the force density balance equation (31) links the forces acting in the system to the time derivative of the current, $m \dot{\mathbf{J}}$. Therefore, the current can be expressed as a time integral over the history of all forces that have acted in the system and shows hence the inertia present in the system. In BD, the force density balance equation (43) links the forces acting in the system to the instantaneous current flowing in the system, \mathbf{J} , via the friction coefficient. The same observation holds for the torque balance equations in MD and BD. Hence, no inertial effects are present in BD systems.

1.1.4 Navier-Stokes equation

Particle-based simulations, like MD, can be used to investigate systems with up to millions of particles [36, 37]. However, the length and time scales accessible in computer simulations of such systems is still small for certain situations, such as for example water flow in a pipe, wind in the atmosphere, and boiling water in a pot. To describe these larger systems a continuum description is valuable. In continuum-based approaches one considers volume elements much larger than the particle length scale. To derive balance equations one exploits conservation laws. For example, mass and momentum conservation lead to the continuity equation and the force balance equation, respectively. In MD we can derive an exact force balance equation (32) that describes conservation of momentum and is based on microscopically resolved one-body fields. These one-body fields are directly accessible in computer simulations and can be used to model the internal force field and the momentum transport.

Both approaches, particle-based and continuum-based, describe the same physics. Hence, the particle-based description of the one-body force balance equation should yield for large length and time scales the corresponding momentum conservation law of the continuum description. The particle-based approach can be used to find new phenomena on small scales that are beyond the continuum description and also to validate existing approximations in the continuum description.

The Navier-Stokes equations are a prominent example of a continuum description. They are used in numerous applications to simulate the time evolution of the coarse-grained velocity and pressure fields of fluids. The air around rotor blades from helicopters [38] and airplane turbines [39] can be studied with the Navier-Stokes equations. Deep learning algorithms were used for analyzing airflow around different shapes of airfoils [40]. Furthermore, gas flow in the context of micro devices [41] and in human lungs [42] was investigated. Water flows were studied for land slides [43], and a dam break [44]. Further examples include the modified Navier-Stokes equations applied to shock waves [45].

The most general form of the force density balance equation in the continuum-based picture is the Cauchy momentum equation. Detailed derivations based on energy balance and symmetry arguments are given in Refs. [46, 47]. The Cauchy momentum equation in its conservation form is given by

$$\frac{\partial}{\partial t}(\tilde{\rho} \tilde{\mathbf{v}}) + \nabla \cdot (\tilde{\rho} \tilde{\mathbf{v}} \tilde{\mathbf{v}}) = \nabla \cdot \tilde{\boldsymbol{\sigma}} + \tilde{\rho} \mathbf{g} \quad (45)$$

with the mass density $\tilde{\rho}$, the velocity field $\tilde{\mathbf{v}}$, the Cauchy stress tensor $\tilde{\boldsymbol{\sigma}}$, and body accelerations \mathbf{g} . The mass density in our one-body description would correspond to $m\rho$ and the body accelerations would be $\mathbf{f}_{\text{ext}}/m$. The velocity fields \mathbf{v} and $\tilde{\mathbf{v}}$ correspond to the same physical fields but our one-body field \mathbf{v} is microscopically resolved in contrast to the coarse grained field $\tilde{\mathbf{v}}$. There are several definitions of the stress tensor in atomistic simulations, which give not necessarily the same results as the Cauchy stress [48].

There are efforts to find a formal link between the many-body description and the continuum description [49]. In Ref. [50] the classical Boltzmann equation is derived as a limiting case of a system of hard spheres following Newtonian dynamics. From this mesoscopic description of the Boltzmann equation of a tagged particle the heat equation can be derived [51].

Comparing the Cauchy momentum equation (45) and the exact one-body force balance equation (32) we observe some similarities. The left hand side of both equations has the same structure. Also on the right hand side the external force density \mathbf{F}_{ext} of Eq. (32) corresponds to $\tilde{\rho}\mathbf{g}$ in Eq. (45). Since both equations express the momentum conservation, $\mathbf{F}_{\text{int}} + \nabla \cdot \boldsymbol{\tau}$ in Eq. (32) corresponds to $\nabla \cdot \tilde{\boldsymbol{\sigma}}$ in Eq. (45). In both approaches their exact forms are unknown. Hence, approximations must be found. In the case of the Cauchy momentum equation, physical assumptions about the Cauchy stress tensor need to be made. In Ref. [52] the following assumptions are made to arrive at the Navier-Stokes equation: (i) the relationship between stress and strain of shear has to be linear, (ii) in isotropic fluids the stress tensor has to be symmetric. Applying these assumptions to the Cauchy stress tensor we obtain

$$\tilde{\boldsymbol{\sigma}} = \mu \left[\nabla \tilde{\mathbf{v}} + (\nabla \tilde{\mathbf{v}})^{\text{t}} - \frac{2}{3} (\nabla \cdot \tilde{\mathbf{v}}) \mathbf{1} \right] - p \mathbf{1} + \xi (\nabla \cdot \tilde{\mathbf{v}}) \mathbf{1}, \quad (46)$$

with μ the dynamic viscosity, ξ the bulk viscosity, p the pressure, and the superscript t indicating the transposition of a second rank tensor. Inserting this expression for the Cauchy stress Eq. (46) into Eq. (45) leads to the well-known Navier-Stokes equation

$$\frac{\partial}{\partial t} (\tilde{\rho} \tilde{\mathbf{v}}) + \nabla \cdot (\tilde{\rho} \tilde{\mathbf{v}} \tilde{\mathbf{v}}) = -\nabla p + \mu \Delta \tilde{\mathbf{v}} + \left(\frac{1}{3} \mu + \xi \right) \nabla (\nabla \cdot \tilde{\mathbf{v}}) + \tilde{\rho} \mathbf{g}. \quad (47)$$

Looking back at the one-body force balance equation (32) we also need to approximate the internal force and the excess kinetic stress tensor. However, in contrast to the continuum approach, we can sample these objects directly in particle-based computer simulations, see Sec. 1.1.3 and use the result to construct accurate approximations.

We perform many-body simulations and sample the internal force directly. As we see below, custom flow allows us to tailor the dynamics and the form of the velocity field [1]. To isolate shear effects, we study a flow with $\nabla \cdot \mathbf{v} = 0$ and $\nabla \times \mathbf{v} \neq 0$ with constant density in time and space. To isolate bulk effects we study a flow with $\nabla \times \mathbf{v} = 0$ and $\nabla \cdot \mathbf{v} \neq 0$ with a density profile constant in time. Our analysis in Ref. [2] revealed that the acceleration field plays an important role in the internal force field. Directly comparing our results with the Navier-Stokes equation is difficult because the length of our system is of the order of a few particle sizes and the volume elements of the coarse grained velocity field in the continuum approaches are on a much larger length scale. It would be interesting to find a formal link between both approaches.

1.1.5 Power functional theory

Density functional theory (DFT) is a well established variational framework to describe inhomogeneous many-body systems in equilibrium. DFT was first introduced for quantum systems [53, 54] and later adapted to classical systems [55]. A widely used extension of DFT to describe time dependent systems is dynamical density functional theory (DDFT) [56, 57]. In DDFT one assumes that the equal-time two-body correlation function out of equilibrium has the same properties as its equilibrium counterpart. This implies that the internal force due to interparticle interactions in non-equilibrium is the same as that of a reference equilibrium system with the same instantaneous density profile as the non-equilibrium system. This constitutes an adiabatic approximation that disregards all the genuine non-equilibrium internal forces, see Ref. [58] for a recent perspective discussing the limitations of DDFT.

Power functional theory (PFT) [33, 59, 60] is a formally exact variational principle able to incorporate the superadiabatic force contributions that go beyond the equilibrium adiabatic contributions. Hence, PFT is formally able to describe non-equilibrium many-body systems accurately. In a recent review by Schmidt [5], PFT and background information is laid out comprehensively.

PFT was first introduced for overdamped Brownian particles [59]. The central object is the power functional $R_t[\rho, \mathbf{J}]$ that depends functionally on the one-body density and on the one-body current profiles. Minimizing the functional

$$\left. \frac{\delta R_t[\rho, \mathbf{J}]}{\delta \mathbf{J}(\mathbf{r}, t)} \right|_{\rho} = 0, \quad (48)$$

with respect to the one-body current \mathbf{J} while keeping the one-body density and the history of both, i.e. at times $t' < t$, unchanged yields the physical density and current fields at the current time t . Setting the functional derivative to zero in Eq. (48) gives by construction the exact one-body force balance equation (43) in BD. The power functional itself can be split into several contributions

$$R_t[\rho, \mathbf{J}] = P_t^{\text{id}} + P_t^{\text{exc}} + \dot{F}_{\text{id}} + \dot{F}_{\text{exc}} - X_t. \quad (49)$$

Here, we find three exact terms: (i) the ideal dissipative intrinsic contribution P_t^{id} related to the friction force against the solvent, (ii) the time derivative of the ideal free energy \dot{F}_{id} responsible for the ideal gas diffusion, and (iii) X_t containing all external contributions. Furthermore, we have two excess terms due to interparticle interactions that are not exactly known and hence need to be approximated. The time derivative of the excess free energy \dot{F}_{exc} relates to the adiabatic, i.e. equilibrium-like, contribution of the interparticle interactions. This contribution has been investigated extensively in the framework of DFT and there are excellent approximations available in the literature, such as for example fundamental measure theory for hard spheres [61]. The remaining contribution P_t^{exc} contains all superadiabatic, i.e. genuine non-equilibrium, contributions due to interparticle interactions. In general, the structure of P_t^{exc} can have a complex dependence on both, ρ and \mathbf{J} , incorporating non-local memory effects in space and time.

In BD simulations, the superadiabatic internal force can be obtained via the adiabatic construction [62]. Using custom flow [8] an equilibrium reference system with the same instantaneous density profile as the non-equilibrium system can be constructed. Subtracting the adiabatic internal force of the reference system from the internal force of the non-equilibrium system yields the superadiabatic force [62]. Using the adiabatic construction, the superadiabatic forces of several non-equilibrium

systems have been investigated. In Ref. [63] a 2d sheared system, investigated on the Focker-Planck level solving numerically the many-body Smoluchowski equation and also using BD simulations, exhibits a superadiabatic viscous internal force working against the flow field and a superadiabatic structural internal force perpendicular to the flow direction sustaining a density gradient. In Ref. [64] a change of variable from $\mathbf{J} \rightarrow \nabla \mathbf{v}$ with respect to the minimization of the power functional was performed. The use of $\nabla \mathbf{v}$ is advantageous since it incorporates by construction the Galilean invariance of the system. Furthermore, an approximation of P_t^{exc} for viscous contributions in the lowest order of the velocity gradient is constructed. In Ref. [65] a 2d system made of two particle species that differ only on their value of the buoyant mass is subject to an external force and exhibits lane formation. This demixing of particles is driven by a superadiabatic structural internal force. The particles exhibit also a superadiabatic viscous internal force working against the flow field. In Ref. [66] a systematic analysis of complex flows reveals that superadiabatic forces can in general be classified as structural and viscous and obtained by many-body simulations. Furthermore, approximations of the power functional based on powers of $\nabla \mathbf{v}$ are constructed.

PFT has been also used to describe the motility induced phase separation of active Brownian particles. In Ref. [67] an approximation for the excess part of the power functional is constructed based on the one-body density and current profiles and is tested against BD simulations. In Ref. [68] PFT is generalized to particles with orientational degrees of freedom and the steady state properties of active Brownian particles are studied. In Refs. [69, 70] the superadiabatic internal force in a system of active Brownian particles is split into four contributions. In particular, a "quiet life" term favors the motility induced phase separation. Furthermore, a self contained theoretical power functional description of the system is provided and compared to BD simulations. Further calculations yield a positive interfacial tension supporting the observed stability of the phase separation [71]. Additionally, sum rules for the interface polarization are proven [72].

Recently, superadiabatic internal forces of a colloidal gel former subject to an external shear force are investigated in the framework of PFT [73] using BD simulations with an efficient adaptive integration scheme [31].

On the two-body level of correlation functions, the van Hove function is an important object. It describes how likely it is to find two particles at different times separated in space by a given vector. Within the framework of PFT for BD, a dynamical test particle theory for the van Hove function of a bulk system consisting of one particle species is developed in Ref. [74]. In Ref. [75] the two-body dynamics of a dense Brownian liquid is investigated and superadiabatic contributions identified. Further investigations of the van Hove function in a hard sphere and Lennard-Jones liquid show also superadiabatic effects that can be theoretically described within the framework of PFT [76, 77].

Recently, Noether's theorem applied to functionals in statistical mechanics yields exact identities from translational and rotational symmetries [78]. Exploiting the symmetries of a classical many-body system yields also sum rules for the global force variance [79]. There is also a quantum mechanical description of PFT [60] in which superadiabatic forces have been shown to contain contributions due to the acceleration field [80].

In this thesis, we are particularly interested in the application of PFT to Newtonian particles [33]. There, the central object is the power rate functional $G_t[\rho, \mathbf{v}, \mathbf{a}]$

that depends functionally on the one-body density, velocity, and acceleration fields. Minimizing the functional

$$\left. \frac{\delta G_t[\rho, \mathbf{v}, \mathbf{a}]}{\delta \mathbf{a}} \right|_{\rho, \mathbf{v}} = 0, \quad (50)$$

with respect to the acceleration field $\mathbf{a} = \dot{\mathbf{v}}$ while keeping the one-body density and velocity fields as well as the history of all three fields constant yields the physical fields, ρ , \mathbf{v} , \mathbf{a} , at the current time. This minimization principle is equivalent to the original one given in Ref. [33] where the dependence is on \mathbf{J} rather than on \mathbf{a} . Furthermore, calculating the functional derivative in Eq. (50) gives by construction the exact one-body force balance equation (31). The power rate functional can be split into three contributions

$$G_t[\rho, \mathbf{v}, \mathbf{a}] = G_t^{\text{id}} + G_t^{\text{exc}} - X_t. \quad (51)$$

Here, G_t^{id} generates via functional differentiation the left hand side of the force balance equation (32). The excess part G_t^{exc} contains all contributions related to interparticle interactions and momentum transport effects of the particle velocities fluctuating around the velocity field \mathbf{v} . The last part, X_t , contains the external contributions. Our work in Ref. [2], which is part of this thesis, makes use of computer simulations to demonstrate that the one-body internal force field, which follows by functional differentiation of G_t^{exc} , depends on the one-body velocity and acceleration fields beside the one-body density. Hence, we validate with particle-based computer simulations that the functional G_t^{exc} carries a dependency on the one-body acceleration field. Furthermore, we give explicit expressions for the viscous internal force and the corresponding functional generator for shear and bulk flows including temporal memory effects.

1.2 Theoretical approaches and simulation techniques in many-body systems

1.2.1 Force sampling methods with reduced variance

This thesis is largely based on results from particle-based computer simulations. With the growth of computational power in the last decades, it has become possible to simulate many physical systems. The widespread use of computer simulations in research makes it necessary to develop efficient algorithms and methods to save time and reduce energy consumption.

Several works have been recently devoted to the development of equilibrium methods to sample one-body quantities (e.g. the density profile) with reduced-variance in particle-based computer simulations. See e.g. the review by Rotenberg [7] that explains the shortcoming of the traditional histogram-based counting methods and presents some alternatives based on sampling the force. The main limitation with the traditional counting of events methodology is illustrated in Fig. 2 for the orientational distribution function. The orientational distribution function describes the probability of finding a particle with a certain orientation. With increasing the number of bins, one needs more sampling steps over different microstates to fill the histograms of the counting method and therefore to obtain an accurate profile for the orientational distribution function.

To the best of our knowledge, the first equilibrium sampling method with reduced variance appeared in the context of sampling the one-body electron density

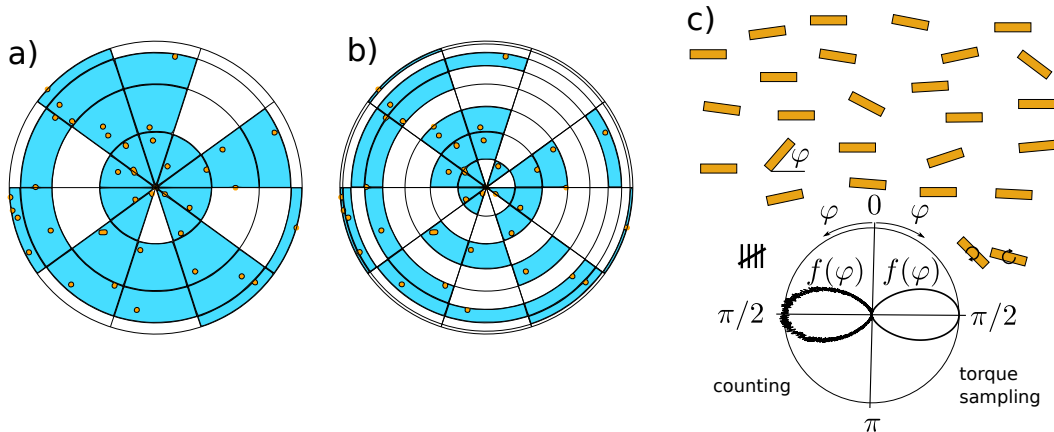


Figure 2: Illustration of the bin size dependence using the counting method. Panels a) and b) show the top view of the upper half unit sphere, which represents all possible orientations of a uniaxial particle. The hemisphere is divided into bins: forty in a) and eighty in b). The orange dots represent the particle orientations of a given microstate. The cyan color indicates bins with at least one particle with this orientation. Note that significantly less area is covered by occupied bins (cyan) in b) than in a). In c) a system of rods is illustrated schematically and the orientational distribution function is shown schematically for the counting method on the left with more statistical noise than the torque sampling method on the right.

in quantum Monte Carlo simulations [81, 82]. For classical systems, an estimator for the radial distribution function and the one-body density using the force acting on the particle was proposed in Ref. [83]. This work was extended to sample 3d charge and polarization densities with better accuracy [84]. Another approach for sampling the one-body density more accurately is force sampling, based on rewriting and integrating the exact one-body force balance equation to eliminate the ideal gas fluctuations [6]. In Ref. [6] it is shown that spurious small negative densities can occur in force sampling in regions that the particles rarely visit, e.g. close to a hard wall. To remedy this artifact the use of optimal linear combinations of reduced variance estimators is fruitful [85].

To further profit from methods with reduced statistical noise, the mapped-averaging framework was developed [86]. This framework uses approximate theoretical results to derive an ensemble average with less statistical noise. The mapped-averaging framework can be used to derive the previously mentioned force sampling methods and it has the potential to improve other existing methods. Usually, sampling the internal interactions is the key ingredient in reduced-variance sampling methods. This is difficult in hard systems, even though event driven simulations can be used to sample the force via the momentum transfer of each collision averaged over time. Alternatively, the mapped averaging framework can be applied to hard sphere systems in which a direct sampling of the forces is not feasible Ref. [87].

In this thesis, we develop a reduced variance method to sample the orientational distribution function [3], illustrated in Fig. 2 c). The method is conceptually related to the force sampling method in Ref [6] which we summarize in the following. The starting point is the exact one-body force balance equation in equilibrium given by

$$0 = \mathbf{F}_{\text{ext}} + \mathbf{F}_{\text{int}} - k_B T \nabla \rho. \quad (52)$$

The equilibrium one-body force density balance equation (52) is the same in MD, BD, and LD. Separating the ideal diffusive term and formally applying the inverse nabla operator ∇^{-1} leads to the following expression for the one-body density in terms of the force densities

$$\rho = \rho_0 + \frac{1}{k_B T} \nabla^{-1} \cdot (\mathbf{F}_{\text{ext}} + \mathbf{F}_{\text{int}}). \quad (53)$$

The constant ρ_0 is fixed such that the one-body density is normalized to the total number of particles, i.e. $\int d\mathbf{r} \rho(\mathbf{r}) = N$. Integrating the sampled external and internal force densities allows us to obtain the density profile via Eq. (53) with less statistical noise compared to the counting method. For systems inhomogeneous only along one spatial dimension, the inverse nabla operator reduces to a simple integral in space. For higher dimensions, a line integral, the electrostatic form of the inverse nabla operator, or minimization of a cost function based on the force balance equation with respect to the one-body density can be used [6] to obtain the density profile via Eq. (53).

In Ref. [3] we develop an equilibrium sampling method for anisotropic particles to sample the orientational distribution function with better statistical accuracy than the traditional counting method. Instead of the force density balance equation, we use the exact one-body torque density balance equation, see Eq. (42). We demonstrate that using torque sampling the statistical noise in the sampled orientational distribution function does not depend on the bin size. The torque sampling method outperforms the traditional counting method and it is particularly useful in systems that require small bin sizes.

1.2.2 Custom flow

In many-body computer simulations one propagates the particles in space and time according to the forces acting on each particle. The external force, which is in general time dependent, is usually prescribed. Furthermore, the particles interact not trivially with each other due to a given inter-particle interaction potential. The forces acting on the particles generate different many-body trajectories for each initial microstate and each realization of the thermal noise (the latter only in LD and BD). Averaging over an ensemble of different realizations (initial microstate and thermal noise) yields the corresponding one-body density and current fields. Their respective one-body dynamics, i.e. space and time dependence, are in general unknown beforehand.

We are interested in solving the inverse problem to have full control over the flow, which facilitates the systematic analysis of the one-body internal force and transport terms contributing to the force balance equation. The time-evolution of the one-body density and that of the current are prescribed, and we want to find the corresponding external force generating the desired dynamics. This inverse problem can be solved with the iterative custom flow method, first introduced for BD [8]. To construct the iteration scheme in BD, one starts with the exact one-body force balance equation (43) and solves for the external force

$$\mathbf{f}_{\text{ext}} = k_B T \nabla \ln \rho - \mathbf{f}_{\text{int}} + \gamma \mathbf{v}. \quad (54)$$

The density $\rho(\mathbf{r}, t)$ and the velocity $\mathbf{v}(\mathbf{r}, t)$ profiles are prescribed and are hence known. The only unknown term to determine the corresponding external force is

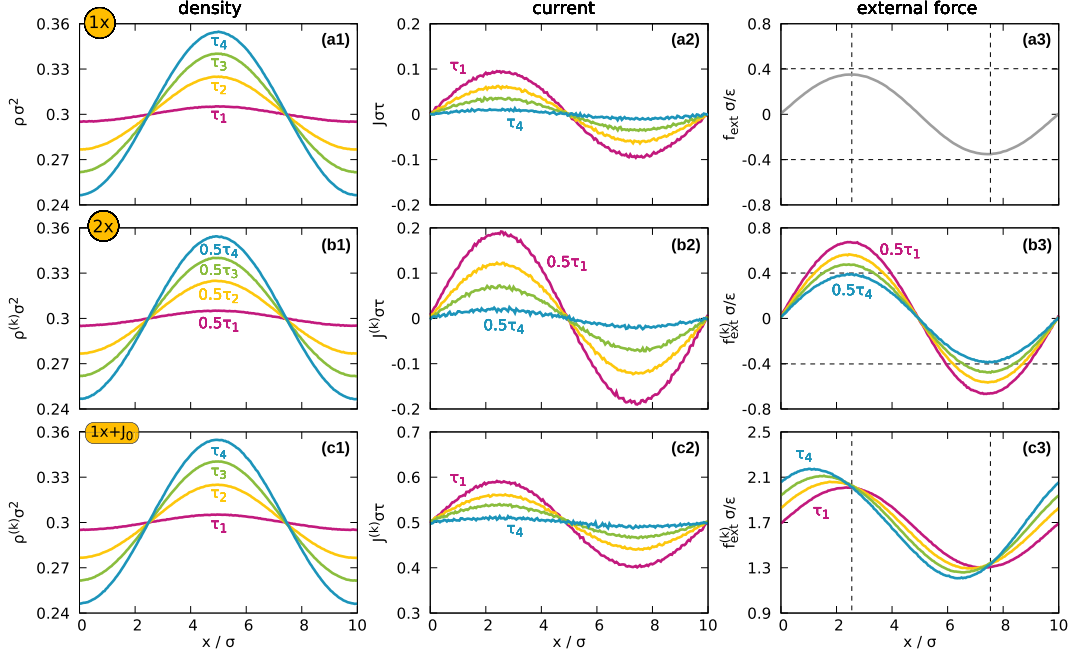


Figure 3: Custom flow BD simulations of $N = 30$ particles interacting via the WCA potential [9] in a 2d box with a side length of 10σ and periodic boundary conditions. The length and time scale are given by σ and τ , respectively. Profiles are averaged over 10^8 different trajectories. Three cases, that start in equilibrium with a homogeneous density profile, are displayed. In all cases four times are shown: $\tau_1/\tau = 0.08$ (violet), $\tau_2/\tau = 0.48$ (yellow), $\tau_3/\tau = 1.0$ (green), and $\tau_4/\tau = 2.2$ (blue). a) external field switched on at $t = 0$. b) speed up dynamics of the one-body density of a) using custom flow. c) one-body current offset compared to a) using custom flow. Reprinted with permission from Ref. [8]. Copyright © 2019 by the American Physical Society.

the internal force $\mathbf{f}_{\text{int}}(\mathbf{r}, t)$. The idea behind custom flow is to construct the external force iteratively by sampling the internal force at iteration i and calculating, based on Eq. (54), the external force for the next iteration $i + 1$. That is

$$\mathbf{f}_{\text{ext}}^{(i+1)} = k_B T \nabla \ln \rho - \mathbf{f}_{\text{int}}^{(i)} + \gamma \mathbf{v}. \quad (55)$$

This iteration is repeated until convergence is achieved. The iteration time step with which the external force is resolved in time, Δt , is in general larger than the integration time step of the simulation. The initial external force at each iteration can be set to that in an ideal gas. That is, using $\mathbf{f}_{\text{int}} = 0$ in Eq. (54).

Using custom flow, arbitrary flow patterns and density distributions can be constructed provided that they are compatible with the continuity equation (30). In Fig. 3 an example of custom flow in BD is shown. The first row (a) is a standard simulation with a fixed external force (a3) which is switched on at $t = 0$. The second row (b) uses custom flow to speed up the dynamics of the original density (a1) by a factor of two. Hence, as dictated by the continuity equation, the current (b2) is twice as large as in (a2). Furthermore, the external force (b3) is now time dependent. The third row (c) has the same time evolution of the density as in (a1). However, the current (c2) has now an offset of $J_0\sigma/\tau = 0.5$ compared to (a2) and hence uses also custom flow to find the corresponding external force. Here, σ and

τ are the length and time scales, respectively. The external force (c3) is also time dependent.

Solving this inverse problem, is useful even at the level of individual particles. It allows to e.g. independently and simultaneously move particles that have different shapes [88] or different magnetic properties [89].

Having full control over the flow allows us to study the viscous and the structural components of the internal force field [66]. The special case of having no flow and hence, being in equilibrium, is used to construct the adiabatic potential to separate adiabatic and superadiabatic contributions of the internal force in BD [65].

In this thesis we develop a custom flow method for Newtonian dynamics [1]. The goal is the same as in BD, i.e. to prescribe the time-evolution of the one-body density and current and then find the corresponding external force. The underlying dynamics, however, is different since we have inertia and in general complex momentum transport effects. The development of custom flow for MD has allowed us to study systematically viscosity, transport, and memory effects in bulk and shear flows [2, 4].

1.2.3 Memory effects

Memory effects occur in most physical systems. That is, the state at the present time depends on what happened in the past. This is very general, e.g. presently I am writing this thesis and this depends on the research that I have done in the past years. Memory effects play a role in, for example, optics [90], batteries [91], granular materials [92], and polymers able to remember different shapes [93].

In the following, we focus on memory effects that occur by integrating out degrees of freedom. One successful approach to deal with memory effects in many-body systems is the Mori-Zwanzig projection operator formalism [94, 95]. Originally used in statistical mechanics to coarse-grain the complex many-body dynamics using fewer degrees of freedom. This coarsening procedure introduces memory effects, friction, and fluctuating forces. The Mori-Zwanzig formalism was applied in different areas with complex dynamics in need of coarse graining. In Ref. [96] the formalism is extended towards general relativity in order to coarse-grain the universe in cosmology. In Ref. [97] the Mori-Zwanzig formalism was applied in the context of large eddy simulations. Also in climate models the formalism was successfully used [98]. The arising fluctuating forces in the Mori-Zwanzig formalism are often assumed to be delta-correlated. In Ref. [99] equations with non-Markovian fluctuating forces are derived. Using these projection techniques yields a generalized Langevin equation for a stationary underlying dynamics and can also be used to find a generalized Langevin equation for non-stationary underlying dynamics [100]. In both cases numerical iterative methods were developed to reconstruct the memory kernel using many-body simulations [101, 102].

In general memory effects can be non-local in space and time. In the following, we focus on the one-body level of many-body systems with memory effects arising due to integrating out degrees of freedom. In Ref. [103] memory effects in BD are investigated by applying a predefined external field that jumps in space and time favoring a step shear velocity field. A sketch of the system with the time evolution of the external field and the corresponding response of the current in BD and MD is shown in Fig. 4 (a) and 4 (b), respectively. The BD current reacts instantaneously to the applied forces due to the absence of inertia. The current jumps to a value compatible with the amplitude of the external force. Due to memory effects in

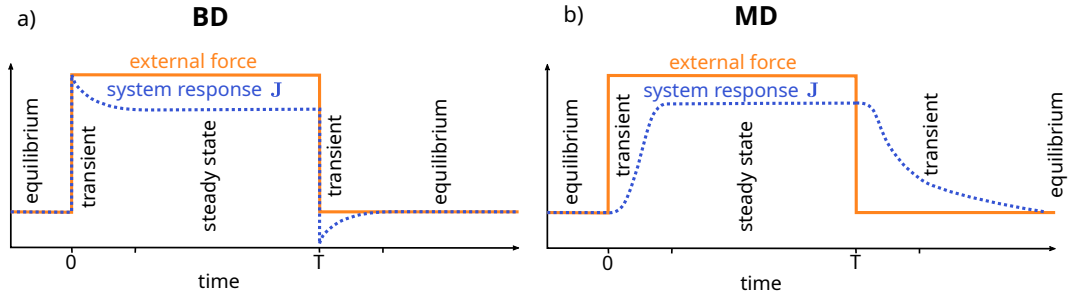


Figure 4: Illustration of the time evolution of a system with an applied external step shear force (orange solid) and the corresponding amplitude of the system response (blue dashed) for a) J for BD and b) J for MD.

the internal force, the current relaxes to a steady value. When the external force is switched off at time T , the current jumps to a negative value compatible with the internal interaction opposing the former external field until the memory effects decay. In MD there is inertia and the current is the time integral over all forces applied to the system in the past. Hence, the steady state current builds up slower than in BD until dissipation is compensated by the external driving. When the external field is switched off it takes time to dissipate the energy of the flow. This happens while also the internal interaction and the momentum transport are subject to memory effects. Hence, it is difficult to distinguish between inertial and memory effects in such situations.

Memory kernels non-local in time and additionally non-local in space have been used to describe the internal force using the framework of PFT in over-damped Brownian systems. We use a slightly different approach in Refs. [2, 4] for MD systems. Instead of prescribing the external force, we prescribe the time-evolution of the velocity field and the one-body density and find the corresponding external force using custom flow [1]. This allows us to decrease the velocity field to zero fast and not having to wait for the viscous forces to reach a vanishing velocity field. Forcing the velocity field to vanish quickly isolates signals in the internal force and the kinetic stress tensor that come solely from memory effects. This helped us to identify the acceleration dependence of the one-body internal force in shear and bulk flows [2, 4].

1.2.4 Thermostats

In some applications it is desirable to simulate many-body systems at a controlled temperature, e.g. to study temperature dependent processes, to remove heat dissipated from the flow in non-equilibrium systems, and to match experimental conditions. In these cases a thermostat controlling the temperature is helpful. In Ref. [1] we implement and test a thermostat alongside custom flow in MD. Furthermore, custom flow can be used, as demonstrated in Ref. [1], to investigate the possible effects that thermostats have on the one-body level, especially on the one-body force balance equation. In Ref. [2] the dissipated energy of the flow is negligible and hence requires no thermostat. Furthermore, the use of a thermostat would complicate the analysis on the level of the one-body force balance due to new terms originating from the thermostat. Especially, the kinetic stress tensor, which we investigate in Ref. [4], containing the velocity fluctuations would be affected. Nevertheless, using custom

flow with a thermostat might be fruitful to investigate the effect of keeping the temperature constant on the momentum transport, as described by the divergence of the kinetic stress tensor.

Several thermostats have been developed to modify the many-body dynamics in order to keep the temperature constant, see an overview in Ref. [104]. First of all, we need to define what temperature is in this context. In equilibrium the temperature is well defined by the equipartition theorem, Eq. (36), which relates the average kinetic energy in the system to the thermal energy. However, defining a temperature in non-equilibrium is not straightforward [105]. One possibility in MD is to modify the equilibrium definition by subtracting the kinetic energy of the flow from the total kinetic energy. There are several algorithms to keep the desired temperature constant in computer simulations. Most thermostats rely on velocity scaling in one way or another. In Ref. [106] the velocity rescaling originates from stochastic forces on the particles enforcing the correct temperature. In Ref. [107] the system is coupled to an external heat bath. A more elaborated approach is presented in Ref. [108] that has a smoother rescaling and recovers the two aforementioned algorithms as limiting cases. Also LD and BD, introduced in Sec. 1.1.2, keep the temperature constant by construction. A closely related approach is dissipative particle dynamics that additionally conserves momentum [109]. Since the approaches to create a thermostat are different, they might also lead to different results [110]. This is especially the case in e.g. ultra confined flows with high shear rates [111]. For highly confined systems it also makes a difference whether the thermostat acts on the fluid or on the confining wall when comparing simulations to experimental results [112].

2 Overview of the publications

In the following we give an overview of the publications contributing to this cumulative thesis [1–3]. The publications have in common the development of methods and theoretical approaches for a better understanding and characterisation of many-body systems using one-body fields. We focus especially on the exact one-body force and torque balance equations. The publications are interconnected and cover several physical aspects of many-body systems, including equilibrium and non-equilibrium, isotropic and anisotropic interactions, inertial and overdamped dynamics, see Fig. 5. In the first publication [1] we introduce the numerical custom flow method derived from the non-equilibrium one-body force balance equation in MD. The method allows us to prescribe the one-body dynamics of the density and of the flow. Furthermore, we provide test cases as a proof of concept, including the addition of a thermostat alongside custom flow.

Publications [2] and [4] (to be submitted) rely on custom flow to provide clean bulk and shear flows in order to study memory and inertial effects of the one-body internal force field and the momentum transport in the non-equilibrium one-body force balance equation in MD. In Ref. [2] we focus on the internal interactions and show that the acceleration field is required to properly model the internal force field. Reference [4] (to be submitted) focuses on momentum transport and the interplay

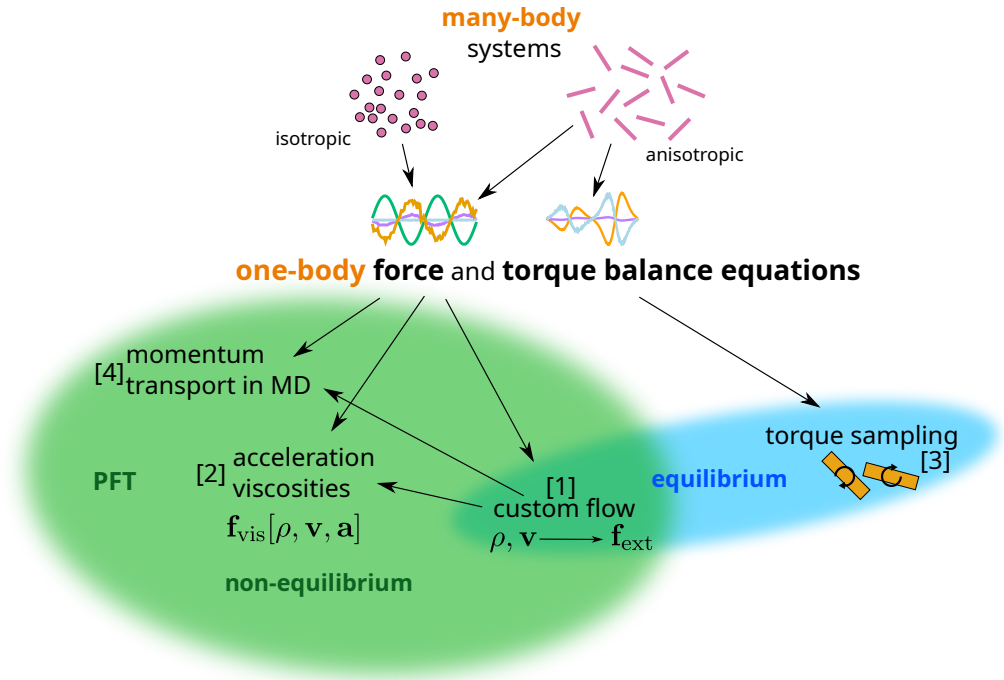


Figure 5: Illustration of the connections and differences between the works derived from this thesis: MD custom flow method [1], applying custom flow to design bulk and shear flows and investigate the contribution of the acceleration field to the internal force [2] and the momentum transport [4] (to be submitted), and torque sampling [3]. All works make use of many-body simulations with information reduced to the one-body level and are based on either the one-body force or the one-body torque balance equations.

of all terms contributing to the one-body force balance equation.

Lastly, we introduce a numerical method for anisotropic particles based on the exact equilibrium one-body torque density balance equation that improves the sampling accuracy of the one-body orientational distribution function [3]. We also provide several test cases to show the advantages of torque sampling compared to the traditional counting method.

2.1 Custom flow in molecular dynamics

In this publication [1] we develop a numerical iterative method to prescribe the time evolution of the one-body density and the one-body current of a many-body system following Newtonian dynamics. Controlling the one-body density, velocity, and acceleration fields is convenient to e.g. study memory effects and to systematically construct approximations for the one-body inter-particle force field and the momentum transport via an approximate power functional [2, 4].

The custom flow method generates the desired time evolution of the input fields by iteratively adjusting the external force in an iteration time step which is usually larger than the integration time step. The adjustment reduces iteratively the difference between the target and sampled fields during each iteration time step. Repeating the iteration scheme for every time step leads to the desired time evolution of the system.

We provide several test cases as a proof of concept. We first prescribe an external force which is constant in time and obtain the corresponding dynamics of the one-body fields by averaging over a set of simulations that differ on the initial microstates. Then, we use custom flow to slow down the sampled dynamics of the one-body density. The resulting complex time-dependent external force field of the slow motion system produces the same one-body dynamics of the density profile and additionally the one-body current profile has half the original amplitude as dictated by the continuity equation. Furthermore, we demonstrate the validity of the custom flow method in presence of thermostats. We propose that the thermostat should act on the kinetic energy of the velocity fluctuations rather than on the total kinetic energy. Otherwise, the kinetic energy of the flow due to the velocity field would be altered. As a last example we demonstrate the use of custom flow to generate arbitrary one-body dynamics provided that they are compatible with the continuity equation. In this case we grow peaks in the one-body density profile fixing the one-body current up to a constant which we choose such that the integrated current vanishes. Hence, when the density peak is fully grown the one-body current vanishes everywhere. At this point the input fields are all time-independent, but the one-body momentum transport and the internal force field still change with time. This clearly illustrates the occurrence of memory effects and also shows the potential of custom flow to isolate memory effects from the time-evolution of the one-body density and current profiles.

2.2 Shear and bulk acceleration viscosities in simple fluids

Here, we use the custom flow method for MD [1] to investigate superadiabatic contributions to the one-body internal force field, especially in rapidly changing flows [2]. Custom flow allows us to create pure bulk ($\nabla \times \mathbf{v} = 0$ and $\nabla \cdot \mathbf{v} \neq 0$) and pure shear ($\nabla \cdot \mathbf{v} = 0$ and $\nabla \times \mathbf{v} \neq 0$) flows with prescribed time evolution. Having full control over the flow profile and the density profile is essential to investigate sys-

tematically the superadiabatic internal force field originating from the inter-particle interactions. Both flows have a time independent one-body density and a time dependent current. Furthermore, the velocity field factorizes in a time dependent part and a space dependent part. As a consequence, the velocity and the acceleration fields have in each flow the same spatial dependence. The time dependent part of the velocity field is such that its amplitude first increases, then stays constant during a time interval, later decreases until it vanishes, and finally stays zero afterwards. We show that the viscous superadiabatic internal force depends linearly on both the velocity and the acceleration field. Therefore, the superadiabatic internal force can be split into a spatial and a time dependent part. The space dependent contribution is the same for the velocity and the acceleration fields. This allows us to investigate the dependence on the velocity and the acceleration fields by looking only at the time dependent part.

For the bulk flow, the time dependent part can be easily described using the velocity and the acceleration profiles together with a simple memory kernel. The time dependent part of the internal force shows an overshoot compared to the steady state value when increasing the amplitude of the velocity profile and an undershoot below zero when decreasing the amplitude of the velocity field to zero. Using symmetry arguments we demonstrate that the acceleration field is responsible for this behaviour. It would be possible to use only the velocity field and construct a complex memory kernel with a negative tail. However, this would imply an unphysical negative viscosity.

For the shear flow no such over- and undershoot appear. This might be due to longer memory times associated to shear-like deformations. The internal viscous force can be approximated reasonably good using only the velocity field. However, we could confirm the presence of the acceleration field in the internal viscous force using a modified flow. Instead of decreasing again the current in amplitude, we propagate the spatial structure with a constant drift velocity in the positive direction while keeping the amplitude constant. Describing the viscous force using only the velocity field results in a phase shift in the theoretical prediction of the viscous internal force as compared to the sampled data. Incorporating the acceleration field yields, however, an accurate description of the internal viscous force.

This work shows the relevance of the acceleration field to describe the internal viscous force in rapidly changing flows accurately. We argue that using both the velocity and the acceleration fields constitutes an accurate and more physical alternative to the description of the internal force than using complex memory kernels and only the velocity profile.

2.3 Reduced-variance orientational distribution functions from torque sampling

In many-body computer simulations it is possible to sample the orientational distribution function (ODF) by dividing the set of orientations (here given by the surface of the unit sphere) into bins and counting how often the particles visit each bin. By decreasing the bin size, this traditional counting method either produces significant statistical noise or requires a substantial increase of the sampling time. We develop in Ref. [3] a method to sample the ODF in many-body systems of anisotropic particles in equilibrium taking advantage of the exact one-body torque density balance equation. The ODF is obtained by sampling the one-body torques and integrating them appropriately. This circumvents the ideal gas fluctuations and hence reduces

the statistical noise in the sampled profile of the ODF.

To demonstrate the advantages of the torque sampling method compared to the counting method we consider several systems. First, we perform Langevin dynamics simulations of rectangles in a two dimensional box with periodic boundary conditions. We investigate a system with low packing fraction and an external potential favoring one orientation. We show visually for several sampling times the smoother profiles obtained by the torque sampling method compared to the counting method. Furthermore, we investigate the error of each method as a function of the bin size. The error of the torque sampling method is independent of the bin size, whereas the error of the counting method diverges for bin sizes approaching zero. With torque sampling it is therefore possible to sample the ODF with arbitrarily high angular resolution. Second, we investigate a system with moderate packing fraction favoring tetratic order, i.e. there are two favored orientations (directors) orthogonal to each other. Additionally, the particles are subject to an external potential favoring orientations along only one of the directors. The resulting ODF has two peaks with different amplitudes. Again, the torque sampling method delivers more accurate profiles than the counting method. This particular case shows that the complete ODF might be required to fully characterise the orientational order of the system since sampling only the nematic and the tetratic order parameters would not provide enough information. Last, we perform overdamped Brownian dynamics simulations of Gay-Berne particles in a three dimensional box. The particles are subject to an external potential favoring orientations along the polar axis. The torque sampling method provides better accuracy than the counting method, especially close to the pole since we use spherical coordinates, and hence smaller bins for smaller polar angles.

2.4 Outlook

This thesis gives insight into some problems concerning methods and theoretical descriptions of many-body systems on the one-body level, and it also opens new interesting questions, some of which are described in the following.

In ongoing work [4] we investigate shear and bulk flows of isotropic particles similar to those in Ref. [2]. We investigate all contributions to the exact one-body force balance equation and focus in particular on the momentum transport term given by the divergence of the kinetic stress tensor. The density profile is stationary and both flows can be factorized in a time and a space dependent part. This setup allows us to investigate the response of the kinetic stress tensor to a prescribed flow using custom flow [1]. The kinetic stress tensor has an ideal part and an excess part, see Eq. (32) and the discussion around it. The latter contains all velocity fluctuations. We also split the excess contribution into viscous and structural components depending on whether the sign changes or not under flow reversal, respectively. We propose approximations for the spatial part of each component of the kinetic stress tensor.

The flow in the shear case is relatively strong, and hence flow energy is dissipated. This influences the amplitude of the internal force and the kinetic stress tensor. Despite of the strong driving of the system, the spatial dependence of the approximations for the kinetic stress tensor are in very good agreement with the sampled data. Examples of the kinetic stress tensor components for the shear flow are shown in Fig. 6.

The bulk flow dissipates very little energy compared to the thermal energy that

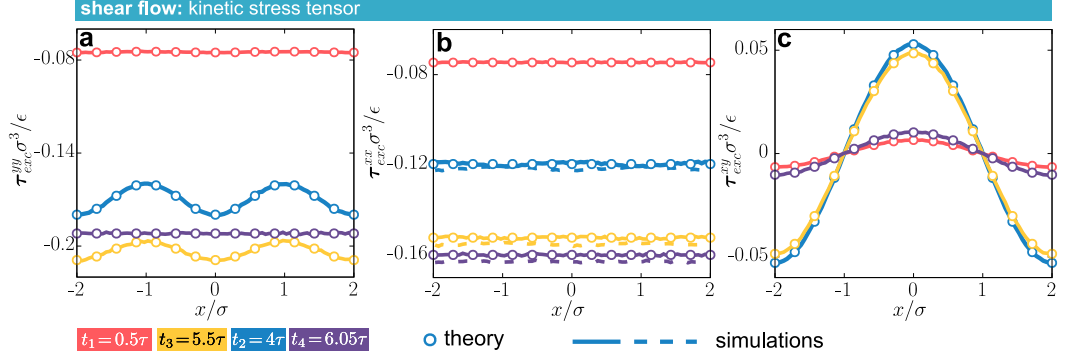


Figure 6: Kinetic stress tensor of a pure shear flow with homogeneous density profile and a sinusoidal velocity field pointing in y -direction. Here, only the non-vanishing components of the excess kinetic stress tensor are shown at different times $t_1 = 0.5\tau$, $t_2 = 4\tau$, $t_3 = 5.5\tau$, and $t_4 = 6.05\tau$ corresponding to increasing, quasi stationary, decreasing, and vanishing currents, respectively. The diagonal elements of the kinetic stress tensor yy in panel a), xx in panel b) (solid lines), and zz in panel b) (dashed lines) are structural, i.e. no sign change under flow reversal. The off-diagonal element xy in panel c) is viscous, i.e. its sign changes under flow reversal. The solid and dashed lines represent sampled data and the circles represent the theoretical prediction.

is already present in the system. The structural components change slightly in amplitude due to the dissipated flow energy. The viscous part of the xx -component of the kinetic stress tensor shows complex behaviour changing also its spatial structure during the time evolution of the system. A local description in space with a non-local memory kernel in time seems to be sufficient to describe the kinetic stress tensor for a steady velocity field. To find a complete description in full non-equilibrium we propose the following two routes.

- To derive an exact equation for the time evolution of the one-body kinetic stress tensor, analogous to the derivation of the exact one-body force balance equation. New terms will appear that need to be sampled and understood. Splitting the equation for the dynamics of the kinetic stress tensor might also reveal more insights.
- To investigate flows with both a homogeneous and an inhomogeneous part in the system. This setup allows for the detection and the isolation of memory effects in space. The internal force and the kinetic stress tensor depend on spatial derivatives of the velocity field that vanish in the homogeneous part of the system. Hence, any signal of the internal force and the kinetic stress tensor in the homogeneous region must occur due to non-local memory effects in space. Investigating these systems might help to find a memory kernel non-local in space and in time capable to describe complex flows.

It would be interesting to extend the analysis of the internal force and that of the momentum transport from isotropic to anisotropic particles. First, one needs to extend MD custom flow to systems with orientational degrees of freedom. Then, one can perform an analysis similar to that done here for isotropic particles but for anisotropic particles and focusing on the internal torques, the angular kinetic stress tensor, and the coupling tensor linking spatial and orientational degrees of freedom.

Similar to time deriving the kinetic stress tensor to obtain its equation of motion, it might be interesting to do the analogue for the orientational counterpart and also for the coupling tensor.

Finally, applying force and torque sampling simultaneously might be advantageous in situations where spatial and orientational degrees of freedom in the one-body density are coupled, such as for example if topological defects arise in the system [113] or if there is also positional order like in smectic [114] or columnar phases [115]. In these situations the one-body force and torque balance equations determine the density profile, which carries a dependence on both the spatial and the orientational degrees of freedom, simultaneously.

2.5 Author contributions

I am the first author in all three publications contained in this cumulative thesis [1–3]. I created the first complete draft, including text, figures, and bibliography, of all the publications. I generated, analysed, and interpreted the data in close collaboration with my supervisors. Besides generating the first draft, I contributed as follows to each publication.

- In Ref. [1] I developed the numerical iterative custom flow method for MD and implemented the parallel MD code including custom flow for MD with thermostats. I ran the test cases for the custom flow method using the developed code.
- In Ref. [2] I used the code developed in Ref. [1] to simulate shear and bulk flows. Furthermore, I implemented a parallel BD Code including custom flow to compare between MD and BD. I analyzed the resulting data and developed approximate terms to the Power functional including memory and acceleration field contributions.
- In Ref. [3] I wrote MD and LD codes for purely repulsive rectangles in two dimensions. Furthermore, I implemented a BD code for Gay-Berne particles in three dimensions. I developed the torque sampling method and tested its advantages compared to the counting method with simulations using the aforementioned codes.

Bibliography

- ¹J. Renner, M. Schmidt, and D. de las Heras, “Custom flow in molecular dynamics”, *Phys. Rev. Res.* **3**, 013281 (2021).
- ²J. Renner, M. Schmidt, and D. de las Heras, “Shear and bulk acceleration viscosities in simple fluids”, *Phys. Rev. Lett.* **128**, 094502 (2022).
- ³J. Renner, M. Schmidt, and D. de las Heras, “Reduced-variance orientational distribution functions from torque sampling”, *J. Phys.: Condens. Matter* **35**, 235901 (2023).
- ⁴J. Renner, M. Schmidt, and D. de las Heras, “Non-equilibrium one-body force balance equation in molecular dynamics”, to be submitted (2023).
- ⁵M. Schmidt, “Power functional theory for many-body dynamics”, *Rev. Mod. Phys.* **94**, 015007 (2022).
- ⁶D. de las Heras and M. Schmidt, “Better than counting: density profiles from force sampling”, *Phys. Rev. Lett.* **120**, 218001 (2018).
- ⁷B. Rotenberg, “Use the force! Reduced variance estimators for densities, radial distribution functions, and local mobilities in molecular simulations”, *J. Chem. Phys.* **153**, 150902 (2020).
- ⁸D. de las Heras, J. Renner, and M. Schmidt, “Custom flow in overdamped Brownian dynamics”, *Phys. Rev. E* **99**, 023306 (2019).
- ⁹J. D. Weeks, D. Chandler, and H. C. Andersen, “Role of repulsive forces in determining the equilibrium structure of simple liquids”, *J. Chem. Phys.* **54**, 5237 (1971).
- ¹⁰S. Sacanna, D. J. Pine, and G.-R. Yi, “Engineering shape: the novel geometries of colloidal self-assembly”, *Soft Matter* **9**, 8096 (2013).
- ¹¹E. Bianchi, R. Blaak, and C. N. Likos, “Patchy colloids: state of the art and perspectives”, *Phys. Chem. Chem. Phys.* **13**, 6397 (2011).
- ¹²I. Nezbeda, J. Kolafa, and Y. V. Kalyuzhnyi, “Primitive model of water: II. theoretical results for the structure and thermodynamic properties”, *Mol. Phys.* **68**, 143 (1989).
- ¹³M. H. Ford, S. M. Auerbach, and P. Monson, “On the mechanical properties and phase behavior of silica: a simple model based on low coordination and strong association”, *J. Chem. Phys.* **121**, 8415 (2004).
- ¹⁴R. P. Sear, “Phase behavior of a simple model of globular proteins”, *J. Chem. Phys.* **111**, 4800 (1999).
- ¹⁵A. Lomakin, N. Asherie, and G. B. Benedek, “Aeolotopic interactions of globular proteins”, *Proc. Natl. Acad. Sci.* **96**, 9465 (1999).
- ¹⁶M. J. Stephen and J. P. Straley, “Physics of liquid crystals”, *Rev. Mod. Phys.* **46**, 617 (1974).
- ¹⁷M. Schadt, “Liquid crystal materials and liquid crystal displays”, *Annu. Rev. Mater. Sci.* **27**, 305 (1997).
- ¹⁸I. Tadwee, S. Shahi, V. Ramteke, and I. Syed, “Liquid crystals pharmaceutical application: a review”, *Int. J. Pharm. Res. Allied Sci* **1**, 6 (2012).

- ¹⁹C. J. Hernandez and T. G. Mason, “Colloidal alphabet soup: monodisperse dispersions of shape-designed lithoparticles”, *J. Phys. Chem. C* **111**, 4477 (2007).
- ²⁰Z. Gong, T. Hueckel, G.-R. Yi, and S. Sacanna, “Patchy particles made by colloidal fusion”, *Nature* **550**, 234 (2017).
- ²¹C. Fernández-Rico, M. Chiappini, T. Yanagishima, H. de Sousa, D. G. A. L. Aarts, M. Dijkstra, and R. P. A. Dullens, “Shaping colloidal bananas to reveal biaxial, splay-bend nematic, and smectic phases”, *Science* **369**, 950 (2020).
- ²²Y. Jiao, F. Stillinger, and S. Torquato, “Optimal packings of superdisks and the role of symmetry”, *Phys. Rev. Lett.* **100**, 245504 (2008).
- ²³S. Torquato and Y. Jiao, “Dense packings of the platonic and archimedean solids”, *Nature* **460**, 876 (2009).
- ²⁴Y. Martínez-Ratón and E. Velasco, “Orientational ordering in a fluid of hard kites: A density-functional-theory study”, *Phys. Rev. E* **102**, 052128 (2020).
- ²⁵Y. Martínez-Ratón and E. Velasco, “Failure of standard density functional theory to describe the phase behavior of a fluid of hard right isosceles triangles”, *Phys. Rev. E* **104**, 054132 (2021).
- ²⁶Y. Martínez-Ratón and E. Velasco, “Effect of clustering on the orientational properties of a fluid of hard right isosceles triangles”, *Phys. Fluids* **34**, 037110 (2022).
- ²⁷D. J. Dichmann, Y. Li, and J. H. Maddocks, *Mathematical approaches to biomolecular structure and dynamics* (Springer, New York, 1996).
- ²⁸D. Frenkel and B. Smit, *Understanding molecular simulation: from algorithms to applications* (Elsevier, San Diego, 2002).
- ²⁹Y.-G. Tao, W. K. den Otter, J. T. Padding, J. K. G. Dhont, and W. J. Briels, “Brownian dynamics simulations of the self-and collective rotational diffusion coefficients of rigid long thin rods”, *J. Chem. Phys.* **122**, 244903 (2005).
- ³⁰N. Grønbech-Jensen and O. Farago, “A simple and effective Verlet-type algorithm for simulating Langevin dynamics”, *Mol. Phys.* **111**, 983 (2013).
- ³¹F. Sammüller and M. Schmidt, “Adaptive Brownian dynamics”, *J. Chem. Phys.* **155**, 134107 (2021).
- ³²J.-P. Hansen and I. R. McDonald, *Theory of simple liquids: with applications to soft matter* (Academic press, Oxford, 2013).
- ³³M. Schmidt, “Power functional theory for Newtonian many-body dynamics”, *J. Chem. Phys.* **148**, 044502 (2018).
- ³⁴R. C. Tolman, “A general theory of energy partition with applications to quantum theory”, *Phys. Rev.* **11**, 261 (1918).
- ³⁵M. J. Uline, D. W. Siderius, and D. S. Corti, “On the generalized equipartition theorem in molecular dynamics ensembles and the microcanonical thermodynamics of small systems”, *J. Chem. Phys.* **128**, 124301 (2008).
- ³⁶A. Kitao, K. Yonekura, S. Maki-Yonekura, F. A. Samatey, K. Imada, K. Namba, and N. Go, “Switch interactions control energy frustration and multiple flagellar filament structures”, *Proc. Natl. Acad. Sci.* **103**, 4894 (2006).
- ³⁷K. Y. Sanbonmatsu and C.-S. Tung, “High performance computing in biology: multimillion atom simulations of nanoscale systems”, *J. Struct. Biol.* **157**, 470 (2007).

- ³⁸G. R. Srinivasan, J. D. Baeder, S. Obayashi, and W. J. McCroskey, “Flowfield of a lifting rotor in hover-A Navier-Stokes simulation”, *AIAA J.* **30**, 2371 (1992).
- ³⁹M. M. Rai, “Navier-Stokes simulations of rotor/stator interaction using patched and overlaid grids”, *J. Propuls. Power* **3**, 387 (1987).
- ⁴⁰N. Thuerey, K. Weißenow, L. Prantl, and X. Hu, “Deep learning methods for Reynolds-averaged Navier-Stokes simulations of airfoil flows”, *AIAA J.* **58**, 25 (2020).
- ⁴¹D. Jie, X. Diao, K. B. Cheong, and L. K. Yong, “Navier-Stokes simulations of gas flow in micro devices”, *J. Micromech. Microeng.* **10**, 372 (2000).
- ⁴²D. K. Walters and W. H. Luke, “A method for three-dimensional Navier-Stokes simulations of large-scale regions of the human lung airway”, *J. Fluids Eng.* **132**, 051101 (2010).
- ⁴³S. Abadie, D. Morichon, S. Grilli, and S. Glockner, “Numerical simulation of waves generated by landslides using a multiple-fluid Navier-Stokes model”, *Coast. Eng.* **57**, 779 (2010).
- ⁴⁴K. Abdolmaleki, K. P. Thiagarajan, and M. T. Morris-Thomas, “Simulation of the dam break problem and impact flows using a Navier-Stokes solver”, *Simulation* **13**, 17 (2004).
- ⁴⁵C. J. Greenshields and J. M. Reese, “The structure of shock waves as a test of Brenner’s modifications to the Navier-Stokes equations”, *J. Fluid Mech.* **580**, 407 (2007).
- ⁴⁶N. Coleman, “A derivation of the Navier-Stokes equations”, *Math. Exch.* **7**, 1 (2010).
- ⁴⁷A. E. Green and R. S. Rivlin, “On Cauchy’s equations of motion”, *Z. Angew. Math. Phys.* **15**, 290 (1964).
- ⁴⁸Y. Chen, “The origin of the distinction between microscopic formulas for stress and Cauchy stress”, *EPL* **116**, 34003 (2016).
- ⁴⁹I. Gallagher, “From Newton to Navier-Stokes, or how to connect fluid mechanics equations from microscopic to macroscopic scales”, *Bull. Am. Math. Soc.* **56**, 65 (2019).
- ⁵⁰I. Gallagher, L. Saint-Raymond, and B. Texier, *From Newton to Boltzmann: hard spheres and short-range potentials* (European Mathematical Society, Zürich, 2013).
- ⁵¹I. Gallagher, “From classical mechanics to kinetic theory and fluid dynamics”, *Journ. Équ. dériv. partielles*, 1 (2014).
- ⁵²R. Deissler, “Derivation of the Navier-Stokes equation”, *Am. J. Phys.* **44**, 1128 (1976).
- ⁵³P. Hohenberg and W. Kohn, “Inhomogeneous electron gas”, *Phys. Rev.* **136**, B864 (1964).
- ⁵⁴W. Kohn and L. J. Sham, “Self-consistent equations including exchange and correlation effects”, *Phys. Rev.* **140**, A1133 (1965).
- ⁵⁵R. Evans, “The nature of the liquid-vapour interface and other topics in the statistical mechanics of non-uniform, classical fluids”, *Adv. Phys.* **28**, 143 (1979).

- ⁵⁶U. M. B. Marconi and P. Tarazona, “Dynamic density functional theory of fluids”, *J. Chem. Phys.* **110**, 8032 (1999).
- ⁵⁷U. M. B. Marconi and P. Tarazona, “Dynamic density functional theory of fluids”, *J. Phys.: Condens. Matter* **12**, A413 (2000).
- ⁵⁸D. de las Heras, T. Zimmermann, F. Sammüller, S. Hermann, and M. Schmidt, “Perspective: How to overcome dynamical density functional theory”, *J. Phys.: Condens. Matter* **35**, 271501 (2023).
- ⁵⁹M. Schmidt and J. M. Brader, “Power functional theory for Brownian dynamics”, *J. Chem. Phys.* **138**, 214101 (2013).
- ⁶⁰M. Schmidt, “Quantum power functional theory for many-body dynamics”, *J. Chem. Phys.* **143**, 174108 (2015).
- ⁶¹R. Roth, “Fundamental measure theory for hard-sphere mixtures: a review”, *J. Phys.: Condens. Matter* **22**, 063102 (2010).
- ⁶²A. Fortini, D. de las Heras, J. M. Brader, and M. Schmidt, “Superadiabatic forces in Brownian many-body dynamics”, *Phys. Rev. Lett.* **113**, 167801 (2014).
- ⁶³N. C. Stuhlmüller, T. Eckert, D. de las Heras, and M. Schmidt, “Structural nonequilibrium forces in driven colloidal systems”, *Phys. Rev. Lett.* **121**, 098002 (2018).
- ⁶⁴D. de las Heras and M. Schmidt, “Velocity gradient power functional for Brownian dynamics”, *Phys. Rev. Lett.* **120**, 028001 (2018).
- ⁶⁵T. Geigenfeind, D. de las Heras, and M. Schmidt, “Superadiabatic demixing in nonequilibrium colloids”, *Commun. Phys.* **3**, 1 (2020).
- ⁶⁶D. de las Heras and M. Schmidt, “Flow and structure in nonequilibrium Brownian many-body systems”, *Phys. Rev. Lett.* **125**, 018001 (2020).
- ⁶⁷P. Krinninger, M. Schmidt, and J. M. Brader, “Nonequilibrium phase behavior from minimization of free power dissipation”, *Phys. Rev. Lett.* **117**, 208003 (2016).
- ⁶⁸P. Krinninger and M. Schmidt, “Power functional theory for active Brownian particles: general formulation and power sum rules”, *J. Chem. Phys.* **150**, 074112 (2019).
- ⁶⁹S. Hermann, P. Krinninger, D. de las Heras, and M. Schmidt, “Phase coexistence of active Brownian particles”, *Phys. Rev. E* **100**, 052604 (2019).
- ⁷⁰S. Hermann, D. de las Heras, and M. Schmidt, “Phase separation of active Brownian particles in two dimensions: anything for a quiet life”, *Mol. Phys.* **119**, e1902585 (2021).
- ⁷¹S. Hermann, D. de las Heras, and M. Schmidt, “Non-negative interfacial tension in phase-separated active Brownian particles”, *Phys. Rev. Lett.* **123**, 268002 (2019).
- ⁷²S. Hermann and M. Schmidt, “Active interface polarization as a state function”, *Phys. Rev. Res.* **2**, 022003 (2020).
- ⁷³F. Sammüller, D. de las Heras, and M. Schmidt, “Inhomogeneous steady shear dynamics of a three-body colloidal gel former”, *J. Chem. Phys.* **158**, 054908 (2023).
- ⁷⁴J. M. Brader and M. Schmidt, “Power functional theory for the dynamic test particle limit”, *J. Phys.: Condens. Matter* **27**, 194106 (2015).

- ⁷⁵T. Schindler and M. Schmidt, “Dynamic pair correlations and superadiabatic forces in a dense Brownian liquid”, *J. Chem. Phys.* **145**, 064506 (2016).
- ⁷⁶L. L. Treffenstädt and M. Schmidt, “Universality in driven and equilibrium hard sphere liquid dynamics”, *Phys. Rev. Lett.* **126**, 058002 (2021).
- ⁷⁷L. L. Treffenstädt, T. Schindler, and M. Schmidt, “Dynamic decay and superadiabatic forces in the van Hove dynamics of bulk hard sphere fluids”, *SciPost Phys.* **12**, 133 (2022).
- ⁷⁸S. Hermann and M. Schmidt, “Noether’s theorem in statistical mechanics”, *Commun. Phys.* **4**, 176 (2021).
- ⁷⁹S. Hermann and M. Schmidt, “Variance of fluctuations from Noether invariance”, *Commun. Phys.* **5**, 276 (2022).
- ⁸⁰M. Brütting, T. Trepl, D. de las Heras, and M. Schmidt, “Superadiabatic forces via the acceleration gradient in quantum many-body dynamics”, *Molecules* **24**, 3660 (2019).
- ⁸¹R. Assaraf and M. Caffarel, “Zero-variance principle for Monte Carlo algorithms”, *Phys. Rev. Lett.* **83**, 4682 (1999).
- ⁸²R. Assaraf, M. Caffarel, and A. Scemama, “Improved Monte Carlo estimators for the one-body density”, *Phys. Rev. E* **75**, 035701 (2007).
- ⁸³D. Borgis, R. Assaraf, B. Rotenberg, and R. Vuilleumier, “Computation of pair distribution functions and three-dimensional densities with a reduced variance principle”, *Mol. Phys.* **111**, 3486 (2013).
- ⁸⁴S. W. Coles, D. Borgis, R. Vuilleumier, and B. Rotenberg, “Computing three-dimensional densities from force densities improves statistical efficiency”, *J. Chem. Phys.* **151**, 064124 (2019).
- ⁸⁵S. W. Coles, E. Mangaud, D. Frenkel, and B. Rotenberg, “Reduced variance analysis of molecular dynamics simulations by linear combination of estimators”, *J. Chem. Phys.* **154**, 191101 (2021).
- ⁸⁶A. Purohit, A. J. Schultz, and D. A. Kofke, “Force-sampling methods for density distributions as instances of mapped averaging”, *Mol. Phys.* **117**, 2822 (2019).
- ⁸⁷A. Trokhymchuk, A. J. Schultz, and D. A. Kofke, “Alternative ensemble averages in molecular dynamics simulation of hard spheres”, *Mol. Phys.* **117**, 3734 (2019).
- ⁸⁸M. Mirzaee-Kakhki, A. Ernst, D. de las Heras, M. Urbaniak, F. Stobiecki, J. Gördes, M. Reginka, A. Ehresmann, and T. Fischer, “Simultaneous polydirectional transport of colloidal bipeds”, *Nat. Commun.* **11**, 4670 (2020).
- ⁸⁹J. Loehr, M. Loenne, A. Ernst, D. de las Heras, and T. Fischer, “Topological protection of multiparticle dissipative transport”, *Nat. Commun.* **7**, 11745 (2016).
- ⁹⁰G. Osnabrugge, R. Horstmeyer, I. N. Papadopoulos, B. Judkewitz, and I. M. Vellekoop, “Generalized optical memory effect”, *Optica* **4**, 886 (2017).
- ⁹¹T. Sasaki, Y. Ukyo, and P. Novák, “Memory effect in a lithium-ion battery”, *Nat. Mater.* **12**, 569 (2013).
- ⁹²C. Jossierand, A. V. Tkachenko, D. M. Mueth, and H. M. Jaeger, “Memory effects in granular materials”, *Phys. Rev. Lett.* **85**, 3632 (2000).
- ⁹³T. Xie, “Tunable polymer multi-shape memory effect”, *Nature* **464**, 267 (2010).

- ⁹⁴R. Zwanzig, “Memory effects in irreversible thermodynamics”, *Phys. Rev.* **124**, 983 (1961).
- ⁹⁵H. Mori, “Transport, collective motion, and Brownian motion”, *Prog. Theor. Phys.* **33**, 423. (1965).
- ⁹⁶M. Te Vrugt, S. Hossenfelder, and R. Wittkowski, “Mori-Zwanzig formalism for general relativity: a new approach to the averaging problem”, *Phys. Rev. Lett.* **127**, 231101 (2021).
- ⁹⁷E. J. Parish and K. Duraisamy, “A dynamic subgrid scale model for large eddy simulations based on the Mori-Zwanzig formalism”, *J. Comput. Phys.* **349**, 154 (2017).
- ⁹⁸S. K. J. Falkena, C. Quinn, J. Sieber, J. Frank, and H. A. Dijkstra, “Derivation of delay equation climate models using the Mori-Zwanzig formalism”, *Proc. R. Soc. Lond. A* **475**, 20190075 (2019).
- ⁹⁹Z. Li, X. Bian, X. Li, and G. E. Karniadakis, “Incorporation of memory effects in coarse-grained modeling via the Mori-Zwanzig formalism”, *J. Chem. Phys.* **143**, 243128 (2015).
- ¹⁰⁰H. Meyer, T. Voigtmann, and T. Schilling, “On the non-stationary generalized Langevin equation”, *J. Chem. Phys.* **147**, 214110 (2017).
- ¹⁰¹G. Jung, M. Hanke, and F. Schmid, “Iterative reconstruction of memory kernels”, *J. Chem. Theory Comput.* **13**, 2481 (2017).
- ¹⁰²H. Meyer, S. Wolf, G. Stock, and T. Schilling, “A numerical procedure to evaluate memory effects in non-equilibrium coarse-grained models”, *Adv. Theory Simul.* **4**, 2000197 (2021).
- ¹⁰³L. L. Treffenstädt and M. Schmidt, “Memory-induced motion reversal in Brownian liquids”, *Soft Matter* **16**, 1518 (2020).
- ¹⁰⁴P. H. Hünenberger, *Thermostat algorithms for molecular dynamics simulations* (Springer, Berlin, Heidelberg, 2005).
- ¹⁰⁵J. Casas-Vázquez and D. Jou, “Temperature in non-equilibrium states: a review of open problems and current proposals”, *Rep. Prog. Phys.* **66**, 1937 (2003).
- ¹⁰⁶H. C. Andersen, “Molecular dynamics simulations at constant pressure and/or temperature”, *J. Chem. Phys.* **72**, 2384 (1980).
- ¹⁰⁷H. J. C. Berendsen, J. P. M. V. Postma, W. F. V. Gunsteren, A. R. H. J. DiNola, and J. R. Haak, “Molecular dynamics with coupling to an external bath”, *J. Chem. Phys.* **81**, 3684 (1984).
- ¹⁰⁸G. Bussi, D. Donadio, and M. Parrinello, “Canonical sampling through velocity rescaling”, *J. Chem. Phys.* **126**, 014101 (2007).
- ¹⁰⁹T. Soddemann, B. Dünweg, and K. Kremer, “Dissipative particle dynamics: a useful thermostat for equilibrium and nonequilibrium molecular dynamics simulations”, *Phys. Rev. E* **68**, 046702 (2003).
- ¹¹⁰J. E. Basconi and M. R. Shirts, “Effects of temperature control algorithms on transport properties and kinetics in molecular dynamics simulations”, *J. Chem. Theory Comput.* **9**, 2887 (2013).
- ¹¹¹M. Thomas and B. Corry, “Thermostat choice significantly influences water flow rates in molecular dynamics studies of carbon nanotubes”, *Microfluid. Nanofluid.* **18**, 41 (2015).

- ¹¹²X. Yong and L. T. Zhang, “Thermostats and thermostat strategies for molecular dynamics simulations of nanofluidics”, *J. Chem. Phys.* **138**, 084503 (2013).
- ¹¹³M. González-Pinto, J. Renner, D. de las Heras, Y. Martínez-Ratón, and E. Velasco, “Defects in vertically vibrated monolayers of cylinders”, *New J. Phys.* **21**, 033002 (2019).
- ¹¹⁴G. Cinacchi, L. Mederos, and E. Velasco, “Liquid-crystal phase diagrams of binary mixtures of hard spherocylinders”, *J. Chem. Phys.* **121**, 3854 (2004).
- ¹¹⁵S. Dussi, M. Chiappini, and M. Dijkstra, “On the stability and finite-size effects of a columnar phase in single-component systems of hard-rod-like particles”, *Mol. Phys.* **116**, 2792 (2018).

3 Publications




Full versions of the three publications contributing to this cumulative thesis are included in this chapter. The papers have already been published.

- [1] Custom flow in molecular dynamics p. 35
J. Renner, M. Schmidt, and D. de las Heras
Phys. Rev. Res. **3**, 013281 (2021)

- [2] Shear and bulk acceleration viscosities in simple fluids p. 47
J. Renner, M. Schmidt, and D. de las Heras
Phys. Rev. Lett. **128**, 094502 (2022)

- [3] Reduced-variance orientational distribution functions from torque sampling p. 61
J. Renner, M. Schmidt, and D. de las Heras
J. Phys.: Condens. Matter **35**, 235901 (2023)

Custom flow in molecular dynamics

Johannes Renner , Matthias Schmidt ,* and Daniel de las Heras [†]

Theoretische Physik II, Physikalisches Institut, Universität Bayreuth, D-95440 Bayreuth, Germany



(Received 7 December 2020; accepted 12 March 2021; published 26 March 2021)

Driving an inertial many-body system out of equilibrium generates complex dynamics due to memory effects and the intricate relationships between the external driving force, internal forces, and transport effects. Understanding the underlying physics is challenging and often requires carrying out case-by-case analysis. To systematically study the interplay between all types of forces that contribute to the dynamics, a method to generate prescribed flow patterns could be of great help. We develop a custom flow method to numerically construct the external force field required to obtain the desired time evolution of an inertial many-body system, as prescribed by its one-body current and density profiles. We validate the custom flow method in a Newtonian system of purely repulsive particles by creating a slow-motion dynamics of an out-of-equilibrium process and by prescribing the full time evolution between two distinct equilibrium states. The method can also be used with thermostat algorithms to control the temperature.

DOI: [10.1103/PhysRevResearch.3.013281](https://doi.org/10.1103/PhysRevResearch.3.013281)

I. INTRODUCTION

The precise application of a space- and time-resolved external force field can be used to drive a many-body system out of equilibrium in a controlled way. Analyzing the response of a system to an external field is a primary method to calculate transport coefficients [1] such as shear [2,3] and bulk [4,5] viscosities and the thermal conductivity [6]. Imposed pressure gradients, patterned substrates, capillary forces, electromagnetic fields, and centrifugal forces are examples of external fields that can be used in lab-on-a-chip devices [7] for the control of microflows [8]. However, the dynamics are complex due to far from trivial relationships between the external driving, the interparticle interactions, and transport effects. It is therefore difficult to predict the time evolution of a many-body system under the influence of an imposed external field, and case-by-case analyses are often required [9–11].

We consider here the inverse problem: to impose the desired dynamics and then find the corresponding external field. Such inversion, known as a closed-loop control system in control theory [12], is a valuable tool even at the level of individual particles. It allows, for example, the independent and simultaneous motion of several particles (that differ in either shape [13] or magnetic properties [14]) in arbitrary directions

using a single external magnetic field. Particles with different characteristics respond differently to the magnetic field and can therefore be transported in different directions. In other words, a unique magnetic field creates different external force fields for different particles. We focus here on many-body systems. We aim at specifying the dynamics of a many-body system of identical particles, as given by the time evolution of the one-body density and the one-body current fields, and then find, with computer simulations, the corresponding space- and time-resolved external field.

From a fundamental viewpoint, such inversion can be used to time-reverse the dynamics of a many-body system [15] and might offer new insights into irreversible processes [16,17]. The inversion can be also used as an alternative to Gauss's principle of least constraint [18] in order to impose constraints on a dynamical system. From an applied viewpoint, controlling the time evolution of the system instead of the external force acting on it can also be useful for the calculation of transport coefficients and relaxation times, especially in nanochannels where deviations from the Navier-Stokes formalism and from bulk behavior are expected [19–23]. The study of memory effects [24,25], the design of lab-on-a-chip devices [26,27], and the determination of the slip length at the nanoscale [28] can also benefit from such inverse methodology.

From a theoretical perspective, the existence in equilibrium of a unique mapping between the density distribution and the conservative external force forms the basis of quantum [29,30] and classical [31] density functional theory. In time-dependent quantum mechanical systems, the Runge-Gross theorem [32] ensures the existence of a unique mapping between the density distribution and a time-dependent external potential. A classical analog of the Runge-Gross theorem was proposed by Chan and Finken [33]. The existence of a unique mapping between the kinematic fields and the external force field plays a central role in power functional theory, an exact

*Matthias.Schmidt@uni-bayreuth.de; www.mschmidt.uni-bayreuth.de

[†]delasheras.daniel@gmail.com; <http://www.danieldelasheras.com/>.

Published by the American Physical Society under the terms of the Creative Commons Attribution 4.0 International license. Further distribution of this work must maintain attribution to the author(s) and the published article's title, journal citation, and DOI.

variational principle for nonequilibrium classical many-body overdamped Brownian [34] and Hamiltonian systems [35] as well as for many-body quantum systems [36].

The rapid increase in computational power has made possible the development of numerical inverse methods that implement these unique mappings in equilibrium for both classical [37,38] and quantum [39,40] systems. It is hence possible to prescribe an equilibrium density distribution and find the corresponding external potential that generates the density using, e.g., Monte Carlo simulations in the case of an equilibrium classical system. We have also developed a custom flow method for time-dependent overdamped Brownian systems [38]. The method is a valuable tool to generate specific flow and density patterns in a completely controlled way [15]. Custom flow is based on the exact one-body force balance equation that, in overdamped Brownian systems, relates the friction (against the solvent) force field, the internal force field, the external force field, and the thermal diffusion. Using Brownian dynamics simulations, custom flow finds the external force required to generate the desired (imposed) time evolution of both the one-body density and the one-body current distributions. We prescribe elements that enter into the force balance equation, namely, the density and the current distributions, and use an iterative scheme to find the generating external force field.

The force sampling method [41] uses a closely related idea: By sampling the one-body internal force field and using the force balance equation it is possible to obtain the one-body density distribution of an equilibrium system. The density distributions obtained using the forces acting on the particles [41–45] are more accurate than those obtained via the traditional counting of particles at space points.

Here, we present a custom flow method for classical many-body systems following Newtonian dynamics. The method is motivated by the exact one-body force balance equation (Sec. II A), and it constructs iteratively the external force field that is required to generate the desired (target) time evolution of both the density and the current distributions (Sec. II B). The method constitutes the solution of a complex inverse problem in statistical physics and implements numerically the map between the kinematic fields (density and current) and the external force field. Custom flow can be used with both conservative and nonconservative forces as well as with thermostats. We validate the method in a model system (Sec. III) of purely repulsive particles using several test cases (Sec. IV), including one with the Bussi-Donadio-Parrinello thermostat [46].

II. THEORY

A. One-body force balance equation

Consider a classical system with N identical and mutually interacting particles following Newtonian dynamics. The equations of motion of the i th particle are

$$\frac{d\mathbf{r}_i}{dt} = \frac{\mathbf{p}_i}{m}, \quad (1)$$

$$\frac{d\mathbf{p}_i}{dt} = \mathbf{f}_i, \quad (2)$$

where m is the mass of the particle, \mathbf{r}_i denotes its position, $\mathbf{p}_i = m\mathbf{v}_i$ is the momentum of the particle with \mathbf{v}_i being its

velocity, and \mathbf{f}_i is the total force acting on the particle,

$$\mathbf{f}_i = -\nabla_i u(\mathbf{r}^N) + \mathbf{f}_{\text{ext}}(\mathbf{r}_i, t), \quad (3)$$

which in general consists of an imposed time-dependent external contribution, $\mathbf{f}_{\text{ext}}(\mathbf{r}_i, t)$, and an internal contribution, $-\nabla_i u(\mathbf{r}^N)$. Here, ∇_i is the partial derivative with respect to \mathbf{r}_i , and $u(\mathbf{r}^N)$ is the interparticle potential energy with $\mathbf{r}^N = \{\mathbf{r}_1 \cdots \mathbf{r}_N\}$ being the complete set of particle positions.

In molecular dynamics (MD) simulations the equations of motion, (1) and (2), are integrated in time. The observables of interest can be obtained as space- and time-resolved one-body fields. For example, the one-body density distribution is given by

$$\rho(\mathbf{r}, t) = \left\langle \sum_{i=1}^N \delta(\mathbf{r} - \mathbf{r}_i) \right\rangle, \quad (4)$$

where $\delta(\mathbf{r})$ is the three-dimensional Dirac delta distribution, the sum runs over all particles N , and \mathbf{r} is the position vector. The brackets $\langle \cdot \rangle$ denote a statistical average, which out of equilibrium is done at each time t over different realizations of the initial conditions (that is, the positions and the velocities of the particles at the initial time $t_0 = 0$). Differentiation of Eq. (4) with respect to time yields the one-body continuity equation

$$\dot{\rho}(\mathbf{r}, t) = -\nabla \cdot \mathbf{J}(\mathbf{r}, t), \quad (5)$$

where the overdot indicates a time derivative and the one-body current is defined as

$$\mathbf{J}(\mathbf{r}, t) = \left\langle \sum_{i=1}^N \delta(\mathbf{r} - \mathbf{r}_i) \mathbf{v}_i \right\rangle. \quad (6)$$

Differentiating Eq. (6) and using Eqs. (1), (2), and (3) result in the exact one-body force balance equation

$$m\dot{\mathbf{J}}(\mathbf{r}, t) = \rho(\mathbf{r}, t)[\mathbf{f}_{\text{ext}}(\mathbf{r}, t) + \mathbf{f}_{\text{int}}(\mathbf{r}, t)] + \nabla \cdot \boldsymbol{\tau}(\mathbf{r}, t). \quad (7)$$

See, e.g., Ref. [35] for a more detailed derivation of Eq. (7). Here, the one-body internal force field is $\mathbf{f}_{\text{int}}(\mathbf{r}, t) = \mathbf{F}_{\text{int}}(\mathbf{r}, t)/\rho(\mathbf{r}, t)$, where \mathbf{F}_{int} is the internal force density field given by

$$\mathbf{F}_{\text{int}}(\mathbf{r}, t) = -\left\langle \sum_{i=1}^N \delta(\mathbf{r} - \mathbf{r}_i) \nabla_i u(\mathbf{r}^N) \right\rangle. \quad (8)$$

The last term in Eq. (7) describes the transport effects that arise due to the one-body description. This transport term involves the one-body kinetic stress tensor

$$\boldsymbol{\tau}(\mathbf{r}, t) = -m \left\langle \sum_{i=1}^N \delta(\mathbf{r} - \mathbf{r}_i) \mathbf{v}_i \mathbf{v}_i \right\rangle, \quad (9)$$

where $\mathbf{v}_i \mathbf{v}_i$ is a dyadic product such that $\boldsymbol{\tau}$ is of second rank.

B. Custom flow in inertial systems

We present here an iterative method to construct the external force that generates a prescribed time evolution of the one-body fields ρ and \mathbf{J} . The most general form of the iteration scheme reads

$$\mathbf{f}_{\text{ext}}^{(k+1)}(\mathbf{r}, t) = \mathbf{f}_{\text{ext}}^{(k)}(\mathbf{r}, t) + \alpha(\mathbf{J}(\mathbf{r}, t) - \mathbf{J}^{(k)}(\mathbf{r}, t)) + \beta(\dot{\mathbf{J}}(\mathbf{r}, t) - \dot{\mathbf{J}}^{(k)}(\mathbf{r}, t)) + \gamma \nabla \ln \frac{\rho(\mathbf{r}, t)}{\rho^{(k)}(\mathbf{r}, t)}. \quad (10)$$

Here, k denotes the iteration index, and α , β , and γ are free non-negative prefactors that in general can carry spatial and temporal dependencies. The fields ρ and \mathbf{J} are the prescribed (target) fields, and $\hat{\mathbf{J}}$ is also known since it follows directly from the prescribed \mathbf{J} via partial time derivative.

The procedure to find $\mathbf{f}_{\text{ext}}(\mathbf{r}, t)$ iteratively using Eq. (10) is the following: (i) Run an MD simulation, evolving all the initial microstates from t_0 to $t_0 + \Delta t$ and sampling the space-resolved one-body fields $\rho^{(k)}(\mathbf{r}, t_0 + \Delta t)$, $\mathbf{J}^{(k)}(\mathbf{r}, t_0 + \Delta t)$, and $\hat{\mathbf{J}}^{(k)}(\mathbf{r}, t_0 + \Delta t)$; (ii) use the sampled fields at iteration k to construct the external force for the next iteration $k + 1$ according to Eq. (10); and (iii) iterate until the process converges and the external force at time $t_0 + \Delta t$ is found. Convergence is achieved once the sampled fields $\rho^{(k)}$, $\mathbf{J}^{(k)}$, and $\hat{\mathbf{J}}^{(k)}$ are the same (within the desired numerical accuracy) as their target counterparts ρ , \mathbf{J} , and $\hat{\mathbf{J}}$. Next, advance the time from $t_0 + \Delta t$ to $t_0 + 2\Delta t$ and repeat the previous steps until the external force at $t_0 + 2\Delta t$ is found. The process is repeated for the complete time evolution which is discretized in time steps Δt .

The idea behind Eq. (10) is simple but very useful: At each time, the external force at iteration $k + 1$ is that at the previous iteration k plus terms that (i) correct the deviations in the sampled fields with respect to the target fields and (ii) vanish if the target and sampled fields are identical. For example, if the current at a given position is higher (lower) than the desired one, the external force at that position decreases (increases) in the next iteration. Other correction terms are possible provided that they change the external force at each iteration in the right direction. For example, the third term on the right-hand side of Eq. (10) can be replaced by something like $\gamma \nabla(\rho - \rho^{(k)})$. The precise form of Eq. (10) is motivated by the exact force balance equation, as we show in Appendix.

The non-negative prefactors α , β , and γ control how much the external force changes in one iteration. Using the exact one-body force balance equation (7), we obtain suitable expressions for them (see Appendix for a detailed calculation):

$$\alpha(\mathbf{r}, t) = \frac{m}{\rho(\mathbf{r}, t)\Delta t}, \quad (11)$$

$$\beta(\mathbf{r}, t) = \frac{m}{\rho(\mathbf{r}, t)}, \quad (12)$$

$$\gamma = k_B T_0. \quad (13)$$

Here, k_B is the Boltzmann constant, and T_0 denotes the temperature of the initial state. Recall that the above expressions for α , β , and γ are not unique. The prefactors only fix the amount of change between two iterations. The method can in principle be also implemented by simply using non-negative constant prefactors. Also, not all three prefactors need to be present. Actually, having only α or only β is sufficient to find the external force iteratively. In cases for which the time-dependent density distribution ρ determines the full dynamical evolution of the system it is also possible to work only with the coefficient γ . Such cases occur only if the current is free of both rotational and harmonic terms such that ρ alone fully determines \mathbf{J} via Eq. (5).

In our particular implementation of Eq. (10) we iterate using only the target and sample currents. Hence we set α to

the value in Eq. (11) and set both β and γ to zero. Then, the iterative custom flow method we use here reads

$$\mathbf{f}_{\text{ext}}^{(k+1)}(\mathbf{r}, t) = \mathbf{f}_{\text{ext}}^{(k)}(\mathbf{r}, t) + \frac{m}{\rho(\mathbf{r}, t)\Delta t} (\mathbf{J}(\mathbf{r}, t) - \mathbf{J}^{(k)}(\mathbf{r}, t)). \quad (14)$$

This iteration scheme is repeated at every Δt . That is, we use Eq. (14) to iteratively find $\mathbf{f}_{\text{ext}}(\mathbf{r}, t_0 + \Delta t)$. We then advance time to $t_0 + 2\Delta t$ and use Eq. (14) to find $\mathbf{f}_{\text{ext}}(\mathbf{r}, t_0 + 2\Delta t)$. The process repeats until the complete time evolution is found.

The same algorithm can be used to find a suitable collection of initial microstates at t_0 such as, e.g., microstates from an equilibrium system with a prescribed one-body density distribution. To this end, we can start with a homogeneous equilibrium system and use custom flow to find microstates of another equilibrium system with the desired density distribution that serves as our initial state at t_0 . Alternatively, such an initial set of microstates can be also found using the inversion between the external field and the density distribution for equilibrium systems described in Ref. [38].

At each time we initialize the iterative process ($k = 0$) using the external force

$$\mathbf{f}_{\text{ext}}^{(0)}(\mathbf{r}, t) = \frac{m\hat{\mathbf{J}}(\mathbf{r}, t)}{\rho(\mathbf{r}, t)}, \quad (15)$$

which follows by making both \mathbf{f}_{int} and $\nabla \cdot \boldsymbol{\tau}$ zero everywhere in Eq. (7). Another possible initialization is to include the contributions of the internal force and the kinetic stress tensor at the previous sampling time step Δt on the right-hand side of Eq. (15).

In principle the time step Δt can be as small as the integration time step dt of the MD simulation. In practice, however, we use a larger time step ($\Delta t/dt = 10$) that does not compromise the accuracy of the calculation but still reduces the computational effort. In the MD integration algorithm of the equations of motion, we keep the external force constant between two consecutive time steps, t and $t + \Delta t$. Interpolating the external force between two consecutive time steps can be problematic in cases where \mathbf{f}_{ext} changes drastically (such as, e.g., if an external force is switched on at a specific time).

The iteration scheme (14) is particularly well suited since it is general and it requires us to sample only $\mathbf{J}^{(k)}$ in order to find the external force for the next iteration $k + 1$. Sampling of $\hat{\mathbf{J}}$, which can be done by individually sampling the terms on the right-hand side of Eq. (7), is therefore not required. The proposed version of custom flow in Eq. (14) does not require knowledge of any additional contribution or modification to the one-body force balance equation that might arise if, e.g., a thermostat algorithm acts on the many-body level. As we demonstrate below, our method works also with thermostats.

III. MODEL AND SIMULATION DETAILS

We implement the method in a system of $N = 50$ particles that interact via the purely repulsive Weeks-Chandler-Andersen interparticle-interaction potential [47]:

$$\phi(r) = \begin{cases} 4\epsilon \left[\left(\frac{\sigma}{r}\right)^{12} - \left(\frac{\sigma}{r}\right)^6 + \frac{1}{4} \right] & \text{if } r \leq r_c \\ 0 & \text{otherwise.} \end{cases} \quad (16)$$

Here, r is the distance between two particles, σ is the length scale, ϵ is the energy scale, and $r_c/\sigma = 2^{1/6}$ is the cutoff radius which is set at the minimum of the 12-6 Lennard-Jones potential. We use $\tau = \sqrt{m\sigma^2/\epsilon}$ as the time scale.

The particles are located in a periodic three-dimensional simulation box with lengths L_x , L_y , and L_z . The origin of coordinates is located at the center of the simulation box. The system is inhomogeneous only in the \hat{x} direction, which is discretized with bins of size 0.05σ . The system remains homogeneous and without average flow in the other two directions, \hat{y} and \hat{z} .

The many-body equations of motion, Eqs. (1) and (2), are integrated in time using the velocity Verlet algorithm [48] with an integration time step $dt/\tau = 10^{-4}$. The particle positions are initialized randomly with the condition that the particles do not interact with each other (all interparticle distances are larger than r_c). The particle velocities are initialized according to a Maxwell-Boltzmann distribution. Hence each velocity component is generated from a Gaussian distribution with zero mean and standard deviation $\sqrt{2k_B T/m}$ with T absolute temperature, which needs to be prescribed. The center of mass is set initially at rest. We then let the system equilibrate for 1τ with no external force applied.

For the custom flow method we use a time step of $\Delta t/dt = 10$ and average at each time over 2×10^6 trajectories (different realizations of the initial positions and velocities of the particles at $t = 0$) to obtain accurate results. Since the time step Δt is small and the prefactor α has been carefully selected, only three iterations are required at each time for the method to converge to the desired external force. The one-body fields are sampled at every Δt and used according to Eq. (14) to find the external force for the next iteration.

IV. RESULTS

We illustrate the validity of the method with three examples. In Sec. IV A we measure the time evolution of the one-body fields ρ and \mathbf{J} in a system subject to a spatially inhomogeneous external force which is switched on at $t = 0$ and then kept constant in time. We next construct the time-dependent external force required to slow down the observed dynamics by an arbitrarily prescribed factor. In Sec. IV B, we incorporate a thermostat to demonstrate its easy implementation within custom flow. Finally, in Sec. IV C, we prescribe the full time evolution of the one-body density and the one-body current and then find the corresponding external force.

A. Slow-motion dynamics

As a first example, we use custom flow to modify the time scale of a dynamical process. The particles are located in a box with dimensions $L_x/\sigma = 4$, $L_y/\sigma = 8$, and $L_z/\sigma = 10$. We start with a homogeneous system at equilibrium at $t = 0$ and initial temperature $k_B T/\epsilon = 0.5$. Then, we switch on the following external potential:

$$V(x) = V_0 \cos\left(\frac{4\pi x}{L_x}\right), \quad (17)$$

with $V_0/\epsilon = 1$. Hence the corresponding external force, which is constant in time for $t > 0$, acts only in the \hat{x} direction

$$\mathbf{f}_{\text{ext}}(x) = -\nabla V(x) = V_0 \frac{4\pi}{L_x} \sin\left(\frac{4\pi x}{L_x}\right) \hat{\mathbf{x}}. \quad (18)$$

We let the system evolve for a total time of 10τ , which is long enough to reach proximity to a new equilibrium state with an inhomogeneous density profile. The time evolution of the one-body density and current profiles is shown in Figs. 1(a) and 1(b), respectively. The external force field, shown in Fig. 1(c), accelerates the particles toward the minima of the external potential, located at $x/\sigma = \pm 1$. Two density peaks grow from the homogeneous density distribution at $t = 0$, reaching the largest amplitude at $t/\tau \approx 0.65$. At short times, the shape of the one-body current resembles that of the external force (sine wave), and it increases in amplitude until it reaches its largest value at $t/\tau \approx 0.3$. Then, the amplitude of the current decreases until the current starts to flip sign, which occurs when the density peaks reach the largest amplitude ($t/\tau \approx 0.65$). Next, the density peaks decrease in amplitude and get broader since only some particles have enough momentum to overcome the external potential barrier. Most particles, however, cannot overcome the potential barrier. Instead, they partially climb the barrier (contributing to the broadening of the density peaks). Then, once the kinetic energy of the particles has been transformed into external energy, the particles start to move backwards towards the minima of the potential. This backward motion leads to an increase in the density peaks, and the process repeats again in time. Now, however, the process is less intense since both the energy stored in the current and the external energy have been partially dissipated due to, e.g., interparticle collisions and converted into thermal energy. The described time evolution repeats in time creating a damped oscillatory behavior. Eventually, the system reaches an equilibrium state at $t/\tau \approx 9.5$ with vanishing one-body current (within our numerical accuracy). Recall that this highly non-trivial time evolution of the one-body density and current profiles is produced by a simple external force [see Eq. (18)] that is switched on at $t = 0$ and then kept constant in time. A video showing the time evolution of the one-body fields is provided in the Supplemental Material [49].

Next, we use custom flow to find the external force required to reproduce this complex dynamics but in slow motion, i.e., slowed down by an arbitrarily chosen factor. By changing the time scale of the process we expect the external force of the slow-motion system to be time dependent, which is indeed the case. We want to scale the time by a factor a . Hence, in the new system the density profile ρ_a at time t is the same as the density profile in the original system at time at . That is, $\rho_a(\mathbf{r}, t) = \rho(\mathbf{r}, at)$. The time derivative in the continuity equation (5) implies that the current in the new system is also scaled by a factor a . That is, $\mathbf{J}_a(\mathbf{r}, t) = a\mathbf{J}(\mathbf{r}, at)$. Therefore scaling the time leads to a factor a in front of the current that needs to be considered when prescribing the target fields. Similarly, the time derivative of the current gets an additional scaling factor $\dot{\mathbf{J}}_a(\mathbf{r}, t) = a^2\dot{\mathbf{J}}(\mathbf{r}, at)$.

In Figs. 1(d)–1(f) we show the slow-motion dynamics with scaling factor $a = 0.5$. Hence the slow motion runs for 20τ , i.e., twice the original total time. The sampled one-body density and current profiles coincide with their target. The time

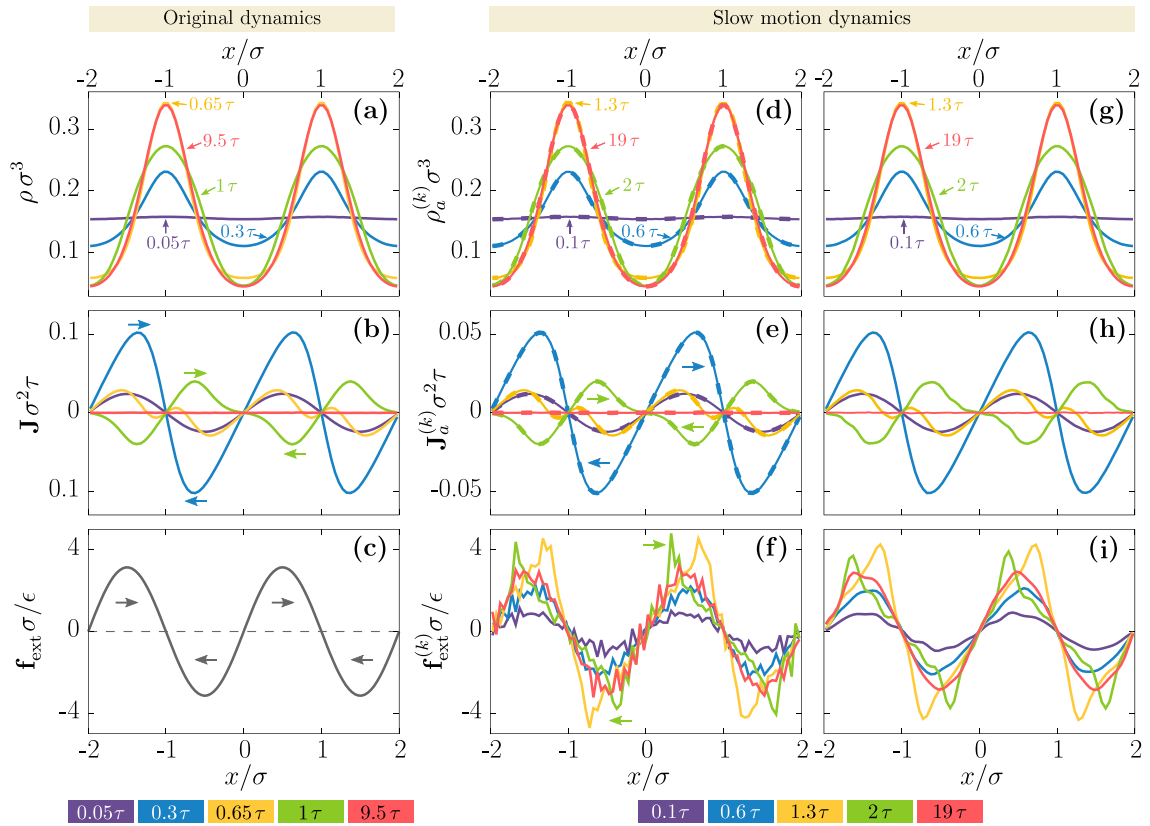


FIG. 1. Time evolution of the density (a) and the current (b) profiles of a system under the influence of a sinusoidal external force (c). The profiles in (a) and (b) are colored according to time, as indicated. Both \mathbf{J} and \mathbf{f}_{ext} act along the $\hat{\mathbf{x}}$ axis. The horizontal arrows illustrate the direction of the vector field at specific regions (position of the arrow) and also times (color). Sampled (solid lines) density (d) and current (e) profiles of a slow-motion system with dynamics slowed down by a factor $a = 1/2$ [note that the indicated times are twice those in (a) and (b)]. The dashed lines indicate the target profiles. (f) External force, color-coded as in (d), obtained with custom flow, that produces the slow-motion dynamics. Sampled density (g) and current (h) profiles for a system under the influence of the external force field (i), which is a smoothed version of that shown in (f). The set of initial microstates used to obtain the averaged fields in the second and in the third column are not the same. A video showing the time evolution is provided in the Supplemental Material [49].

evolution of the one-body density [Fig. 1(d)] is the same as in the original system [Fig. 1(a)], but it proceeds only at half speed. Similarly, the evolution of the one-body current [Fig. 1(e)] is two times slower, and the amplitude is half of the original target current profiles [Fig. 1(b)]. The time-dependent external force that generates the slow motion (found with custom flow) is shown in Fig. 1(f). At short times the shape of the external force resembles that in the original system [Fig. 1(c)], but its amplitude is reduced by a factor of 4. This was expected since at $t = 0$ the system is in equilibrium under no external force. That is, at $t = 0$ both $\nabla \cdot \boldsymbol{\tau}$ and \mathbf{F}_{int} are homogeneous and cancel each other in Eq. (7). At short times, only \mathbf{J}_a contributes to the external force in the force balance equation; hence the external force has the same shape as in the original system, but it is rescaled by a factor a^2 since $\mathbf{J}_a = a^2 \mathbf{J}$ as discussed above.

Although the maximum amplitude of the density peaks occurs at 1.3τ , the amplitude of the external force continues to grow, and its shape deviates from a sinusoidal wave. The maxima and the minima of the external force are shifted towards the location of the density peaks at $x/\sigma = \pm 1$. While the amplitude of the density profile decreases, the extrema of

the external force shift towards the minima of the one-body density at $x = 0$ and $x/\sigma = \pm 2$.

When the slow-motion system reaches the equilibrium state, the shape of the external force resembles that in the original system, but interestingly, the amplitude is slightly smaller in the slow-motion system. In slow motion, less energy is dissipated due to the reduced value of the one-body current. Hence also the temperature is slightly different. For the original time evolution the final temperature after equilibrium is reached is $k_B T/\epsilon = 0.77$, and in slow motion it is $k_B T/\epsilon = 0.68$ [50]. This temperature difference is responsible for the different amplitudes of the external force. Note that in equilibrium the transport term reduces to

$$\nabla \cdot \boldsymbol{\tau} = -k_B T \nabla \rho. \quad (19)$$

Hence, according to Eq. (7) it is clear that two equilibrium systems with the same density distribution but at different temperatures are generated by external forces with different amplitudes.

Robustness of the external force. Custom flow generates a noisy external force; see Fig. 1(f). The iterative scheme, Eq. (14), minimizes the error in the current profile since it

is designed to converge if target and sampled currents coincide. As a result, the statistical fluctuations in \mathbf{J} are directly translated into the external force field. Such fluctuations arise due to the finite number of realizations (recall that at each time we average over 2×10^6 trajectories that have evolved from different realizations of the initial particle positions and velocities). One could then think that the external force is tailored to the set of initial conditions and cannot be used in other circumstances. We demonstrate in the following that this is not the case and that the external force is indeed quite robust and independent of the small details. To this end, we first smooth the external force in Fig. 1(f) using a Fourier transform and eliminating the high-frequency modes (only the lowest 15 modes are retained). The smoothed external force is depicted in Fig. 1(i). Next, using the smoothed external force and also a different set of initial conditions (with the same number of microstates, i.e., 2×10^6), we sample the time evolution of the density and the current one-body fields, shown in Figs. 1(g) and 1(h), respectively.

Both the density and the current profiles obtained with the original external force and with the smoothed external force and a different set of initial conditions are similar and reproduce accurately the target profiles. Of course, small differences occur; compare, e.g., the current profiles at $t/\tau = 1$ in Figs. 1(e) and 1(h). Hence we conclude that custom flow is suitable to reproduce the prescribed dynamics using other sets of initial conditions provided that enough trajectories are used. Furthermore, we want to stress that for the cases considered here the noise in the external force is not relevant to generate the target fields ρ and \mathbf{J} . We expect that other filters that keep the structure and eliminate the noise can also be used to smooth the external force.

B. Thermostats

It is often the case that MD simulations are performed at constant temperature. In the following we show that custom flow is also valid with algorithms to control the temperature (thermostats). Several types of thermostats can be implemented in MD [51]. In general, a thermostat acts on the many-body level by rescaling the particle velocities and modifying therefore the equations of motion and the integration algorithm. Hence thermostats generate new terms in the one-body force balance equation (7). However, custom flow is designed such that sampling of these terms is not required to advance the iterative process. Custom flow uses only the external force at the previous iteration and the sampled current field [cf. Eq. (14)]. The external force constructed with custom flow changes, of course, if a thermostat is used, but the implementation of the method remains unchanged.

To illustrate the use of thermostats, we implement the well-known Bussi-Donadio-Parrinello (BDP) thermostat [46], an extension of the Berendsen thermostat [52], that stochastically ensures a thermalized distribution of the kinetic energy.

Out of equilibrium, the kinetic energy has a contribution due to the net flow of the system

$$E_{\text{flow}} = \frac{m}{2} \int d\mathbf{r} \rho \mathbf{v}^2, \quad (20)$$

which is unrelated to the temperature [51]. To control the temperature considering only the velocity fluctuations around the mean velocity [53], we can rescale the particle velocities using only the thermal kinetic energy:

$$E_{\text{thermal}} = \left\langle \frac{m}{2} \sum_{i=1}^N (\mathbf{v}_i - \mathbf{v})^2 \right\rangle, \quad (21)$$

where it is important to note that $\mathbf{v}(\mathbf{r}, t)$ is the space- and time-dependent velocity profile (and not the center of mass velocity). The implementation of Eq. (21) is particularly simple within custom flow since the velocity profile is known in advance.

To demonstrate that custom flow can be used with thermostats, we find the external force that generates the same time evolution of ρ and \mathbf{J} as that in Figs. 1(a) and 1(b) but using the BDP thermostat. We set the time constant (required in the algorithm to control the temperature) to five times the integration time step dt of the simulation. We show in Fig. 2 results from both using the total kinetic energy and using only the thermal energy [Eq. (21)] to rescale the velocities.

The sampled one-body density and one-body current are displayed in Figs. 2(a) and 2(b), respectively. The results from both thermostats are on top of each other and are indistinguishable from the case without a thermostat [Fig. 1]. In Fig. 2(c) we show the external force constructed with custom flow and smoothed using the same procedure as discussed above. We have verified that the smoothed external force also reproduces the target time evolution. The inclusion of the thermostat has a strong influence on the external force, which is now time dependent, in contrast to the original (constant energy) dynamics for which the external force is constant in time [Eq. (18)]. Furthermore, the external force required to produce the desired dynamics depends on the thermostat. This is clearly visible at, e.g., $t/\tau = 0.35$, at which the current profile has its largest amplitude. At that time the flow kinetic energy has also its largest value, and hence the two versions of the thermostat rescale the velocities differently. Differences are also noticeable both in the internal force field [see Fig. 2(e)] and especially in the transport term $\nabla \cdot \boldsymbol{\tau}$ [Fig. 2(f)], since $\boldsymbol{\tau}$ is directly related to the total kinetic energy [cf. Eq. (9)].

Custom flow can help us to understand how different thermostat algorithms modify the physical properties of a system. In Fig. 2(c) we plot the external force at $t/\tau = 0.35$ calculated by using the sampled \mathbf{f}_{int} and $\nabla \cdot \boldsymbol{\tau}$ in the force balance equation (A1), which is exact only without thermostats. Using the thermal kinetic energy in the BDP thermostat results in an approximated external force, via Eq. (A1), that is almost on top of the actual force generated with custom flow. The external force obtained with the original BDP thermostat (which uses the total kinetic energy) via the force balance equation (A1) shows a clear deviation from the force obtained in custom flow. We therefore conclude that using the total kinetic energy in the BDP thermostat induces a nontrivial contribution to the force balance equation that alters the flow. In contrast, using the thermal energy, only the velocity fluctuations are rescaled, and the flow is left unchanged.

As expected, the time derivative of the current $\dot{\mathbf{J}}$ [Fig. 2(d)] is very small for $t = 0.35\tau$ since \mathbf{J} reaches at that time the

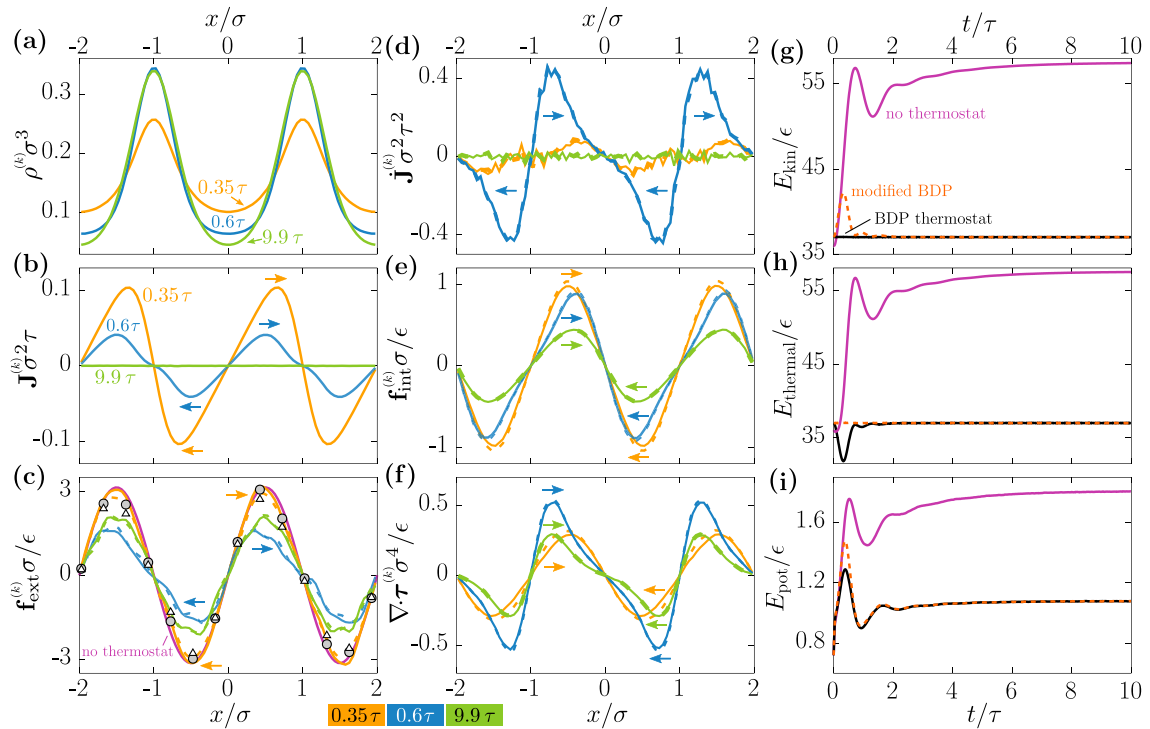


FIG. 2. Time evolution of a system with target ρ and \mathbf{J} like those in Figs. 1(a) and 1(b), respectively, but under the influence of either the BDP thermostat (solid lines) or the modified BDP thermostat (dashed lines). Three different times are displayed: $t/\tau = 0.35$ (yellow), $t/\tau = 0.6$ (blue), and $t/\tau = 9.9$ (green). (a) Density profile ρ , (b) current profile \mathbf{J} , (c) external force \mathbf{f}_{ext} , (d) time derivative of the current \mathbf{J} , (e) internal force \mathbf{f}_{int} , and (f) transport term $\nabla \cdot \boldsymbol{\tau}$. All vector fields act along the $\hat{\mathbf{x}}$ axis. The horizontal arrows in (b)–(f) indicate the direction of the respective field at specific regions and times, as indicated by the position and the color of the arrow, respectively. The violet line in (c) indicates the constant-in-time external force that generates the target fields ρ and \mathbf{J} if no thermostat is present. The gray circles (white triangles) in (c) show the external force calculated via the force balance equation for the BDP (modified BDP) thermostat at time $t/\tau = 0.35$. The third column shows the time evolution of the kinetic (g), thermal (h), and potential (i) energies in the case of no thermostat (violet lines), a BDP thermostat (black lines), and a modified BDP thermostat (dashed orange lines).

maximum amplitude. Also for $t/\tau \geq 9.9$ the system is very close to equilibrium, and \mathbf{J} vanishes within the numerical accuracy.

Finally, we show in Figs. 2(g), 2(h), and 2(i) the time evolution of the total kinetic energy, the thermal energy, and the internal potential energy, respectively. Shown are the original dynamics (no thermostat) and both the BDP thermostat and the modified version that uses only the thermal kinetic energy. The total kinetic energy is constant in time for the BDP thermostat as it should be by construction. In the modified version, the thermal kinetic energy [Fig. 2(h)] is constant in time, but the total kinetic energy varies with time since the flow kinetic energy is kept unchanged. The original time evolution is clearly not at constant temperature since both the kinetic energy and the thermal kinetic energy vary substantially over time. The total internal potential energy is for neither thermostat constant in time [Fig. 2(i)]. For a short period of time around $t/\tau = 0.35$ there is a significant difference between both versions of the BDP thermostat due to the large amplitude of the one-body current.

Custom flow can be used as a new tool to analyze the quality and the physical consequences of the inclusion of thermostats in the dynamics of many-body systems. We have shown here that separating the flow and thermal kinetic en-

ergies, especially in systems with large magnitude of the one-body current, is advisable.

C. Tailoring inhomogeneous density profiles

In the previous examples we obtained ρ and \mathbf{J} in a simulation for a fixed external force and used modified versions of them as target fields. In this last example, we show that there is freedom to prescribe the fields provided that they represent a physical system. For example, the target ρ and \mathbf{J} must obey the continuity equation.

We set a simulation box with dimensions $L_x/\sigma = 10$, $L_y/\sigma = 5$, and $L_z/\sigma = 5$ and prescribe the one-body density

$$\rho(x, t) = \rho_0 - \frac{A}{2} \cos\left(\frac{4\pi x}{L_x}\right) \left[1 - \cos\left(\frac{\pi t}{T_0}\right)\right], \quad (22)$$

with average density $\rho_0 = N/(L_x L_y L_z) = 0.2\sigma^{-3}$ and constants $A\sigma^3 = 0.05$ (maximum amplitude of the density inhomogeneity) and $T_0/\tau = 0.5$. At $t = 0$ the density is homogeneous [see Eq. (22)], and the system is in equilibrium. The density profile evolves according to Eq. (22) for $0 < t < T_0$ (two peaks grow from the initial homogeneous state). At $t \geq T_0$ the one-body current is set to zero everywhere, and

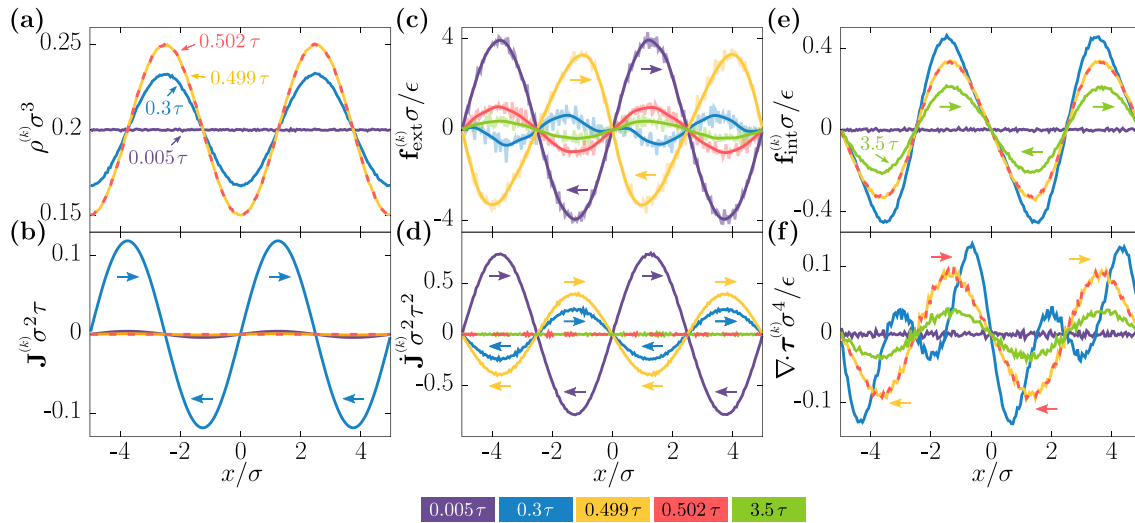


FIG. 3. Sampled one-body (a) density ρ and (b) current \mathbf{J} profiles at different times, as indicated. The target fields are prescribed according to Eqs. (22) and (23). (c) External force field constructed with custom flow (semitransparent lines) and smoothed external force (solid lines). Sampled (d) time derivative of the current profile $\dot{\mathbf{J}}$, (e) internal force density \mathbf{f}_{int} , and (f) transport term $\nabla \cdot \boldsymbol{\tau}$. All vector fields act along the \hat{x} axis. The horizontal arrows indicate the direction of the respective field at specific regions (arrow's position) and times (arrow's color). The Supplemental Material [49] contains a movie showing the time evolution.

therefore the inhomogeneous density profile remains stationary.

The target current \mathbf{J} follows from Eq. (22) and the space integral of the continuity equation (5):

$$J_x = - \int dx \dot{\rho} + C, \quad (23)$$

with J_x being the x component of \mathbf{J} and C being a constant that we set such that the total integral of the current vanishes, $\int dx J_x = 0$. That is, for convenience we choose to not have motion of the center of mass. We calculate the target current analytically using Eq. (23). Note that in our effective one-dimensional system with periodic boundary conditions the time evolution of ρ determines the current \mathbf{J} up to a constant only. However, in higher dimensions the continuity equation alone is not enough to determine the current from the time evolution of the density profile since any divergence-free field can be added to the current without altering ρ .

Using custom flow to construct the external force that generates the time evolution prescribed in Eq. (22) yields the results shown in Fig. 3 (a movie is also included in the Supplemental Material [49]). Figures 3(a) and 3(b) show for different times the sampled one-body density and the one-body current, respectively. Both fields are in perfect agreement with their respective target fields [cf. Eqs. (22) and (23)]. The largest amplitude in \mathbf{J} occurs at $t/\tau = 0.25$, which is also the time of the largest change in the density profile. The constructed external force, shown in Fig. 3(c), is highly nontrivial, and it is closely related to the behavior of \mathbf{J} , shown in Fig. 3(d). Initially, the external force accelerates the particles towards the maxima of the one-body density. Then, around $t/\tau = 0.25$ the external force flips sign and decelerates, therefore, the particles. At $t/\tau = 0.5$ there is a jump in the time evolution of the external force due to the imposed vanishing $\dot{\mathbf{J}}$ (compare the profiles at $t/\tau = 0.499$ and 0.502). Custom flow finds the

correct external force despite this drastic change in time. After \mathbf{J} vanishes, neither ρ nor \mathbf{J} changes anymore. Interestingly, the external force continues to evolve in time. This can be explained by memory effects occurring in both the internal force field \mathbf{f}_{int} [Fig. 3(e)] and the transport term $\nabla \cdot \boldsymbol{\tau}$ [Fig. 3(f)]. Even though \mathbf{J} vanishes at $t/\tau > 0.5$, the external force still needs to vary in time in order to cancel the time evolution of the internal and the transport terms. Custom flow is therefore a valuable tool to study memory effects [24,25,54–56] since it allows us to isolate memory contributions in the force balance equation from the time evolution of the density and the current fields.

V. DISCUSSION AND CONCLUSIONS

We have presented a numerical iterative scheme [see Eqs. (10) and (14)] to construct the external force required to achieve a given (prescribed) time evolution of a Newtonian many-body system, as specified by the one-body density and the one-body current. We have previously shown how in overdamped Brownian dynamics the exact one-body force balance equation can be directly used to construct a reliable custom flow method [38]. The external force is generated as the sum of different contributions that are sampled in the simulation. Here, we have followed a different and more general approach. We construct iteratively the external force by adding at each iteration terms that correct the external force in the right direction and that vanish when target and sample fields coincide. Although we have restricted ourselves here to inertial molecular dynamics, the method is general and can be also used in, e.g., overdamped Brownian dynamics and Langevin dynamics. There the corresponding force balance equation can be used to recalculate suitable expressions for the prefactors α , β , and γ since they might be different.

The more general iterative scheme, Eq. (10), modifies the external force based on three types of target-sampled

differences that occur in the gradient of the density, in the current, and in the time derivative of the current. This is analogous to the three different fundamental equations in classical mechanics: d'Alembert's principle based on particle displacements, Jourdain's principle based on variations in particle velocities, and the Gibbs-Appell-Gauss principle based on variations in particle accelerations. It is therefore not surprising that only one prefactor, α , β , or γ , in Eq. (10) needs to be present (using only γ is restricted to curl-free target current profiles as discussed in Sec. II B).

Since the calculation of the external force requires us to sample only the current, but not the individual contributions to the force balance equation, it is straightforward to use custom flow together with a thermostat. Applying custom flow to systems with the same target fields but different thermostat algorithms provides new insight into the different mechanisms to control the temperature since it is possible to precisely analyze how the individual contributions to the force balance equation are affected by different thermostats. The choice of thermostat can heavily influence the results [57,58], and custom flow might help us to make an educated selection as to how to control the temperature out of equilibrium, which is a delicate issue [59].

The external field controls the density and the velocity profiles, but it does not determine the fluctuations of the particle velocities around the mean velocity. Hence we do not expect that custom flow can be used in general to construct an ideal thermostat able to maintain a temperature profile constant in time and uniform in space. However, it might be possible to generalize custom flow to include a new external field that produces such a temperature profile by acting on the particle velocities. The new spatially and temporally resolved field could then be found iteratively by comparing the target and the desired thermal kinetic energy fields [cf. Eq. (21)].

Custom flow can be used to prescribe target fields such that at least one contribution to the force balance equation vanishes. For example, the current vanishes after a certain time in the example of Sec. IV C. This can facilitate the study of memory effects and the structure of memory kernels, a topic of current interest [24,25,54–56].

The external forces constructed with custom flow are in general noisy since they are tailored to the finite set of initial microstates used during the iterative process. Nevertheless, we have shown that a smoothed version of the external force, constructed by filtering out the high-frequency terms, also produces the target dynamics within the numerical accuracy. We note, however, that we have stayed away from instabilities that might be the source of convergence issues.

Although they are only model situations, the examples considered here are demanding; the target fields vary substantially over distances comparable to the particle size, and we have designed a case in Sec. IV C for which the resulting external force is discontinuous in time. Custom flow has in all cases found the external force field that produces the target fields within the numerical accuracy. Nevertheless, convergence issues can occur, e.g., in strongly driven systems, in flows with rapid spatial variations, and near the onset of mechanical and fluid instabilities. Integer arithmetic [17,60] and using small values for the prefactors α , β , and γ might help to mitigate some of the problems that might appear.

The existence of a unique mapping between the density distribution and a time-dependent external potential is at the core of time-dependent density functional theory [33]. Such mapping is not completely general but is restricted to the occurrence of gradientlike forces only. Similarly, in the widely spread dynamical density functional theory [31,61], the internal force field is drastically approximated as a functional of the density distribution only. No functional dependence on the flow occurs. These limitations are solved in the formally exact power functional theory [34,35] that considers a functional dependence on all kinematic fields. Such dependence is required to properly describe, e.g., shear migration [62], phase coexistence of active particles [63], and laning formation in binary mixtures [64]. Power functional theory relies on a mapping between the external force and both the density and the current distributions. Such mapping is indispensable to, e.g., describe systems in which the current field contains nongradient contributions (i.e., rotational and harmonic contributions) since the continuity equation links only the divergence of the current and the time evolution of the density profile. It is therefore perfectly possible to construct families of systems that, e.g., share the same time evolution of the density profile but have different current profiles [15] and are therefore generated by different external forces. Custom flow provides the numerical evidence of the existence of the unique mapping between the external force and the kinematic fields.

Custom flow has proven to be an excellent tool to develop approximated power functionals in overdamped Brownian systems [15], and we expect it to be also of great help to develop approximate power functionals in Newtonian systems. To study large-scale systems, it can be useful to extend custom flow to adaptive resolution techniques for multiscale molecular dynamics simulations [65–68]. The extension of custom flow to multicomponent systems is of both applied and fundamental interest. It would allow us to, e.g., explore up to what extent the dynamics of a collection of interacting particles that differ in, e.g., their shape can be controlled using a single external field such as, e.g., a magnetic field.

ACKNOWLEDGMENTS

We thank Sophie Hermann for a critical reading of the manuscript. This work is supported by the German Research Foundation (DFG) via Project No. 447925252. The publication costs were funded by the DFG and the University of Bayreuth in the funding program Open Access Publishing.

APPENDIX: PREFACTORS FROM THE FORCE BALANCE EQUATION

We start with the exact one-body force balance equation (7). Solving for the external force field yields

$$\mathbf{f}_{\text{ext}}(\mathbf{r}, t) = \frac{m\mathbf{J}(\mathbf{r}, t)}{\rho(\mathbf{r}, t)} - \mathbf{f}_{\text{int}}(\mathbf{r}, t) - \frac{\nabla \cdot \boldsymbol{\tau}(\mathbf{r}, t)}{\rho(\mathbf{r}, t)}. \quad (\text{A1})$$

Following the ideas of Ref. [38], it is possible to establish an iteration scheme to find the external force at iteration

$k + 1$ as

$$\mathbf{f}_{\text{ext}}^{(k+1)}(\mathbf{r}, t) = \frac{m\dot{\mathbf{J}}(\mathbf{r}, t)}{\rho(\mathbf{r}, t)} - \mathbf{f}_{\text{int}}^{(k)}(\mathbf{r}, t) - \frac{\nabla \cdot \boldsymbol{\tau}^{(k)}(\mathbf{r}, t)}{\rho(\mathbf{r}, t)}. \quad (\text{A2})$$

Here, the unknown terms on the right-hand side of Eq. (A1), i.e., the internal force field and the kinetic stress tensor, are sampled at each iteration and used to construct the external force iteratively. This idea, which works in overdamped Brownian systems [38], presents stability issues in inertial systems and does not converge in general. We next observe that the one-body force balance equation (7) implies that for iteration k

$$\mathbf{f}_{\text{ext}}^{(k)}(\mathbf{r}, t) = \frac{m\dot{\mathbf{J}}^{(k)}(\mathbf{r}, t)}{\rho^{(k)}(\mathbf{r}, t)} - \mathbf{f}_{\text{int}}^{(k)}(\mathbf{r}, t) - \frac{\nabla \cdot \boldsymbol{\tau}^{(k)}(\mathbf{r}, t)}{\rho^{(k)}(\mathbf{r}, t)}. \quad (\text{A3})$$

Combining Eqs. (A2) and (A3) yields

$$\mathbf{f}_{\text{ext}}^{(k+1)}(\mathbf{r}, t) = \mathbf{f}_{\text{ext}}^{(k)}(\mathbf{r}, t) + \frac{m}{\rho(\mathbf{r}, t)} (\dot{\mathbf{J}}(\mathbf{r}, t) - \dot{\mathbf{J}}^{(k)}(\mathbf{r}, t)) - \nabla \cdot \boldsymbol{\tau}^{(k)}(\mathbf{r}, t) \left(\frac{1}{\rho(\mathbf{r}, t)} - \frac{1}{\rho^{(k)}(\mathbf{r}, t)} \right), \quad (\text{A4})$$

where we have assumed that target and sampled density profiles are the same, i.e., set $\rho^{(k)}(\mathbf{r}, t) \rightarrow \rho(\mathbf{r}, t)$ in the first term of the right-hand side of Eq. (A3). Note that this is necessarily the case if the iterative process converges. Comparing Eqs. (A4) and (10) yields $\beta = \frac{m}{\rho}$.

To find an expression for α , we approximate $\dot{\mathbf{J}}(\mathbf{r}, t)$ and $\dot{\mathbf{J}}^{(k)}(\mathbf{r}, t)$ in Eq. (A4) by

$$\dot{\mathbf{J}}(\mathbf{r}, t) = \frac{\mathbf{J}(\mathbf{r}, t) - \mathbf{J}(\mathbf{r}, t - \Delta t)}{\Delta t}, \quad (\text{A5})$$

$$\dot{\mathbf{J}}^{(k)}(\mathbf{r}, t) = \frac{\mathbf{J}^{(k)}(\mathbf{r}, t) - \mathbf{J}(\mathbf{r}, t - \Delta t)}{\Delta t}, \quad (\text{A6})$$

where we have used that the sampled $\mathbf{J}^{(k)}$ and the target \mathbf{J} coincide at time $t - \Delta t$. This is again necessarily the case if the process converges. Although a central time difference would be more precise, we use here the backward time difference since $\mathbf{J}^{(k)}(\mathbf{r}, t + \Delta t)$ is unknown at time t . Inserting Eqs. (A5) and (A6) into Eq. (A4) and comparing the result with Eq. (10) result in $\alpha = \frac{m}{\rho \Delta t}$.

Finally, to find a suitable expression for γ , we use the equilibrium expression for the transport term (19) to roughly approximate the second term in Eq. (A4) by

$$-\nabla \cdot \boldsymbol{\tau}^{(k)} \left(\frac{1}{\rho} - \frac{1}{\rho^{(k)}} \right) \sim +k_B T \nabla \ln \frac{\rho}{\rho^{(k)}}, \quad (\text{A7})$$

from which we obtain $\gamma = k_B T$ by comparison with Eq. (10). We note that Eq. (A7) is a crude approximation, but we are only interested in a suitable expression for the prefactor γ . The precise value of the prefactors is not critical for the method to converge (provided they are small enough such that the iterative process is stable). However, having suitable expressions is relevant to achieve a fast convergence since the prefactors control the amount of change in the external force from iteration to iteration.

-
- [1] D. J. Evans and O. P. Morriss, Non-Newtonian molecular dynamics, *Comput. Phys. Rep.* **1**, 297 (1984).
- [2] B. Hess, Determining the shear viscosity of model liquids from molecular dynamics simulations, *J. Chem. Phys.* **116**, 209 (2002).
- [3] F. Müller-Plathe, Reversing the perturbation in nonequilibrium molecular dynamics: An easy way to calculate the shear viscosity of fluids, *Phys. Rev. E* **59**, 4894 (1999).
- [4] W. G. Hoover, A. J. C. Ladd, R. B. Hickman, and B. L. Holian, Bulk viscosity via nonequilibrium and equilibrium molecular dynamics, *Phys. Rev. A* **21**, 1756 (1980).
- [5] G. Jung and F. Schmid, Computing bulk and shear viscosities from simulations of fluids with dissipative and stochastic interactions, *J. Chem. Phys.* **144**, 204104 (2016).
- [6] F. Müller-Plathe, A simple nonequilibrium molecular dynamics method for calculating the thermal conductivity, *J. Chem. Phys.* **106**, 6082 (1997).
- [7] H.A. Stone, A. D. Stroock, and A. Ajdari, Engineering flows in small devices: Microfluidics toward a lab-on-a-chip, *Annu. Rev. Fluid Mech.* **36**, 381 (2004).
- [8] T. M. Squires and S. R. Quake, Microfluidics: Fluid physics at the nanoliter scale, *Rev. Mod. Phys.* **77**, 977 (2005).
- [9] F. Zhu, E. Tajkhorshid, and K. Schulten, Pressure-induced water transport in membrane channels studied by molecular dynamics, *Biophys. J.* **83**, 154 (2002).
- [10] F. D. Sofos, T. E. Karakasidis, and A. Liakopoulos, Effects of wall roughness on flow in nanochannels, *Phys. Rev. E* **79**, 026305 (2009).
- [11] R. Hartkamp, A. Ghosh, T. Weinhart, and S. Luding, A study of the anisotropy of stress in a fluid confined in a nanochannel, *J. Chem. Phys.* **137**, 044711 (2012).
- [12] T. Glad and L. Ljung, *Control Theory*, 1st ed. (CRC, Boca Raton, 2000).
- [13] M. Mirzaee-Kakhki, A. Ernst, D. de las Heras, M. Urbaniak, F. Stobiecki, J. Gördes, M. Reginka, A. Ehresmann, and T. M. Fischer, Simultaneous polydirectional transport of colloidal bipeds, *Nat. Commun.* **11**, 4670 (2020).
- [14] J. Loehr, M. Loenne, A. Ernst, D. de las Heras, and T. M. Fischer, Topological protection of multiparticle dissipative transport, *Nat. Commun.* **7**, 11745 (2016).
- [15] D. de las Heras and M. Schmidt, Flow and Structure in Nonequilibrium Brownian Many-Body Systems, *Phys. Rev. Lett.* **125**, 018001 (2020).
- [16] G. I. Toth, Exact hydrodynamic equations to the classical many-body problem in the macroscopic limit, [arXiv:2009.03089](https://arxiv.org/abs/2009.03089) [cond-mat.stat-mech].
- [17] Wm. G. Hoover and C. G. Hoover, Time-symmetry breaking in Hamiltonian mechanics. II. A memoir for Berni Julian Alder [1925–2020], *Comput. Methods Sci. Technol.* **26**, 101 (2020).


- [18] D. J. Evans, W. G. Hoover, B. H. Failor, B. Moran, and A. J. C. Ladd, Nonequilibrium molecular dynamics via Gauss's principle of least constraint, *Phys. Rev. A* **28**, 1016 (1983).
- [19] S. Granick, Motions and relaxations of confined liquids, *Science* **253**, 1374 (1991).
- [20] H.-W. Hu, G. A. Carson, and S. Granick, Relaxation Time of Confined Liquids under Shear, *Phys. Rev. Lett.* **66**, 2758 (1991).
- [21] I. Bitsanis, S. A. Somers, H. T. Davis, and M. Tirrell, Microscopic dynamics of flow in molecularly narrow pores, *J. Chem. Phys.* **93**, 3427 (1990).
- [22] L. A. Pozhar, Structure and dynamics of nanofluids: Theory and simulations to calculate viscosity, *Phys. Rev. E* **61**, 1432 (2000).
- [23] K. P. Travis and K. E. Gubbins, Poiseuille flow of Lennard-Jones fluids in narrow slit pores, *J. Chem. Phys.* **112**, 1984 (2000).
- [24] D. Lesnicki, R. Vuilleumier, A. Carof, and B. Rotenberg, Molecular Hydrodynamics from Memory Kernels, *Phys. Rev. Lett.* **116**, 147804 (2016).
- [25] G. Jung, M. Hanke, and F. Schmid, Iterative reconstruction of memory kernels, *J. Chem. Theory Comput.* **13**, 2481 (2017).
- [26] O. A. Hickey, J. L. Harden, and G. W. Slater, Molecular Dynamics Simulations of Optimal Dynamic Uncharged Polymer Coatings for Quenching Electro-Osmotic Flow, *Phys. Rev. Lett.* **102**, 108304 (2009).
- [27] Y. Li, J. Xu, and D. Li, Molecular dynamics simulation of nanoscale liquid flows, *Microfluid. Nanofluid.* **9**, 1011 (2010).
- [28] S. Kumar Kannam, B. D. Todd, J. S. Hansen, and P. J. Daivis, Slip length of water on graphene: Limitations of non-equilibrium molecular dynamics simulations, *J. Chem. Phys.* **136**, 024705 (2012).
- [29] P. Hohenberg and W. Kohn, Inhomogeneous electron gas, *Phys. Rev. [Sect.] B* **136**, B864 (1964).
- [30] N. D. Mermin, Thermal properties of the inhomogeneous electron gas, *Phys. Rev. [Sect.] A* **137**, A1441 (1965).
- [31] R. Evans, The nature of the liquid-vapour interface and other topics in the statistical mechanics of non-uniform, classical fluids, *Adv. Phys.* **28**, 143 (1979).
- [32] E. Runge and E. K. U. Gross, Density-Functional Theory for Time-Dependent Systems, *Phys. Rev. Lett.* **52**, 997 (1984).
- [33] G. K.-L. Chan and R. Finken, Time-Dependent Density Functional Theory of Classical Fluids, *Phys. Rev. Lett.* **94**, 183001 (2005).
- [34] M. Schmidt and J. M. Brader, Power functional theory for Brownian dynamics, *J. Chem. Phys.* **138**, 214101 (2013).
- [35] M. Schmidt, Power functional theory for Newtonian many-body dynamics, *J. Chem. Phys.* **148**, 044502 (2018).
- [36] M. Schmidt, Quantum power functional theory for many-body dynamics, *J. Chem. Phys.* **143**, 174108 (2015).
- [37] A. Fortini, D. de las Heras, J. M. Brader, and M. Schmidt, Superadiabatic Forces in Brownian Many-Body Dynamics, *Phys. Rev. Lett.* **113**, 167801 (2014).
- [38] D. de las Heras, J. Renner, and M. Schmidt, Custom flow in overdamped Brownian dynamics, *Phys. Rev. E* **99**, 023306 (2019).
- [39] M. Thiele, E. K. U. Gross, and S. Kümmel, Adiabatic Approximation in Nonperturbative Time-Dependent Density-Functional Theory, *Phys. Rev. Lett.* **100**, 153004 (2008).
- [40] M. Brütting, T. Trepl, D. de las Heras, and M. Schmidt, Superadiabatic forces via the acceleration gradient in quantum many-body dynamics, *Molecules* **24**, 3660 (2019).
- [41] D. de las Heras and M. Schmidt, Better than Counting: Density Profiles from Force Sampling, *Phys. Rev. Lett.* **120**, 218001 (2018).
- [42] D. Borgis, R. Assaraf, B. Rotenberg, and R. Vuilleumier, Computation of pair distribution functions and three-dimensional densities with a reduced variance principle, *Mol. Phys.* **111**, 3486 (2013).
- [43] S. W. Coles, D. Borgis, R. Vuilleumier, and B. Rotenberg, Computing three-dimensional densities from force densities improves statistical efficiency, *J. Chem. Phys.* **151**, 064124 (2019).
- [44] A. Purohit, A. J. Schultz, and D. A. Kofke, Force-sampling methods for density distributions as instances of mapped averaging, *Mol. Phys.* **117**, 2822 (2019).
- [45] B. Rotenberg, Use the force! Reduced variance estimators for densities, radial distribution functions, and local mobilities in molecular simulations, *J. Chem. Phys.* **153**, 150902 (2020).
- [46] G. Bussi, D. Donadio, and M. Parrinello, Canonical sampling through velocity rescaling, *J. Chem. Phys.* **126**, 014101 (2007).
- [47] J. D. Weeks, D. Chandler, and H. C. Andersen, Role of repulsive forces in determining the equilibrium structure of simple liquids, *J. Chem. Phys.* **54**, 5237 (1971).
- [48] W. C. Swope, H. C. Andersen, P. H. Berens, and K. R. Wilson, A computer simulation method for the calculation of equilibrium constants for the formation of physical clusters of molecules: Application to small water clusters, *J. Chem. Phys.* **76**, 637 (1982).
- [49] See Supplemental Material at <http://link.aps.org/supplemental/10.1103/PhysRevResearch.3.013281> for movies of the dynamical time evolution of the one-body fields.
- [50] We calculate the temperature in equilibrium via the equipartition theorem $E_{\text{kin}} = \frac{3}{2}(N-1)k_B T$, where E_{kin} is the total kinetic energy of the system $E_{\text{kin}} = \frac{m}{2} \sum_{i=1}^N \mathbf{v}_i^2$.
- [51] P. H. Hünenberger, Thermostat algorithms for molecular dynamics simulations, in *Advanced Computer Simulation: Approaches for Soft Matter Sciences I* (Springer, Berlin, 2005), pp. 105–149.
- [52] H. J. C. Berendsen, J. P. M. Postma, W. F. van Gunsteren, A. DiNola, and J. R. Haak, Molecular dynamics with coupling to an external bath, *J. Chem. Phys.* **81**, 3684 (1984).
- [53] W. Loose and G. Ciccotti, Temperature and temperature control in nonequilibrium-molecular-dynamics simulations of the shear flow of dense liquids, *Phys. Rev. A* **45**, 3859 (1992).
- [54] H. Meyer, P. Pelagejcev, and T. Schilling, Non-Markovian out-of-equilibrium dynamics: A general numerical procedure to construct time-dependent memory kernels for coarse-grained observables, *EPL* **128**, 40001 (2020).
- [55] J. Berner, B. Müller, J. R. Gomez-Solano, M. Krüger, and C. Bechinger, Oscillating modes of driven colloids in overdamped systems, *Nat. Commun.* **9**, 999 (2018).
- [56] L. L. Treffenstädt and M. Schmidt, Memory-induced motion reversal in Brownian liquids, *Soft Matter* **16**, 1518 (2020).
- [57] J. Wong-Ekkabut, M. S. Miettinen, C. Dias, and M. Karttunen, Static charges cannot drive a continuous flow of water molecules through a carbon nanotube, *Nat. Nanotechnol.* **5**, 555 (2010).

- [58] M. Thomas and B. Corry, Thermostat choice significantly influences water flow rates in molecular dynamics studies of carbon nanotubes, *Microfluid. Nanofluid.* **18**, 41 (2015).
- [59] J. Casas-Vázquez and D. Jou, Nonequilibrium temperature versus local-equilibrium temperature, *Phys. Rev. E* **49**, 1040 (1994).
- [60] D. Levesque and L. Verlet, Molecular dynamics and time reversibility, *J. Stat. Phys.* **72**, 519 (1993).
- [61] U. M. B. Marconi and P. Tarazona, Dynamic density functional theory of fluids, *J. Chem. Phys.* **110**, 8032 (1999).
- [62] N. C. X. Stuhlmüller, T. Eckert, D. de las Heras, and M. Schmidt, Structural Nonequilibrium Forces in Driven Colloidal Systems, *Phys. Rev. Lett.* **121**, 098002 (2018).
- [63] S. Hermann, P. Krinninger, D. de las Heras, and M. Schmidt, Phase coexistence of active Brownian particles, *Phys. Rev. E* **100**, 052604 (2019).
- [64] T. Geigenfeind, D. de las Heras, and M. Schmidt, Superadiabatic demixing in nonequilibrium colloids, *Commun. Phys.* **3**, 23 (2020).
- [65] R. Delgado-Buscalioni and P. V. Coveney, Continuum-particle hybrid coupling for mass, momentum, and energy transfers in unsteady fluid flow, *Phys. Rev. E* **67**, 046704 (2003).
- [66] M. Praprotnik, L. Delle Site, and K. Kremer, Adaptive resolution molecular-dynamics simulation: Changing the degrees of freedom on the fly, *J. Chem. Phys.* **123**, 224106 (2005).
- [67] R. Potestio, S. Fritsch, P. Español, R. Delgado-Buscalioni, K. Kremer, R. Everaers, and D. Donadio, Hamiltonian Adaptive Resolution Simulation for Molecular Liquids, *Phys. Rev. Lett.* **110**, 108301 (2013).
- [68] C. Krekeler, A. Agarwal, C. Junghans, M. Praprotnik, and L. Delle Site, Adaptive resolution molecular dynamics technique: Down to the essential, *J. Chem. Phys.* **149**, 024104 (2018).

Shear and Bulk Acceleration Viscosities in Simple Fluids

Johannes Renner¹, Matthias Schmidt¹, and Daniel de las Heras^{1*}

Theoretische Physik II, Physikalisches Institut, Universität Bayreuth, D-95440 Bayreuth, Germany

 (Received 30 October 2021; accepted 9 February 2022; published 4 March 2022)

Inhomogeneities in the velocity field of a moving fluid are dampened by the inherent viscous behavior of the system. Both bulk and shear effects, related to the divergence and the curl of the velocity field, are relevant. On molecular time scales, beyond the Navier-Stokes description, memory plays an important role. Using molecular and overdamped Brownian dynamics many-body simulations, we demonstrate that analogous viscous effects act on the acceleration field. This acceleration viscous behavior is associated with the divergence and the curl of the acceleration field, and it can be quantitatively described using simple exponentially decaying memory kernels. The simultaneous use of velocity and acceleration fields enables the description of fast dynamics on molecular scales.

DOI: 10.1103/PhysRevLett.128.094502

The viscous force determines the resistance of a moving fluid to change the magnitude and the direction of the flow. Such a viscous response, originated by the interparticle interactions, is relevant in, e.g., lubrication [1], protein dynamics in biological solvents [2,3], viscotaxis [4,5], magnetic [6] and quantum [7] fluids, lava flows [8], cardiovascular events [9,10], food manufacturing [11], and cosmological models [12,13]. Viscous effects are associated with inhomogeneities in the velocity field of the fluid. The viscous force $\mathbf{f}_{\text{vis}}(\mathbf{r}, t)$ experienced by a particle of a fluid at position \mathbf{r} and time t contains bulk $\mathbf{f}_b(\mathbf{r}, t)$ and shear $\mathbf{f}_s(\mathbf{r}, t)$ contributions, i.e., $\mathbf{f}_{\text{vis}} = \mathbf{f}_b + \mathbf{f}_s$. These contributions are associated with the divergence $\nabla \cdot \mathbf{v}$ (bulk) and the curl $\nabla \times \mathbf{v}$ (shear) of the velocity field $\mathbf{v}(\mathbf{r}, t)$, respectively. Specifically, \mathbf{f}_{vis} in the Navier-Stokes [14] equations is

$$\rho \mathbf{f}_{\text{vis}} = \eta_b \nabla \nabla \cdot \mathbf{v} - \eta_s \nabla \times (\nabla \times \mathbf{v}), \quad (1)$$

where $\rho(\mathbf{r}, t)$ is the density profile and η_α with $\alpha = b, s$ are transport coefficients known as bulk and shear viscosities.

Here, we demonstrate the occurrence in simple fluids of analog viscous contributions, but generated by the divergence and the curl of the acceleration field $\mathbf{a}(\mathbf{r}, t)$. We use custom flow [15,16] to design specific flows (driven by external forces) in which we can unambiguously single out the acceleration contribution of the viscous force. We consider inhomogeneous and rapidly changing flows. Hence, memory effects and inhomogeneities of the density profile cannot be ignored and need to be included in Eq. (1). We propose the following expressions for bulk and shear viscous forces of an inhomogeneous simple fluid,

$$\mathbf{f}_b(\mathbf{r}, t) = \frac{1}{\rho} \int_0^t dt' [K_b^\gamma(t-t') \nabla(\rho \rho' \nabla \cdot \mathbf{v}') + K_b^a(t-t') \nabla(\rho \rho' \nabla \cdot \mathbf{a}')], \quad (2)$$

$$\mathbf{f}_s(\mathbf{r}, t) = \frac{-1}{\rho} \int_0^t dt' [K_s^\gamma(t-t') \nabla \times (\rho \rho' \nabla \times \mathbf{v}') + K_s^a(t-t') \nabla \times (\rho \rho' \nabla \times \mathbf{a}')], \quad (3)$$

where we leave out the dependence on \mathbf{r} and t , primed quantities are evaluated at t' , e.g., $\rho' = \rho(\mathbf{r}, t')$, and K_α^Γ (with $\alpha = b, s$ and $\Gamma = \mathbf{v}, \mathbf{a}$) are exponentially decaying memory kernels

$$K_\alpha^\Gamma(t-t') = \frac{c_\alpha^\Gamma}{\tau_\alpha^\Gamma} e^{-(t-t')/\tau_\alpha^\Gamma}, \quad (4)$$

with constant amplitudes c_α^Γ and memory times τ_α^Γ . The first terms of Eqs. (2) and (3) are the familiar bulk and shear viscous forces in the Navier-Stokes equations, Eq. (1), for flows with inhomogeneous density profiles and with the addition of a memory kernel. The second terms have identical structure but replacing \mathbf{v} by \mathbf{a} and represent therefore a viscous response generated by an inhomogeneous acceleration field. The viscous force in Eq. (1) with viscosities $\eta_\alpha = c_\alpha^\gamma \rho^2$ follows from the velocity contributions of Eqs. (2) and (3) by ignoring the effect of both memory and an inhomogeneous density profile. Our specific form for \mathbf{f}_{vis} arises in power functional theory [17–19] by retrieving the first terms of an expansion in acceleration gradients; see additional details in the Supplemental Material [20].

To demonstrate the occurrence of viscous effects associated with the acceleration field, we need to disentangle the velocity and the acceleration contributions from the total viscous force. This requires a complete control over the characteristics of the flow, which we achieve using custom flow [15,16]. Custom flow uses particle-based simulations to find numerically the spatially and temporally resolved external field required to generate the desired

dynamics of a many-body system. The one-body density $\rho(\mathbf{r}, t)$ and current $\mathbf{J}(\mathbf{r}, t) = \rho(\mathbf{r}, t)\mathbf{v}(\mathbf{r}, t)$ profiles serve as input target fields, while the external field $\mathbf{f}_{\text{ext}}(\mathbf{r}, t)$ that generates these targets is the output of the method. At each time, $\mathbf{f}_{\text{ext}}(\mathbf{r}, t)$ is constructed iteratively. At iteration $k + 1$ we add to the external force of the previous iteration k a term proportional to the difference between the target (\mathbf{J}) and sampled ($\mathbf{J}^{(k)}$) currents, i.e., $\mathbf{f}_{\text{ext}}^{(k+1)} = \mathbf{f}_{\text{ext}}^{(k)} + \alpha_0(\mathbf{J} - \mathbf{J}^{(k)})$. Here, the parameter $\alpha_0(\mathbf{r}, t) > 0$ is chosen to ensure that the difference between the target and sampled current fields progressively shrinks. Details about custom flow are provided in Refs. [15,16] and in the Supplemental Material [20]. Custom flow is essential here to tailor the dynamics of the system such that the viscous force can be (i) easily measured and (ii) unambiguously split into velocity and acceleration contributions. We use molecular dynamics (MD) simulations to study a three-dimensional system of particles of mass m interacting via the short-ranged and purely repulsive Weeks-Chandler-Andersen pair potential [21] with length and energy parameters σ

and ϵ , respectively. We work in units of σ , ϵ , and m . Hence, the unit of time is $\tau = \sqrt{m\sigma^2/\epsilon}$. We consider two different flows that represent pure bulk (compressible) and shear situations. In both flows the one-body current \mathbf{J} factorizes into a (vectorial) spatial part \mathbf{J}_r and a (scalar) temporal part J_t , i.e., $\mathbf{J}(\mathbf{r}, t) = J_t(t)\mathbf{J}_r(\mathbf{r})$.

The temporal part is common to both flows; see Fig. 1(a) and the Supplemental Material [20] for the mathematical expression. The current increases from the initial time until $t_\uparrow = 1\tau$, then remains constant (quasisteady state) until $t_c = 5\tau$, decreases until it vanishes at $t_\downarrow = 6\tau$, and it stays zero afterward. This setup helps to disentangle the velocity and the acceleration contributions from \mathbf{f}_{vis} since \mathbf{v} and \mathbf{a} are parallel to each other during the increase of \mathbf{J} , but they are antiparallel during the decrease of \mathbf{J} . Both \mathbf{v} and \mathbf{a} stay unchanged during the quasisteady state and during the final evolution toward equilibrium which is useful to characterize memory effects.

Both flows are designed to have a stationary one-body density during the whole time evolution, i.e., $\dot{\rho}(\mathbf{r}, t) = 0$,

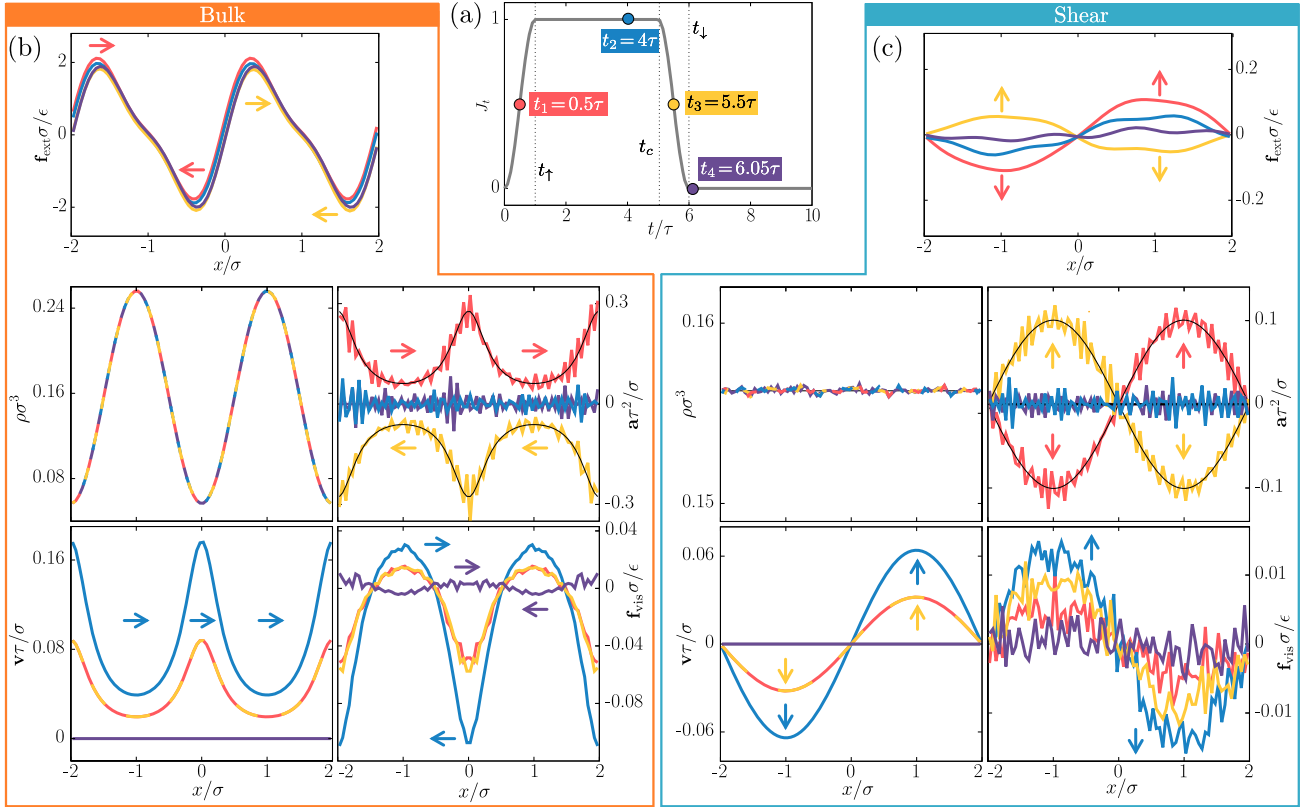


FIG. 1. (a) Temporal part of the current J_t vs time t common to the bulk (b) and shear (c) flows. Four times t_i with $i = 1, 2, 3$, and 4 are highlighted with colored circles. The vertical dotted lines indicate the times t_\uparrow , t_c , and t_\downarrow . (b),(c) The external force \mathbf{f}_{ext} , density ρ , velocity \mathbf{v} , acceleration \mathbf{a} , and viscous force \mathbf{f}_{vis} profiles as a function of x for the bulk and shear flows, respectively. To improve the visualization, the external force has been smoothed by eliminating high-frequency Fourier modes (see details and raw data in the Supplemental Material [20]). The thin black solid lines are the target fields that coincide (up to numerical accuracy) with the sampled fields. The color of the profiles indicates the time $t_1 = 0.5\tau$ (red), $t_2 = 4\tau$ (blue), $t_3 = 5.5\tau$ (yellow), and $t_4 = 6.05\tau$ (purple), as indicated in (a). The arrows indicate the direction of the vector field at specific locations (arrow position) and times (arrow color).

where the overdot denotes a time derivative. This simplifies the data analysis since as a direct consequence the viscous forces in Eqs. (2) and (3) also factorize into spatial and temporal terms [20]

$$\mathbf{f}_\alpha(\mathbf{r}, t) = C_\alpha(t)\mathbf{f}_{\mathbf{r},\alpha}(\mathbf{r}), \quad \alpha = b, s. \quad (5)$$

Bulk flow.—Here, by construction $\nabla \times \mathbf{v} = 0$ and $\nabla \times \mathbf{a} = 0$ but $\nabla \cdot \mathbf{v} \neq 0$ and $\nabla \cdot \mathbf{a} \neq 0$. Hence, only bulk effects contribute to the viscous force, i.e., $\mathbf{f}_{\text{vis}} = \mathbf{f}_b$. We take the one-body density to be inhomogeneous, but only along the x direction. The one-body current has only an x component which is taken to be constant in space:

$$\rho(\mathbf{r}, t) = \rho(x) = \rho_0 - \rho_1 \cos(4\pi x/L_x), \quad (6)$$

$$\mathbf{J}(\mathbf{r}, t) = \mathbf{J}(t) = J_0 J_t(t) \hat{\mathbf{e}}_x, \quad (7)$$

with average density $\rho_0\sigma^3 = 0.15625$, amplitude $\rho_1\sigma^3 = 0.1$, side length of the simulation box $L_x/\sigma = 4$, and maximum value of the current $J_0\tau\sigma^2 = 0.01$. Both the velocity $\mathbf{v} = \mathbf{J}/\rho$ and the acceleration $\mathbf{a} = \dot{\mathbf{v}} = \dot{\mathbf{J}}/\rho$ (where the second equality holds here since $\dot{\rho} = 0$) are inhomogeneous in space even though the current is homogeneous.

The external force that produces this bulk flow together with density, velocity, and acceleration profiles sampled in MD are shown in Fig. 1(b) for four selected times. The viscous force \mathbf{f}_{vis} [also shown in Fig. 1(b)] is the part of the internal force that changes sign under flow reversal [20,22]. The four times selected in Fig. 1 represent the different regimes of the time evolution imposed by J_t ; see Fig. 1(a). At $t_1 = 0.5\tau$, i.e., $t_1 < t_\uparrow$, the current increases, and both \mathbf{v} and \mathbf{a} point in the same direction. At $t_2 = 4\tau$, i.e., $t_\uparrow < t_2 < t_c$, the system is in a quasisteady state with negligible memory effects (we know this by monitoring the viscous force which does not change with time). The acceleration vanishes everywhere, and the velocity profile remains unchanged in this time interval. At $t_3 = 5.5\tau$, i.e., $t_c < t_3 < t_\downarrow$ the current decreases. The velocity and the acceleration profiles have opposite sign everywhere. Finally, at $t_4 = 6.05\tau$, i.e., $t_4 > t_\downarrow$, both \mathbf{v} and \mathbf{a} vanish everywhere. However, due to memory effects the system has not reached equilibrium yet; there is, for example, a viscous force generated by the history of \mathbf{v} and \mathbf{a} .

A visual inspection of the viscous force \mathbf{f}_{vis} , in Fig. 1(b), reveals two strong indications that the acceleration profile contributes to the viscosity. First, at t_4 the viscous force points in the opposite direction than at the previous times. Hence, the history of the acceleration profile must be dominating the viscosity since the velocity profile does not change its sign during the whole time evolution. Only \mathbf{a} changes sign during the decrease of the current [compare the acceleration profiles at times t_1 and t_3 in Fig. 1(b)]. Second, the profiles \mathbf{f}_{vis} at times t_1 and t_3 are similar. At these two times the velocity profiles are identical by

construction; see Figs. 1(a) and 1(b). However, \mathbf{a} and the history of both \mathbf{v} and \mathbf{a} are different. Since the viscosity at a given time depends on the history of the system, the contribution to the viscosity due to the acceleration must be canceling the contribution due to the history of the velocity profile. Otherwise, the viscous force at these times would differ.

The temporal part $C_b(t)$ for the bulk flow [see Eq. (5)] can be understood as the variation of the strength of the viscous force over time. Results are shown in Fig. 2(a). Clearly, C_b achieves larger values than at the quasisteady state for times around t_\uparrow , and smaller (negative) values than in equilibrium ($C_b = 0$) for times around t_\downarrow . The acceleration is responsible for the overshoot and the undershoot around the times t_\uparrow and t_\downarrow because \mathbf{a} is the only field that flips its sign during the increase and during the decrease of the current. Note that if \mathbf{a} does not contribute to the bulk viscous force, then the negative values of C_b would indicate an unphysical negative viscosity.

We next compare the MD data to our expression for the viscous force \mathbf{f}_b , Eq. (2), to obtain the kernel parameters; see the Supplemental Material [20] for details.

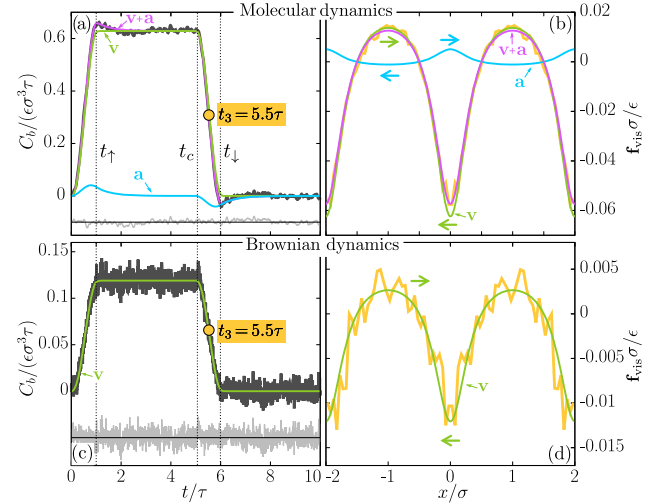


FIG. 2. (a) Temporal dependency of the bulk viscous force C_b as a function of time t in molecular dynamics simulations (thick black line) and theoretically (violet) for the bulk flow. The vertical dotted lines indicate the times t_\uparrow , t_c , and t_\downarrow . The time $t_3 = 5.5\tau$ is highlighted with a yellow circle. The light gray line fluctuating around the horizontal line is the difference between simulation (thick black) and theory (violet). (b) Bulk viscous force \mathbf{f}_{vis} as a function of x at time $t_3 = 5.5\tau$ according to MD (yellow) and theory (violet). The force points along the x axis. The colored arrows indicate the direction of the corresponding force at selected positions. The contributions of the velocity (green) and of the acceleration (blue) to the total signal (violet) are also shown in (a) and (b). The bottom panels (c) and (d) show the same data as the top panels, but using overdamped Brownian dynamics instead of MD. In BD only the velocity field contributes to the viscosity.

The amplitudes are $c_b^y/(\epsilon\sigma^3\tau) = 0.63$, $c_b^a/(\epsilon\sigma^3\tau^2) = 0.044$, and the memory times are $\tau_b^y/\tau = 0.043$, $\tau_b^a/\tau = 0.56$. The partial contributions of the velocity and the acceleration fields to C_b and \mathbf{f}_{vis} are shown in Figs. 2(a) and 2(b), respectively. The sum of both contributions agrees quantitatively with the MD data.

To assure that the overshoot and the undershoot in C_b are indeed due to the acceleration field, we performed overdamped Brownian dynamics (BD) simulations for exactly the same flow (using BD custom flow [15,20] and the usual assumption that the random force does not depend on the external force [23]). Since the system is overdamped, the acceleration does not play any role, and indeed, there is no overshoot or undershoot in C_b [Fig. 2(c)]. Both C_b and \mathbf{f}_{vis} are well reproduced theoretically using only the velocity field, Figs. 2(c) and 2(d), with kernel parameters $c_b^y/(\epsilon\sigma^3\tau) = 0.117$ and $\tau_b^y/\tau = 0.041$.

Shear flow.—We next consider a flow in which $\nabla \cdot \mathbf{v} = 0$ and $\nabla \cdot \mathbf{a} = 0$ but $\nabla \times \mathbf{v} \neq 0$ and $\nabla \times \mathbf{a} \neq 0$. Hence, only shear effects contribute to the viscous force, i.e., $\mathbf{f}_{\text{vis}} = \mathbf{f}_s$. Using custom flow we set the density profile to be homogeneous and the current to be a shear wave pointing in the y direction with modulation along the x direction,

$$\rho(\mathbf{r}, t) = \rho_0, \quad (8)$$

$$\mathbf{J}(\mathbf{r}, t) = \mathbf{J}(x, t) = J_0 \sin(2\pi x/L_x) J_t(t) \hat{\mathbf{e}}_y, \quad (9)$$

with $\rho_0\sigma^3 = 0.15625$, $L_x/\sigma = 4$, and $J_0\tau\sigma^2 = 0.01$.

Figure 1(c) shows the external force required to produce the flow along with results for ρ , \mathbf{v} , \mathbf{a} , and \mathbf{f}_{vis} at the same four different times as in the previous flow. A visual inspection of the data does not reveal the acceleration contribution since (i) for times $t_1 = 0.5\tau$ and $t_3 = 5.5\tau$ the curves are different (suggesting either a large memory time of the velocity contribution or a strong effect of the acceleration) and (ii) \mathbf{f}_{vis} does not flip the sign after the one-body current vanishes. Also, in contrast to the bulk flow, no apparent over- or undershoot is present in $C_s(t)$, i.e., the temporal part of \mathbf{f}_{vis} [see Fig. 3(a) and Eq. (5)]. For the shear flow we find that the amplitudes $c_s^y/(\epsilon\sigma^3\tau) = 0.56$ and $c_s^a/(\epsilon\sigma^3\tau^2) = 0.059$, and the memory times $\tau_s^y = 0.24\tau$, $\tau_s^a = 0.23\tau$ yield quantitative agreement between simulation data and our theory for both the temporal, Fig. 3(a), and the spatial dependence of \mathbf{f}_{vis} , Fig. 3(b). In contrast to the bulk flow, the memory times of \mathbf{a} and \mathbf{v} are now comparable, which partially hides the effect of the acceleration. To demonstrate the importance of \mathbf{a} we use only the velocity contribution and obtain $c_s^y/(\epsilon\sigma^3\tau) = 0.56$ and $\tau_s^y/\tau = 0.13$ as the optimal kernel parameters. The resulting curve for C_s [see Fig. 3(a)] deviates from the MD data around the times t_\uparrow (curve above MD data) and t_\downarrow (curve below MD data). This indicates that \mathbf{a} indeed contributes since its sign change around these times can correct these deviations.

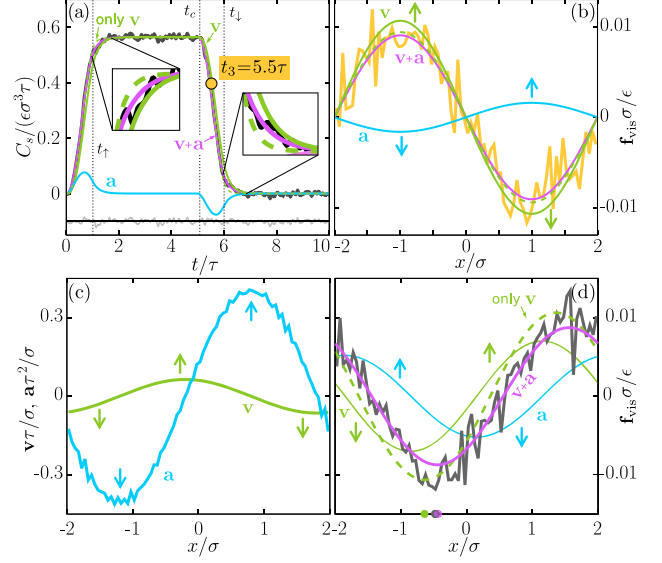


FIG. 3. (a) Temporal dependency of the shear viscous force C_s as a function of time t in MD simulations (thick black line) and theoretically (violet) for the shear flow. The light gray line fluctuating around the horizontal line is the difference between simulation (thick black) and theory (violet). (b) Shear viscous force \mathbf{f}_{vis} as a function of x at time $t_3 = 5.5\tau$ according to MD (yellow) and theory (violet). The force points along the y axis. (c) Illustrative velocity (green) and acceleration (blue) profiles vs x for the traveling shear wave ($t = 2.7\tau$). Note that \mathbf{a} and \mathbf{v} are not in phase. (d) Viscous force vs x for the traveling shear wave according to MD (thick black) and theory (violet) ($t = 2.7\tau$). The colored arrows indicate the direction of the corresponding field at the selected positions. The theoretical contributions of \mathbf{v} (green) and \mathbf{a} (blue) to the total signal (violet) are also shown in panels (a), (b), and (d) together with the theoretical predictions using only the velocity field (dashed green line). The colored circles over the x axis in (d) indicate the position of the minimum of \mathbf{f}_{vis} according to MD (gray), and theory using both contributions (violet) or only the velocity contribution (green).

To further ascertain the reality of the acceleration contribution, we use the obtained parameters for the amplitudes and the memory times to describe a variation of the flow. Instead of decreasing the one-body current after t_c , we keep the amplitude of the current unchanged and let the shear wave travel in the positive x direction. Specifically, after time $t = 2\tau > t_\uparrow$ we replace the x coordinate in Eq. (9) by $x - v_s t$ with constant velocity $v_s = 4\tau/\sigma$. Hence, the acceleration field is shifted by $\pi/2$ with respect to the velocity field; see Fig. 3(c). The phase difference between \mathbf{v} and \mathbf{a} has an effect on the viscous force; see Fig. 3(d). Using the kernel parameters for the previous flow and both the velocity and the acceleration contributions we reproduce the simulation data. In contrast, using the parameters obtained only with the velocity contribution results in a clear phase shift compared with the MD data. See the Supplemental Material [20] for more details.

Our results demonstrate the existence of shear and bulk acceleration viscous forces generated by inhomogeneities of the acceleration field. These forces act in addition to the usual viscous response associated with the velocity field. In our examples the contribution of the acceleration to the viscous force is quantitatively significant. Acceleration viscous forces might be also relevant in flows with rapid temporal changes of the velocity field such as in shock waves [24–28], turbulent flows [29–31] including atmospheric and oceanic flows [32], inertial microfluidics [33–35], the description of flows at the nanoscale [36–38], mudflows [39], single-bubble sonoluminescence [40,41], and viscous cosmological models [12,42].

We did not use a thermostat due to the low heat production in both flows (the temperature increase was less than 2% from the initial to the final state [20]). However, custom flow can be used with thermostats [16], and it would be interesting to compare the effect of the acceleration viscosities in thermalized and nonthermalized flows.

We use here a rather simple kernel as compared with other approaches [43–46]. The use of simple memory kernels that decay exponentially in time is only possible because we use all physically relevant variables, i.e., both \mathbf{v} and \mathbf{a} . Since \mathbf{a} and \mathbf{v} are related to each other, it should be possible to describe \mathbf{f}_{vis} using only \mathbf{v} or \mathbf{a} together with a complicated kernel. Such a kernel would be tailored to the specific flow instead of being general to every situation. For example, it might be possible to describe the viscous force of the bulk flow using only \mathbf{v} and a complex memory kernel with a negative tail.

This work is supported by the German Research Foundation (DFG) via Project No. 447925252.

*Corresponding author.

<https://www.danieldelasheras.com>
delasheras.daniel@gmail.com

- [1] B. Bhushan, J. N. Israelachvili, and U. Landman, Nanotribology: Friction, wear and lubrication at the atomic scale, *Nature (London)* **374**, 607 (1995).
- [2] A. Ansari, C. M. Jones, E. R. Henry, J. Hofrichter, and W. A. Eaton, The role of solvent viscosity in the dynamics of protein conformational changes, *Science* **256**, 1796 (1992).
- [3] B. Zagrovic and V. Pande, Solvent viscosity dependence of the folding rate of a small protein: Distributed computing study, *J. Comput. Chem.* **24**, 1432 (2003).
- [4] B. Liebchen, P. Monderkamp, B. ten Hagen, and H. Löwen, Viscotaxis: Microswimmer Navigation in Viscosity Gradients, *Phys. Rev. Lett.* **120**, 208002 (2018).
- [5] C. Datt and G. J. Elfring, Active Particles in Viscosity Gradients, *Phys. Rev. Lett.* **123**, 158006 (2019).
- [6] J.-C. Bacri, R. Perzynski, M. I. Shliomis, and G. I. Burde, Negative-viscosity Effect in a Magnetic Fluid, *Phys. Rev. Lett.* **75**, 2128 (1995).
- [7] J. E. Avron, R. Seiler, and P. G. Zograf, Viscosity of Quantum Hall Fluids, *Phys. Rev. Lett.* **75**, 697 (1995).
- [8] R. W. Griffiths, The dynamics of lava flows, *Annu. Rev. Fluid Mech.* **32**, 477 (2000).
- [9] G. D. O. Lowe, A. J. Lee, A. Rumley, J. F. Price, and F. G. R. Fowkes, Blood viscosity and risk of cardiovascular events: The Edinburgh Artery Study, *Br. J. Haematol.* **96**, 168 (1997).
- [10] H. C. Kwaan, The hyperviscosity syndromes, *Semin. Thromb. Hemostasis* **29**, 433 (2003).
- [11] G. Tabilo-Munizaga and G. V. Barbosa-Cnovas, Rheology for the food industry, *J. Food Eng.* **67**, 147 (2005).
- [12] R. Maartens, Dissipative cosmology, *Classical Quantum Gravity* **12**, 1455 (1995).
- [13] J.-S. Gagnon and J. Lesgourgues, Dark goo: Bulk viscosity as an alternative to dark energy, *J. Cosmol. Astropart. Phys.* **09** (2011) 026.
- [14] F. M. White and J. Majdalani, *Viscous fluid flow*, 4th ed. (McGraw-Hill New York, 2022).
- [15] D. de las Heras, J. Renner, and M. Schmidt, Custom flow in overdamped Brownian dynamics, *Phys. Rev. E* **99**, 023306 (2019).
- [16] J. Renner, M. Schmidt, and D. de las Heras, Custom flow in molecular dynamics, *Phys. Rev. Research* **3**, 013281 (2021).
- [17] M. Schmidt and J. M. Brader, Power functional theory for brownian dynamics, *J. Chem. Phys.* **138**, 214101 (2013).
- [18] M. Schmidt, Power functional theory for Newtonian many-body dynamics, *J. Chem. Phys.* **148**, 044502 (2018).
- [19] D. de las Heras and M. Schmidt, Velocity Gradient Power Functional for Brownian Dynamics, *Phys. Rev. Lett.* **120**, 028001 (2018).
- [20] See Supplemental Material at <http://link.aps.org/supplemental/10.1103/PhysRevLett.128.094502> for details about simulations, custom flow, and power functional theory.
- [21] J. D. Weeks, D. Chandler, and H. C. Andersen, Role of repulsive forces in determining the equilibrium structure of simple liquids, *J. Chem. Phys.* **54**, 5237 (1971).
- [22] D. de las Heras and M. Schmidt, Flow and Structure in Nonequilibrium Brownian Many-Body Systems, *Phys. Rev. Lett.* **125**, 018001 (2020).
- [23] R. Kubo, The fluctuation-dissipation theorem, *Rep. Prog. Phys.* **29**, 255 (1966).
- [24] B. L. Holian, W. G. Hoover, B. Moran, and G. K. Straub, Shock-wave structure via nonequilibrium molecular dynamics and Navier-Stokes continuum mechanics, *Phys. Rev. A* **22**, 2798 (1980).
- [25] B. L. Holian, Modeling shock-wave deformation via molecular dynamics, *Phys. Rev. A* **37**, 2562 (1988).
- [26] E. Salomons and M. Mareschal, Usefulness of the Burnett Description of Strong Shock Waves, *Phys. Rev. Lett.* **69**, 269 (1992).
- [27] V. V. Zhakhovskii, S. V. Zybin, K. Nishihara, and S. I. Anisimov, Shock Wave Structure in Lennard-Jones Crystal via Molecular Dynamics, *Phys. Rev. Lett.* **83**, 1175 (1999).
- [28] M. Marciantie and M. S. Murillo, Thermodynamic and Kinetic Properties of Shocks in Two-Dimensional Yukawa Systems, *Phys. Rev. Lett.* **118**, 025001 (2017).
- [29] G. Falkovich, K. Gawędzki, and M. Vergassola, Particles and fields in fluid turbulence, *Rev. Mod. Phys.* **73**, 913 (2001).
- [30] L. Bentkamp, C. C. Lalescu, and M. Wilczek, Persistent accelerations disentangle Lagrangian turbulence, *Nat. Commun.* **10**, 3550 (2019).

- [31] S. Yamani, B. Keshavarz, Y. Raj, T. A. Zaki, G. H. McKinley, and I. Bischofberger, Spectral Universality of Elastoinertial Turbulence, *Phys. Rev. Lett.* **127**, 074501 (2021).
- [32] G. K. Vallis, *Atmospheric and Oceanic Fluid Dynamics* (Cambridge University Press, Cambridge, England, 2017).
- [33] G. R. Wang, F. Yang, and W. Zhao, There can be turbulence in microfluidics at low Reynolds number, *Lab Chip* **14**, 1452 (2014).
- [34] D. Di Carlo, Inertial microfluidics, *Lab Chip* **9**, 3038 (2009).
- [35] J. Zhang, S. Yan, D. Yuan, G. Alici, N.-T. Nguyen, M. Ebrahimi Warkiani, and W. Li, Fundamentals and applications of inertial microfluidics: A review, *Lab Chip* **16**, 10 (2016).
- [36] S. Roy, R. Raju, H. F. Chuang, B. A. Cruden, and M. Meyyappan, Modeling gas flow through microchannels and nanopores, *J. Appl. Phys.* **93**, 4870 (2003).
- [37] A. V. Straube, B. G. Kowalik, R. R. Netz, and F. Höfling, Rapid onset of molecular friction in liquids bridging between the atomistic and hydrodynamic pictures, *Commun. Phys.* **3**, 126 (2020).
- [38] N. Kavokine, R. R. Netz, and L. Bocquet, Fluids at the nanoscale: From continuum to subcontinuum transport, *Annu. Rev. Fluid Mech.* **53**, 377 (2021).
- [39] P. Coussot, *Mudflow Rheology and Dynamics* (Routledge, London, 2017).10.1201/9780203746349
- [40] M. P. Brenner, S. Hilgenfeldt, and D. Lohse, Single-bubble sonoluminescence, *Rev. Mod. Phys.* **74**, 425 (2002).
- [41] R. Toegel, S. Luther, and D. Lohse, Viscosity Destabilizes Sonoluminescing Bubbles, *Phys. Rev. Lett.* **96**, 114301 (2006).
- [42] M. Zakari and D. Jou, Equations of state and transport equations in viscous cosmological models, *Phys. Rev. D* **48**, 1597 (1993).
- [43] G. Jung, M. Hanke, and F. Schmid, Iterative reconstruction of memory kernels, *J. Chem. Theory Comput.* **13**, 2481 (2017).
- [44] H. Meyer, P. Pelagejcev, and T. Schilling, Non-Markovian out-of-equilibrium dynamics: A general numerical procedure to construct time-dependent memory kernels for coarse-grained observables, *Europhys. Lett.* **128**, 40001 (2020).
- [45] D. Lesnicki, R. Vuilleumier, A. Carof, and B. Rotenberg, Molecular Hydrodynamics from Memory Kernels, *Phys. Rev. Lett.* **116**, 147804 (2016).
- [46] J. O. Daldrop, B. G. Kowalik, and R. R. Netz, External Potential Modifies Friction of Molecular Solutes in Water, *Phys. Rev. X* **7**, 041065 (2017).

Supplementary Material

Shear and bulk acceleration viscosities in simple fluids

Johannes Renner,¹ Matthias Schmidt,¹ and Daniel de las Heras¹

¹*Theoretische Physik II, Physikalisches Institut, Universität Bayreuth, D-95440 Bayreuth, Germany*

(Dated: January 28, 2022)

The Supplementary Material contains the expression for the temporal contribution of the current, (A), the description of the calculation of the kernel parameters (B), details about molecular (C) and Brownian (D) dynamics simulations, summaries of the custom flow method (E), the splitting of internal forces into viscous and structural contributions (F) and power functional theory (G), as well as supplementary data on the shear flow in Brownian dynamics (H) and on the traveling shear wave (I).

A. Time evolution of the current

The temporal contribution to the current, shown in Fig.1(a) of the main text, is set to

$$J_t(t) = \begin{cases} 0.5 [1 - \cos(\pi t/t_\uparrow)], & 0 < t \leq t_\uparrow \\ 1, & t_\uparrow < t \leq t_c \\ 0.5 [1 + \cos(\pi \frac{t-t_c}{t_\downarrow-t_c})], & t_c < t \leq t_\downarrow \\ 0, & t_\downarrow < t, \end{cases} \quad (\text{S1})$$

with $t_\uparrow = 1\tau$, $t_c = 5\tau$, and $t_\downarrow = 6\tau$.

B. Calculation of the kernel parameters

To obtain the memory times and the amplitudes of the viscosity kernels we proceed as follows. For the bulk and the shear flows considered here, the one-body density is by construction time-independent $\rho(\mathbf{r}, t) = \rho(\mathbf{r})$ and the one-body current \mathbf{J} factorizes into time- and space-dependent parts $\mathbf{J}(\mathbf{r}, t) = \mathbf{J}_r(\mathbf{r})J_t(t)$. Hence, the time derivative of the current also factorizes into time- and space-dependent parts

$$\dot{\mathbf{J}}(\mathbf{r}, t) = \mathbf{J}_r(\mathbf{r})\dot{J}_t(t), \quad (\text{S2})$$

and it has the same spatial form $\mathbf{J}_r(\mathbf{r})$ as the current itself. Since the expressions for the shear \mathbf{f}_s and bulk \mathbf{f}_b viscous forces are linear in both $\mathbf{v} = \mathbf{J}/\rho = J_t\mathbf{J}_r/\rho$ and $\mathbf{a} = \dot{\mathbf{v}}$ where here $\dot{\mathbf{v}} = \dot{\mathbf{J}}/\rho = \dot{J}_t\mathbf{J}_r/\rho$ [see Eqs. (1) and (2) of the main text], the viscous forces also factorize into time- and space-dependent parts:

$$\mathbf{f}_\alpha(\mathbf{r}, t) = C_\alpha(t)\mathbf{f}_{r,\alpha}(\mathbf{r}), \quad \alpha = b, s, \quad (\text{S3})$$

where the space-dependent parts are

$$\mathbf{f}_{r,b} = \frac{1}{\rho} \nabla \left[\rho \rho \nabla \cdot \left(\frac{\mathbf{J}_r}{\rho} \right) \right], \quad (\text{S4})$$

$$\mathbf{f}_{r,s} = -\frac{1}{\rho} \nabla \times \left[\rho \rho \nabla \times \left(\frac{\mathbf{J}_r}{\rho} \right) \right], \quad (\text{S5})$$

and the temporal parts are

$$C_\alpha(t) = \int_0^t dt' \left(K_\alpha^\mathbf{v}(t-t')J_t(t') + K_\alpha^\mathbf{a}(t-t')\dot{J}_t(t') \right), \quad (\text{S6})$$

with $\alpha = b$ for bulk and $\alpha = s$ for shear. The kernels are

$$K_\alpha^\mathbf{\Gamma}(t) = \frac{c_\alpha^\mathbf{\Gamma}}{\tau_\alpha^\mathbf{\Gamma}} \exp(-t/\tau_\alpha^\mathbf{\Gamma}), \quad (\text{S7})$$

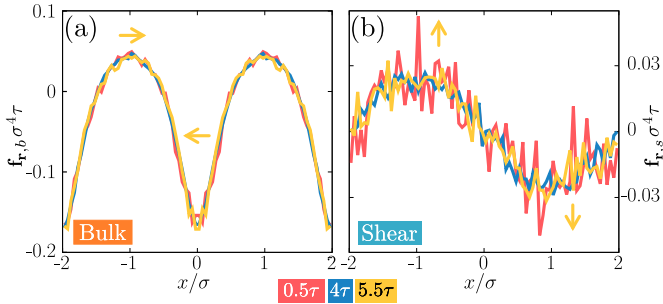
with the superscript $\mathbf{\Gamma}$ labeling either the acceleration $\mathbf{\Gamma} = \mathbf{a}$ or the velocity $\mathbf{\Gamma} = \mathbf{v}$ contributions. The factorization of the viscous force into temporal- and spatial parts, Eq. (S3), which facilitates the analysis of the data, is not general and holds only if the one-body current also factorizes. Custom flow is therefore an essential tool here since it allows to carefully prescribe the features of the flow. We show in Supplementary Fig. 1 the space-dependent parts of the bulk and shear viscous forces at different times according to simulations. As expected, the curves for different times collapse into a single curve.

The process to calculate the kernel parameters uses two steps. In step one, at every time t we compare the simulation data for \mathbf{f}_{vis} to Eq. (S3) using the expressions in Eqs. (S4) and (S5) for the spatial part of the viscous forces. As a result, we obtain the curve $C_\alpha(t)$ in simulations. In the second step, the kernel parameters are obtained by finding the values of $c_\alpha^\mathbf{\Gamma}$ and $\tau_\alpha^\mathbf{\Gamma}$ in Eq. (S6) that best reproduce the curve $C_\alpha(t)$ that results from step one.

C. Molecular dynamics simulations

We use molecular dynamics (MD) to simulate a dynamical ensemble of $\sim 10^6$ instances of a three-dimensional system consisting of $N = 50$ particles interacting via the purely repulsive Weeks-Chandler-Andersen interparticle-interaction potential [1]

$$\phi(r_{ij}) = \begin{cases} 4\epsilon \left[\left(\frac{\sigma}{r_{ij}} \right)^{12} - \left(\frac{\sigma}{r_{ij}} \right)^6 \right] & \text{if } r_{ij} \geq r_c \\ 0 & \text{otherwise.} \end{cases} \quad (\text{S8})$$



Supplementary Figure 1. Space-dependent parts of (a) the bulk $\mathbf{f}_{r,b}$ and (b) the shear $\mathbf{f}_{r,s}$ viscous forces as a function of the x -coordinate obtained with MD simulation data. Three different times are shown, as indicated by the color of the lines. The arrows indicate the direction of the vector field at the selected positions.

Here, $r_{ij} = |\mathbf{r}_i - \mathbf{r}_j|$ is the distance between particle i and j , and $r_c = 2^{\frac{1}{6}}\sigma$ is the cutoff radius, which is located at the minimum of the Lennard-Jones potential. We work in units of the length scale σ , the energy scale ϵ , and the mass of one particle m . Hence, the derived time scale is $\tau = \sqrt{m\sigma^2/\epsilon}$.

The equations of motion for the i th particle are

$$\frac{d\mathbf{r}_i}{dt} = \frac{\mathbf{p}_i}{m}, \quad (\text{S9})$$

$$\frac{d\mathbf{p}_i}{dt} = -\nabla_i u(\mathbf{r}^N) + \mathbf{f}_{\text{ext}}(\mathbf{r}_i, t), \quad (\text{S10})$$

where \mathbf{r}_i denotes the position of the i th particle, and $\mathbf{p}_i = m\mathbf{v}_i$ its momentum, with \mathbf{v}_i its velocity. The total force acting on the particle is made of an external contribution $\mathbf{f}_{\text{ext}}(\mathbf{r}_i, t)$, and an internal one, $-\nabla_i u(\mathbf{r}^N)$. Here, ∇_i is the partial derivative with respect to \mathbf{r}_i and $u(\mathbf{r}^N) = \frac{1}{2} \sum_i \sum_{j \neq i} \phi(r_{ij})$ is the total interparticle potential energy with, $\mathbf{r}^N = \{\mathbf{r}_1 \dots \mathbf{r}_N\}$ the complete set of particle positions.

We integrate the many-body equations of motion in MD using the standard velocity-Verlet algorithm with time step $dt = 10^{-4}\tau$. The simulation box is a cuboid with lengths $L_x = 4\sigma$, $L_y = 10\sigma$ and $L_z = 8\sigma$ and periodic boundary conditions. To spatially resolve the one-body fields we discretize the system in the x -coordinate with bins of size 0.05σ .

The particle positions are initialised randomly with the constraint that no interparticle interaction occur. The particle velocities are initialised following a Maxwell-Boltzmann distribution with absolute temperature T . For the initial equilibration of the shear flow (homogeneous density) we let the system evolve for 1τ without external force. To initialize the compressible flow (inhomogeneous density profile), we use custom flow to grow the density inhomogeneity and then let the system equilibrate for 4τ such that memory effects decay. The starting temperature, calculated from the kinetic energy using the equipartition theorem, is set to $k_B T/\epsilon = 0.59$ (compressible flow) and $k_B T/\epsilon = 0.486$ (shear flow). Here, k_B

is the Boltzmann constant. The temperatures of the final equilibrium states are $k_B T/\epsilon = 0.60$ and $k_B T/\epsilon = 0.492$ for the compressible and the shear flows, respectively. These values are slightly higher than the initial values due to the heating induced by the external driving. Since the temperature increase was small (below 2%) we did not use a thermostat. Note however that custom flow can also be implemented together with a thermostat [2].

The one-body fields of interest are resolved in space and in time. For example, the one-body density and current profiles are given by

$$\rho(\mathbf{r}, t) = \left\langle \sum_{i=1}^N \delta(\mathbf{r} - \mathbf{r}_i) \right\rangle, \quad (\text{S11})$$

$$\mathbf{J}(\mathbf{r}, t) = \left\langle \sum_{i=1}^N \delta(\mathbf{r} - \mathbf{r}_i) \mathbf{v}_i \right\rangle, \quad (\text{S12})$$

with $\delta(\mathbf{r})$ being the three dimensional Dirac delta distribution, and \mathbf{r} being the position vector. The statistical average, denoted by the brackets $\langle \cdot \rangle$ is done at each time t over different realizations of the initial conditions (the positions and the velocities of the particles at the initial time $t = 0$). Specifically, we average over $2 \cdot 10^6$ different realizations (initial states).

D. Brownian dynamics simulations

For the overdamped Brownian dynamics simulations we use the standard Euler algorithm to integrate the equation of motion of the i th particle

$$\mathbf{r}_i(t + dt) = \mathbf{r}_i(t) + \frac{dt}{\gamma} [-\nabla_i u(\mathbf{r}^N) + \mathbf{f}_{\text{ext}}(\mathbf{r}_i, t)] + \boldsymbol{\eta}_i(t), \quad (\text{S13})$$

where $\boldsymbol{\eta}_i$ is a delta-correlated Gaussian random displacement with standard deviation $\sqrt{2dt k_B T/\gamma}$ in accordance with the fluctuation-dissipation theorem and γ is the friction coefficient against the (implicit) solvent. We hence use in Eq. (S13) the standard assumption that the random force does not depend on the external force [3]. The integration time step is set to $dt = 10^{-4}\tau_b$ with $\tau_b = \sigma^2\gamma/\epsilon$ the BD unit of time. In BD we work in units of σ , ϵ , and γ . We average over $4 \cdot 10^6$ trajectories, i.e. twice than in MD, due to the larger statistical noise generated by the random force. The velocity of particle i at time t , required to e.g. sample the current following Eq. (S12), is calculated as the central derivative of the position vector [4]:

$$\mathbf{v}_i(t) = \frac{\mathbf{r}_i(t + dt) - \mathbf{r}_i(t - dt)}{2dt}. \quad (\text{S14})$$

All further parameters of the simulation, i.e. temperature, number of particles, and target fields, are the same as in MD.

Since the external driving is time-dependent, the overdamped approximation that underlies Eq. (S13) might

not be accurate. However, we use here overdamped BD only as a reference system in which inertial effects are eliminated by construction. This allows us to highlight the inertial effects that occur in MD.

E. Custom flow

Custom flow is a numerical method that finds the external force corresponding to prescribed density, velocity, and acceleration fields (the target fields). A complete description of the method is given in Refs. [2, 4]. Here, we only summarize the main ideas of custom flow in molecular dynamics. The external force is found iteratively. At each iteration, the external force is the same as in the previous iteration plus a term that aims to correct the differences between sampled and target fields,

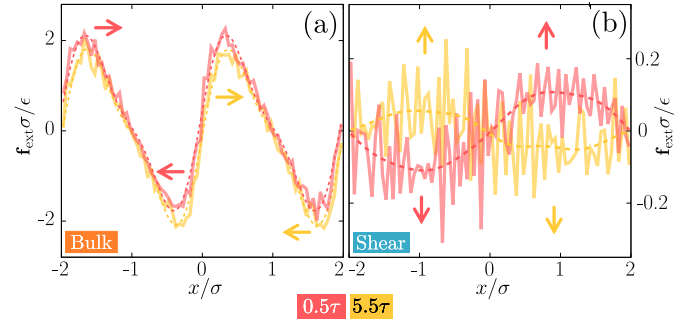
$$\mathbf{f}_{\text{ext}}^{(k+1)}(\mathbf{r}, t) = \mathbf{f}_{\text{ext}}^{(k)}(\mathbf{r}, t) + \frac{m}{\rho(\mathbf{r}, t)\Delta t} \left(\mathbf{J}(\mathbf{r}, t) - \mathbf{J}^{(k)}(\mathbf{r}, t) \right). \quad (\text{S15})$$

Here, k is the iteration index. Hence, $\mathbf{f}_{\text{ext}}^{(k)}(\mathbf{r}, t)$ and $\mathbf{J}^{(k)}(\mathbf{r}, t)$ denote the external force and the current sampled at iteration k , whereas $\rho(\mathbf{r}, t)$ and $\mathbf{J}(\mathbf{r}, t)$ are the target fields. The convergence of the iteration scheme (S15) is achieved when the external forces at iterations $k+1$ and k coincide within a given tolerance (in practice less than ten iterations are usually enough to achieve convergence). The whole iteration scheme needs to be repeated at time intervals separated by Δt which we set to be $\Delta t = 10dt$, i.e., ten times bigger than the time step of the simulation dt . At each time, we initialize the external force according to

$$\mathbf{f}_{\text{ext}}^{(0)}(\mathbf{r}, t) = \frac{m\dot{\mathbf{J}}(\mathbf{r}, t)}{\rho(\mathbf{r}, t)}, \quad (\text{S16})$$

which follows from the exact one-body force balance equation (S30) by making the internal force \mathbf{f}_{int} and the transport term $\nabla \cdot \boldsymbol{\tau}$ zero everywhere.

Using Eq. (S15), custom flow MD minimizes the difference between target and sampled one-body currents. This results in very accurate (essentially noise free) sampled currents. The noise, which in standard MD simulations usually occurs in the sampled fields, appears in custom flow in the external force which is tailored to the initial set of microstates (we use $2 \cdot 10^6$ different initial states), see Supplementary Figure 2. For a better visual representation we show in the main paper and also in Supplementary Figure 2 smooth external force profiles which result from removing the high Fourier modes of the raw signal. Both, the external force that follows directly from custom flow and its smoothed version produce very similar dynamics [2].



Supplementary Figure 2. External force \mathbf{f}_{ext} produced by MD custom flow (solid thick lines) as a function of x for (a) bulk and (b) shear flows at times 0.5τ (red) and 5.5τ (yellow). The smoothed external forces, obtained by removing the high frequency modes, are also shown with dashed lines. Custom flow minimizes the statistical noise that usually occurs in the sampled fields like the density and the velocity profiles. As a result, the external forces obtained with custom flow appear to be noisy. The colored arrows indicate the direction of the force at the selected positions.

F. Viscous and structural internal forces

In non-equilibrium, the total internal force \mathbf{f}_{int} , which is solely generated by the interparticle interactions, contains structural and flow contributions [5]. The structural part is able to e.g. sustain gradients in the density profile, whereas the flow contribution represents the viscous response of the system. The total internal force is easily accessible in computer simulations since $\mathbf{f}_{\text{int}}(\mathbf{r}, t) = \mathbf{F}_{\text{int}}(\mathbf{r}, t)/\rho(\mathbf{r}, t)$ with \mathbf{F}_{int} being the internal force density

$$\mathbf{F}_{\text{int}}(\mathbf{r}, t) = - \left\langle \sum_{i=1}^N \delta(\mathbf{r} - \mathbf{r}_i) \nabla_i u(\mathbf{r}^N) \right\rangle. \quad (\text{S17})$$

To extract the viscous forces from the total internal force, we use that the viscous forces are sensitive to the direction of the flow. Hence, reversing the direction of the flow, i.e., $\mathbf{v} \rightarrow -\mathbf{v}$ and $\mathbf{a} \rightarrow -\mathbf{a}$ while keeping the density profile unchanged, flips the sign of the viscous forces and leaves the structural forces unchanged [5]. The sign change of \mathbf{f}_{vis} by reversing the direction of the flow is apparent in Eqs. (1) and (2) of the main text.

Hence, the total viscous force of the system can be calculated as [5]

$$\mathbf{f}_{\text{vis}}(\mathbf{r}, t) = \frac{\mathbf{f}_{\text{int}}(\mathbf{r}, t) - \mathbf{f}_{\text{int}}^r(\mathbf{r}, t)}{2}, \quad (\text{S18})$$

where $\mathbf{f}_{\text{int}}^r(\mathbf{r}, t)$ indicates the internal force in the reverse system, i.e. a system with flow velocity $-\mathbf{v}(\mathbf{r}, t)$, acceleration $-\mathbf{a}(\mathbf{r}, t)$, but the same density profile $\rho(\mathbf{r}, t)$ as the original forward system [in which the flow is given by $+\mathbf{v}(\mathbf{r}, t)$ and $+\mathbf{a}(\mathbf{r}, t)$ and the internal force is $\mathbf{f}_{\text{int}}(\mathbf{r}, t)$].

Using Eq. (S18) to measure the viscous force is always possible if the density profile is time-independent, such

as e.g. steady states and the full non-equilibrium flows designed here. If the density varies in time, then temporal changes of the density profile affect the flow (via the continuity equation). In such cases finding the reverse system to unambiguously measure the viscous force is in general not possible. This again highlights the importance of custom flow that allows us to generate flows in which the viscous response can be unambiguously measured.

To create the reverse system we follow two independent methods which give the same results. The first method simply uses custom flow to prescribe the respective reverse flow and find the corresponding external force. The second method makes use of symmetry arguments to compute the reverse flow from the forward flow and hence obtain $\mathbf{f}_{\text{int}}^r$ from \mathbf{f}_{int} . This second possibility, which we describe in detail in what follows, is possible only due to the specific characteristics of the flows. In the general case the first method is required to find the reverse system.

Bulk flow. Let us consider a virtual flow in which we reverse at each time t only the x -component of every particle in the original flow, i.e. we perform the operation $x_i(t) \rightarrow -x_i(t)$ while keeping the other two components unchanged. Hence, the x -component of the current in this virtual system, J_x^v , is

$$\begin{aligned} J_x^v &= \left\langle \sum_{i=1}^N \delta(x - (-x_i)) \frac{d(-x_i)}{dt} \right\rangle \\ &= - \left\langle \sum_{i=1}^N \delta(x + x_i) v_i^x \right\rangle = -J_x(-x, t). \end{aligned} \quad (\text{S19})$$

By construction, the bulk flow has the symmetry $J_x(x, t) = J_x(-x, t)$. Hence, in combination with Eq. (S19) above we conclude that $J_x^v(x, t) = J_x^r(x, t)$. Also by construction, the other components of the current vanish and the density profile has also the same symmetry $\rho(x, t) = \rho(-x, t)$. Therefore, we can construct the reverse system of the bulk flow by simply using the trajectories of the forward system and performing the operation $x_i(t) \rightarrow -x_i(t)$.

Hence, for the bulk flow the x -component of the internal force density in the reverse system is

$$F_{\text{int},x}^r(x, t) = \left\langle \sum_{i=1}^N \delta(x + x_i) \frac{\partial \phi(r_{ij})}{\partial (-x_i)} \right\rangle \quad (\text{S20})$$

$$= - \left\langle \sum_{i=1}^N \delta(x + x_i) \frac{\partial \phi(r_{ij})}{\partial x_i} \right\rangle \quad (\text{S21})$$

$$= -F_{\text{int},x}(-x, t), \quad (\text{S22})$$

where we have used that the interparticle distance r_{ij} is not affected by the transformation $x_i \rightarrow -x_i$. Due to the spatial symmetry of the density profile $\rho(x, t) = \rho(-x, t)$, the internal force \mathbf{f}_{int} has the same symmetry as the internal force density \mathbf{F}_{int} , i.e. $f_{\text{int},x}^r(x, t) = -f_{\text{int},x}^r(-x, t)$ because $\mathbf{F}_{\text{int}} = \mathbf{f}_{\text{int}}/\rho$. Therefore, for the bulk flow the

viscous part of the total internal force, see Eq. (S18), can be obtained from the forward bulk flow as a simple arithmetic mean

$$f_{\text{vis},x}(x, t) = \frac{f_{\text{int},x}(x, t) + f_{\text{int},x}(-x, t)}{2}. \quad (\text{S23})$$

Shear flow. Here, the flow is directed along the y -axis and the density is homogeneous $\nabla \rho = 0$. Therefore, by construction, the y -component of the internal force is only of viscous nature (no structural term). We arrive at the same conclusion by considering a virtual flow in which we reverse at each time the y -component of all particles, i.e. $y_i(t) \rightarrow -y_i(t)$. Hence, the y -component of the current in the virtual system J_y^v is

$$J_y^v(x, t) = \left\langle \sum_{i=1}^N \delta(x - x_i) \frac{d(-y_i)}{dt} \right\rangle \quad (\text{S24})$$

$$= - \left\langle \sum_{i=1}^N \delta(x - x_i) v_i^y \right\rangle = -J_y(x, t), \quad (\text{S25})$$

which is precisely the y -component of the current in the reverse system $J_y^r(x, t) = J_y^v(x, t)$. Given that the other two components of the current vanish and that the density profile is stationary, we conclude that the reverse system can be obtained from the forward flow by simply using the operation $y_i(t) \rightarrow -y_i(t)$ and performing the desired averages.

The y -component of the internal force density in the reverse system is therefore

$$F_{\text{int},y}^r(x, t) = \left\langle \sum_{i=1}^N \delta(x - x_i) \frac{\partial \phi(r_{ij})}{\partial (-y_i)} \right\rangle \quad (\text{S26})$$

$$= - \left\langle \sum_{i=1}^N \delta(x - x_i) \frac{\partial \phi(r_{ij})}{\partial y_i} \right\rangle \quad (\text{S27})$$

$$= -F_{\text{int},y}(x, t). \quad (\text{S28})$$

Hence, using Eq. (S18), the viscous part is

$$f_{\text{vis},y}(x, t) = \frac{f_{\text{int},y}(x, t) + f_{\text{int},y}(-x, t)}{2} = f_{\text{int},y}(x, t). \quad (\text{S29})$$

That is, as expected, the flow-direction of the internal force in a shear flow contains only viscous terms provided that there is no density inhomogeneity in the flow direction.

G. Power functional theory

Power functional theory (PFT) is a variational theory that describes the dynamics of interacting many-body overdamped [6] and inertial [7] systems at the level of one-body fields. A variational principle produces by construction the exact one-body force balance equation of

the system. For a classical system of particles following the equations of motion (S9) and (S10), the exact one-body force balance equation reads [7]

$$m\dot{\mathbf{J}}(\mathbf{r}, t) = \rho(\mathbf{r}, t) [\mathbf{f}_{\text{ext}}(\mathbf{r}, t) + \mathbf{f}_{\text{int}}(\mathbf{r}, t)] + \nabla \cdot \boldsymbol{\tau}(\mathbf{r}, t), \quad (\text{S30})$$

where the last term involves the divergence of the second rank kinetic stress tensor $\boldsymbol{\tau}$ and it describes transport effects that arise due to the one-body description of the dynamics. In thermal equilibrium this term reduces to diffusive transport $\nabla \cdot \boldsymbol{\tau} = -k_B T \nabla \rho$. In simulations, $\boldsymbol{\tau}$ can be sampled via

$$\boldsymbol{\tau}(\mathbf{r}, t) = -m \left\langle \sum_{i=1}^N \delta(\mathbf{r} - \mathbf{r}_i) \mathbf{v}_i \mathbf{v}_i \right\rangle, \quad (\text{S31})$$

where $\mathbf{v}_i \mathbf{v}_i$ indicates the dyadic product of the velocity of particle i with itself.

Within PFT each term of the force balance equation (S30) is generated via a functional derivative of a corresponding functional generator with respect to the time derivative of the current or alternatively with respect to the acceleration field. The density profile ρ , the current \mathbf{J} (or the velocity $\mathbf{v} = \mathbf{J}/\rho$), and the time derivative of the current $\dot{\mathbf{J}}$ (or the acceleration $\mathbf{a} = \dot{\mathbf{v}} = \dot{\mathbf{J}}/\rho$, where the second equality holds only if $\dot{\rho} = 0$ like in the present work) are the natural functional dependencies of the generator functionals. One important task in PFT is to find an approximated functional that generates via functional differentiation the internal force field.

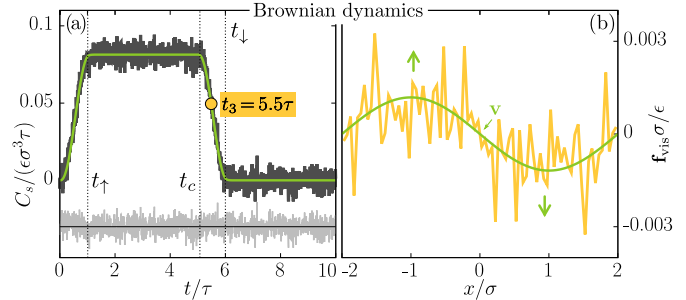
The simplest approximation based on an expansion in terms of the acceleration gradient $\nabla \mathbf{a}$ that is (i) compatible with the symmetry requirements of the viscous force (the force must flip sign under flow reversal) and that (ii) respects the rotational invariance of the system under global rotations is

$$\begin{aligned} G_b[\rho, \mathbf{v}, \mathbf{a}] &= \int d\mathbf{r} \int_0^t dt' K_b^v(t-t') \rho'(\nabla \cdot \mathbf{v}')(\nabla \cdot \mathbf{a})\rho \\ &+ \int d\mathbf{r} \int_0^t dt' K_b^a(t-t') \rho'(\nabla \cdot \mathbf{a}')(\nabla \cdot \mathbf{a})\rho, \end{aligned} \quad (\text{S32})$$

$$\begin{aligned} G_s[\rho, \mathbf{v}, \mathbf{a}] &= \int d\mathbf{r} \int_0^t dt' K_s^v(t-t') \rho'(\nabla \times \mathbf{v}') \cdot (\nabla \times \mathbf{a})\rho \\ &+ \int d\mathbf{r} \int_0^t dt' K_s^a(t-t') \rho'(\nabla \times \mathbf{a}') \cdot (\nabla \times \mathbf{a})\rho, \end{aligned} \quad (\text{S33})$$

where we have omitted the dependencies of the one-body fields, e.g. $\rho = \rho(\mathbf{r}, t)$, primed fields are evaluated at t' , e.g. $\rho' = \rho(\mathbf{r}, t')$, and the spatial integral runs over the whole system. Analogue expressions arise in overdamped Brownian dynamics based on an expansion in terms of the velocity gradient $\nabla \mathbf{v}$ [8].

The shear \mathbf{f}_s and bulk \mathbf{f}_b viscous forces shown in Eqs. (1) and (2) of the main text are then generated via the



Supplementary Figure 3. (a) Temporal dependency of the shear viscous force C_s as a function of time t in Brownian dynamics simulations (thick black line) and theoretically (green) for the shear flow described in the main text. The vertical dotted lines indicate the times t_\uparrow , t_c , and t_\downarrow . The time $t_3 = 5.5\tau$ is highlighted with a yellow circle. The light grey line fluctuating around the horizontal line is the difference between simulation (thick black) and theory (violet). (b) Shear viscous force \mathbf{f}_{vis} as a function of x at time $t_3 = 5.5\tau$ according to BD (yellow) and theory (green). The force points along the y -axis. The colored arrows indicate the direction of the force at the selected positions.

functional derivative

$$\mathbf{f}_\alpha(\mathbf{r}, t) = -\frac{\delta G_\alpha}{\delta \dot{\mathbf{J}}(\mathbf{r}, t)} = -\frac{1}{\rho} \frac{\delta G_\alpha}{\delta \mathbf{a}(\mathbf{r}, t)}, \quad \alpha = b, s, \quad (\text{S34})$$

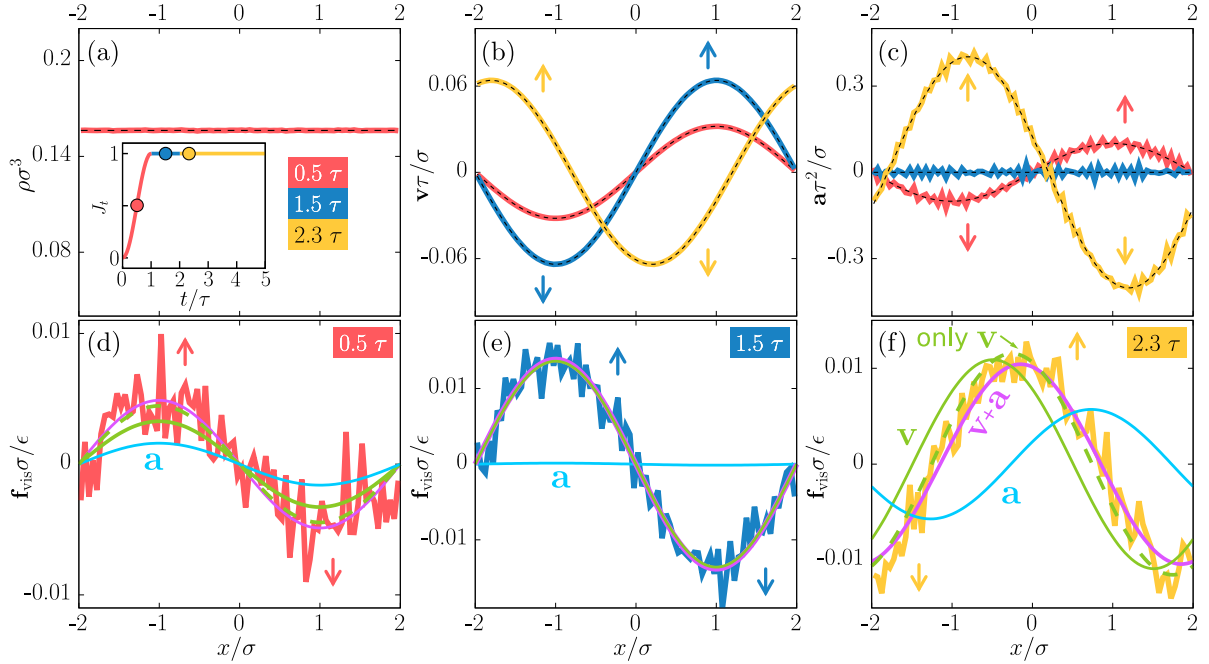
where the derivative is taken at time t with respect to either $\dot{\mathbf{J}}$ or \mathbf{a} and considering that the fields $\rho(\mathbf{r}, t')$, $\mathbf{v}(\mathbf{r}, t')$, and $\mathbf{a}(\mathbf{r}, t')$ are kept fixed at their real physical values for all previous times $t' < t$. Hence, the functional derivative in Eq. (S34) acts only on the unprimed terms $\mathbf{a}(\mathbf{r}, t)$ of Eqs. (S32) and (S33) but not on the primed $\mathbf{a}' = \mathbf{a}(\mathbf{r}, t')$ ones.

H. Shear flow in Brownian dynamics

As in the case of the compressible flow, we have also analysed the shear flow using Brownian dynamics simulations. Since the acceleration field does not play any role in overdamped Brownian dynamics, the velocity field alone reproduces the complete shear viscous force. We show in Supplementary Fig. 3 the temporal part $C_s(t)$ of the viscous force vs time, and the viscous force vs the x -coordinate for a given time obtained in Brownian dynamics simulations along with the corresponding theoretical predictions [kernel parameters $c_s^v/(\epsilon\sigma^3\tau) = 0.081$ and $\tau_s^v/\tau = 0.059$]. The parameters of the flow are identical to those used in MD (see main text).

I. Traveling shear wave

For the traveling shear wave, the current follows up to $t = 2\tau$ the same time evolution as in the shear case, see Eqs. (8) and (9) of the main text. After $t = 2\tau$, the shear



Supplementary Figure 4. Density (a), velocity (b), and acceleration (c) profiles vs the x -coordinate for the shear flow with a traveling wave. Three different times 0.5τ (red), 1.5τ (blue), and 2.3τ (yellow) are shown. Solid lines are simulation data sampled using custom flow and thin black-dashed lines are the corresponding target fields. The inset in (a) shows the temporal dependency of the current with the three different regimes highlighted using different color and the selected times indicated by colored circles. The amplitude of the current increases until $t/\tau = 1$ (red) and then it remains constant until the simulation ends. The shear wave is stationary at first (blue) and then it starts to travel for $t/\tau > 2$ (yellow). Panels (d), (e), and (f) show the shear viscous force at different times (as indicated) obtained in simulations (thick solid lines) along with the theoretical prediction using the acceleration and the velocity contributions (violet) and also using only the velocity contribution (dashed green). The individual contributions of the velocity (solid green) and of the acceleration (blue) to the total signal (violet) are also shown. Once the shear wave is traveling (f) there is a clear phase shift between the simulation data (yellow) and the prediction using only the velocity (dashed green). Using both contributions (violet) the simulation data is correctly reproduced. The color arrows indicate the direction of the respective vector field at the selected positions.

wave starts to move with constant velocity $v_s = 4\sigma/\tau$ and constant amplitude, i.e.

$$\mathbf{J}(\mathbf{r}, t) = J_0 \sin\left(\frac{2\pi(x - v_s t)}{L_x}\right) \hat{\mathbf{e}}_y, \quad t > 2\tau, \quad (\text{S35})$$

where, as in the non-traveling shear case, $L_x/\sigma = 4$ and $J_0\tau\sigma^2 = 0.01$. Representative states for each of the regimes of the traveling shear flow are shown in Supplementary Fig. 4. The density (a) remains constant in space at every time. The amplitudes of the velocity (b) and of the acceleration (c) increase until $t = 1\tau$. To relax memory effects, the velocity profile remains stationary from 1τ to 2τ . Hence, the acceleration vanishes everywhere in that time period. Then, the traveling wave begins to move and the velocity field changes its phase with constant speed. Therefore, the acceleration field has a constant instantaneous phase shift of $\pi/2$ with respect to the velocity field. This is different from what we

considered in the static shear wave and allows us to test our model for the shear viscous force. The shear viscous forces at three different times are shown in panels (d), (e), and (f) of Supplementary Fig. 4. We show the data sampled in molecular dynamics simulations along with the theoretical predictions which we calculate with the same kernel parameters previously obtained for the static shear wave flow. The agreement between simulation and theory is excellent, not only before the wave starts to travel (d,e), which was expected from the static shear case, but also during the traveling wave (f). The phase shift between \mathbf{v} and \mathbf{a} has an effect on the viscous force that is theoretically reproduced. In contrast, if we use only the velocity dependent part of the viscous force and the same kernel parameters as for the static case, there is a phase shift between the theoretical predictions and the simulation data. The acceleration field is therefore required to describe the data accurately.

[1] John D. Weeks, David Chandler, and Hans C. Andersen, “Role of repulsive forces in determining the equilib-

rium structure of simple liquids,” J. Chem. Phys **54**, 5237

- (1971).
- [2] Johannes Renner, Matthias Schmidt, and Daniel de las Heras, “Custom flow in molecular dynamics,” *Phys. Rev. Res.* **3**, 013281 (2021).
 - [3] R. Kubo, “The fluctuation-dissipation theorem,” *Rep. Prog. Phys.* **29**, 255–284 (1966).
 - [4] D. de las Heras, J. Renner, and M. Schmidt, “Custom flow in overdamped Brownian dynamics,” *Phys. Rev. E* **99**, 023306 (2019).
 - [5] Daniel de las Heras and Matthias Schmidt, “Flow and structure in nonequilibrium brownian many-body systems,” *Phys. Rev. Lett.* **125**, 018001 (2020).
 - [6] M. Schmidt and J. M. Brader, “Power functional theory for brownian dynamics,” *J. Chem. Phys.* **138**, 214101 (2013).
 - [7] Matthias Schmidt, “Power functional theory for Newtonian many-body dynamics,” *J. Chem. Phys.* **148**, 044502 (2018).
 - [8] D. de las Heras and M. Schmidt, “Velocity gradient power functional for Brownian dynamics,” *Phys. Rev. Lett.* **120**, 028001 (2018).

PAPER • OPEN ACCESS

Reduced-variance orientational distribution functions from torque sampling

To cite this article: Johannes Renner *et al* 2023 *J. Phys.: Condens. Matter* **35** 235901

View the [article online](#) for updates and enhancements.

You may also like

- [Neutron scattering study of the orientational disorder in potassium cyanide](#)
Guanqun Cai, Anthony E Phillips, David A Keen *et al.*
- [Hard-body models of bulk liquid crystals](#)
Luis Mederos, Enrique Velasco and Yuri Martínez-Ratón
- [Determination of the orientational order parameter of the homologous series of 4-cyanophenyl 4-alkylbenzoate \(n.CN\) by different methods](#)
Malay Kumar Das, Gautam Sarkar, Banani Das *et al.*

Reduced-variance orientational distribution functions from torque sampling

Johannes Renner¹, Matthias Schmidt¹  and Daniel de las Heras^{1,*} 

Theoretische Physik II, Physikalisches Institut, Universität Bayreuth, D-95440 Bayreuth, Germany

E-mail: delasheras.daniel@gmail.com

Received 15 December 2022, revised 24 February 2023

Accepted for publication 8 March 2023

Published 28 March 2023



CrossMark

Abstract

We introduce a method to sample the orientational distribution function in computer simulations. The method is based on the exact torque balance equation for classical many-body systems of interacting anisotropic particles in equilibrium. Instead of the traditional counting of events, we reconstruct the orientational distribution function via an orientational integral of the torque acting on the particles. We test the torque sampling method in two- and three-dimensions, using both Langevin dynamics and overdamped Brownian dynamics, and with two interparticle interaction potentials. In all cases the torque sampling method produces profiles of the orientational distribution function with better accuracy than those obtained with the traditional counting method. The accuracy of the torque sampling method is independent of the bin size, and hence it is possible to resolve the orientational distribution function with arbitrarily small angular resolutions.

Keywords: torque balance, orientational distribution function, torque sampling, reduced variance, liquid crystals

(Some figures may appear in colour only in the online journal)

1. Introduction

The spatial and orientational order in classical equilibrium many-body systems is the result of a delicate balance between forces and torques of internal, entropic (diffusive), and external origin. One-body distribution functions, obtained as statistical averages resolved in either space, orientation or both of these, are essential for the description and understanding of the organization of many-body systems at the microscopic level. For example, the density profile, which is an average

over a statistical ensemble of the number of particles at a given position, provides information about the spatial structure of the many-body system. Traditionally, the density profile in computer simulations has been obtained by discretizing the simulation box and counting the number of particles in each element of the grid. Since the structure of the many-body system is the result of a force balance, an alternative to counting events in order to obtain the density profile consists of reconstructing it from the spatially resolved force contributions [1, 2]. The density profiles obtained via force-sampling methods have a reduced variance as compared to those obtained via the traditional counting method. Moreover, the density at a given position is constructed with information from the whole system. As a result the error in the density profile does not depend on the size of the elements of the grid [1, 2]. The density profile can therefore be resolved with arbitrarily high spatial resolution without increasing the computational cost. This is particularly

* Author to whom any correspondence should be addressed.



Original Content from this work may be used under the terms of the [Creative Commons Attribution 4.0 licence](https://creativecommons.org/licenses/by/4.0/). Any further distribution of this work must maintain attribution to the author(s) and the title of the work, journal citation and DOI.

useful for sampling two- [2] and three-dimensional [3] density profiles. Force-based estimators can be also used to improve the sampling of the radial distribution function [1, 4, 5], and that of the correlation functions required in the Green–Kubo expressions relevant for mobility profiles [6].

It is interesting to note that force-sampling methods can be derived from the general and versatile mapped averaging framework [7–11], in which approximate theoretical results are used to reformulate an ensemble average with reduced variance. Reduced-variance estimators were first introduced in classical and quantum Monte Carlo simulations [12, 13]. An account of reduced-variance estimators that make use of force sampling methods is given in a recent review [14].

Beyond constructing statistical estimators with low variance in equilibrium systems, the internal force can be used to derive force-based density functional theories [15, 16], and it plays a fundamental role in the construction of exact sum rules using the symmetries of the system [17–19]. Moreover, the use of the thermodynamic force can also improve the accuracy of adaptive resolution schemes [20] in which the simulation box is split in regions that can be treated with different levels of resolution [21–23]. Another potential application of force sampling methods is to improve the convergence of Kirkwood–Buff [24] integrals in molecular simulations [25].

Moreover, the knowledge of the internal force field is not only beneficial in equilibrium systems. The adiabatic approximation, which substitutes the non-equilibrium internal forces by those in an equilibrium system, is at the core of popular dynamical theories such as dynamic density functional theory (DDFT) [26–30]. Sampling the internal forces in many-body non-equilibrium simulations and comparing them to those in equilibrium systems is therefore crucial to develop and test the accuracy of dynamical theories that go beyond the adiabatic approximation such as superadiabatic-DDFT [31] and power functional [32–34] theories. Knowledge of the non-equilibrium internal forces facilitates also the construction of the external force field that generates a desired dynamical response via custom flow methods [35, 36], and serves to gain insight into physical processes such as the occurrence of viscous forces generated by the acceleration field [37].

In systems with translational and rotational degrees of freedom, such as liquid crystals, it is not only the forces but also the torques that are crucial in the determination of the equilibrium and non-equilibrium properties of the many-body system. The force balance equation is complemented and coupled with a torque balance equation. Together, the force and the torque balance equations determine in equilibrium the positional and the orientational order of the system.

Here, we demonstrate that torque sampling, i.e. the analogue to force sampling in systems with orientational degrees of freedom, significantly improves the sampling of the orientational distribution function in computer simulations as compared to traditional counting methods. As a proof of concept, we sample the torques using several differing types of dynamics (overdamped Brownian and Langevin dynamics), dimensionality (two- and three-dimensional systems), interparticle interaction potential (rectangular and Gay–Berne particles), type of orientational order (uniaxial and tetratic), and overall

density. In all cases, torque sampling outperforms the traditional counting method.

2. Theory

We consider here classical systems of N identical interacting particles governed by either Langevin or overdamped Brownian dynamics. Exact one-body force and torque balance equations hold in equilibrium, and can be used to calculate one-body distribution functions from the forces and torques acting in the system. We start by revisiting the force balance equation in a many-body system with only translational degrees of freedom.

2.1. Force balance equation for isotropic particles

In many-body systems with only translational degrees of freedom, such as a system of isotropic particles (e.g. a fluid of Lennard-Jones particles), the exact one-body force density balance equation in equilibrium reads [15, 38]

$$0 = -k_B T \nabla \rho(\mathbf{r}) + \mathbf{F}(\mathbf{r}). \quad (1)$$

The first term on the right hand side of equation (1) stems from the (ideal gas) diffusion, with k_B being the Boltzmann constant, T is absolute temperature, ∇ is the derivative with respect to the spatial coordinate \mathbf{r} , and $\rho(\mathbf{r})$ is the one-body density distribution which is given by

$$\rho(\mathbf{r}) = \left\langle \sum_i \delta(\mathbf{r} - \mathbf{r}_i) \right\rangle, \quad (2)$$

where the angles denote a statistical average over an equilibrium ensemble, $\delta(\cdot)$ is the Dirac distribution, \mathbf{r}_i is the position of particle i , and the sum runs over all the particles in the system.

The second term on the right hand side of equation (1) is the force density profile, given by

$$\mathbf{F}(\mathbf{r}) = \left\langle \sum_i \delta(\mathbf{r} - \mathbf{r}_i) \mathbf{f}_i(\mathbf{r}^N) \right\rangle, \quad (3)$$

where \mathbf{f}_i is the sum of the internal and the external forces acting on particle i in microstate $\mathbf{r}^N = \mathbf{r}_1 \dots \mathbf{r}_N$ with N particles. That is

$$\mathbf{f}_i(\mathbf{r}^N) = -\nabla_i u(\mathbf{r}^N) + \mathbf{f}_{\text{ext}}(\mathbf{r}_i), \quad (4)$$

where ∇_i is the derivative with respect to \mathbf{r}_i , and $u(\mathbf{r}^N)$ is the total interparticle interaction potential. In equilibrium, the (imposed) external force $\mathbf{f}_{\text{ext}}(\mathbf{r})$ must be conservative and hence

$$\mathbf{f}_{\text{ext}}(\mathbf{r}) = -\nabla V_{\text{ext}}(\mathbf{r}), \quad (5)$$

with $V_{\text{ext}}(\mathbf{r})$ an imposed external potential. The force profile follows directly from the force density profile via normalization with the density profile, i.e. $\mathbf{f}(\mathbf{r}) = \mathbf{F}(\mathbf{r})/\rho(\mathbf{r})$.

The sum of the ideal, internal, and external force densities vanishes everywhere in space since the system is in equilibrium. Otherwise there would be a net flow of particles. In equilibrium, the exact force density balance equation, equation (1), holds in systems following either Newtonian dynamics, Langevin dynamics, or overdamped Brownian dynamics.

Both, the density profile $\rho(\mathbf{r})$ and the force density profile $\mathbf{F}(\mathbf{r})$, can be easily sampled in computer simulations via equations (2) and (3), respectively. Sampling $\rho(\mathbf{r})$ via equation (2) is the traditional method of counting of events of particle occurrences at space points.

The exact force density balance equation, equation (1), can also be used to calculate the density profile $\rho(\mathbf{r})$ via the forces instead of the direct traditional counting method. Inverting equation (1) results in

$$\rho(\mathbf{r}) = \rho_0 + (k_B T)^{-1} \nabla^{-1} \cdot \mathbf{F}(\mathbf{r}), \quad (6)$$

with ρ_0 a constant and ∇^{-1} the inverse ∇ operator. In effectively one-dimensional systems (e.g. planar geometry), the profiles depend only on one space coordinate and hence the ∇^{-1} operator reduces to a simple spatial integral. Different approaches can be used to solve equation (6) in more general geometries [2]. The unknown integration constant ρ_0 in equation (6) can be determined via normalization of the density

$$\int d\mathbf{r} \rho(\mathbf{r}) = N, \quad (7)$$

where the integral is over the whole system volume. Results for the density profile calculated via force sampling, equation (6), carry a statistical uncertainty smaller than that of the standard counting method [2] since (i) force sampling avoids the inherent ideal gas fluctuations, and (ii) uses non-local information, the forces in the whole system, to determine the density profile at each space point.

2.2. Torque balance equation for anisotropic particles

For anisotropic particles, the one-body density distribution depends not only on the space coordinate \mathbf{r} but also on the orientation, which is denoted here by the unit vector $\hat{\mathbf{u}}$:

$$\rho(\mathbf{r}, \hat{\mathbf{u}}) = \left\langle \sum_i \delta(\mathbf{r} - \mathbf{r}_i) \delta(\hat{\mathbf{u}} - \hat{\mathbf{u}}_i) \right\rangle. \quad (8)$$

In addition to the exact equilibrium one-body force density balance equation,

$$0 = -k_B T \nabla \rho(\mathbf{r}, \hat{\mathbf{u}}) + \mathbf{F}(\mathbf{r}, \hat{\mathbf{u}}), \quad (9)$$

there exists an exact one-body torque density balance equation:

$$0 = -k_B T \hat{\mathbf{R}} \rho(\mathbf{r}, \hat{\mathbf{u}}) + \mathbf{T}(\mathbf{r}, \hat{\mathbf{u}}). \quad (10)$$

Here, $\mathbf{F}(\mathbf{r}, \hat{\mathbf{u}})$ and $\mathbf{T}(\mathbf{r}, \hat{\mathbf{u}})$ are the force density and the torque density, respectively. Both, $\mathbf{F}(\mathbf{r}, \hat{\mathbf{u}})$ and $\mathbf{T}(\mathbf{r}, \hat{\mathbf{u}})$, contain

external and internal (inter-particle) contributions and they depend in general on position and orientation. As before, ∇ is the gradient operator acting on the position, and $\hat{\mathbf{R}}$ is the orientational counterpart acting on the orientation $\hat{\mathbf{u}}$, i.e.

$$\hat{\mathbf{R}} = \hat{\mathbf{u}} \times \nabla_{\hat{\mathbf{u}}}, \quad (11)$$

with $\nabla_{\hat{\mathbf{u}}}$ the derivative with respect to the Cartesian coordinates of $\hat{\mathbf{u}}$.

The one-body torque density is accessible in computer simulations via

$$\mathbf{T}(\mathbf{r}, \hat{\mathbf{u}}) = \left\langle \sum_i \delta(\mathbf{r} - \mathbf{r}_i) \delta(\hat{\mathbf{u}} - \hat{\mathbf{u}}_i) \mathbf{t}_i(\mathbf{r}^N, \hat{\mathbf{u}}^N) \right\rangle, \quad (12)$$

with $\hat{\mathbf{u}}^N = \hat{\mathbf{u}}_1 \dots \hat{\mathbf{u}}_N$ and $\hat{\mathbf{u}}_i = (\sin \theta_i \cos \varphi_i, \sin \theta_i \sin \varphi_i, \cos \theta_i)$ being the orientation of particle i . Here, θ_i and φ_i are the polar and azimuthal angles of particle i , respectively. The torque on particle i is \mathbf{t}_i , given by

$$\mathbf{t}_i(\mathbf{r}^N, \hat{\mathbf{u}}^N) = -\hat{\mathbf{R}}_i u(\mathbf{r}^N, \hat{\mathbf{u}}^N) - \hat{\mathbf{R}}_i V_{\text{ext}}(\mathbf{r}_i, \hat{\mathbf{u}}_i), \quad (13)$$

with $\hat{\mathbf{R}}_i = \hat{\mathbf{u}}_i \times \nabla_{\hat{\mathbf{u}}_i}$. Note that both the total interparticle potential $u(\mathbf{r}^N, \hat{\mathbf{u}}^N)$ and the external potential $V_{\text{ext}}(\mathbf{r}, \hat{\mathbf{u}})$ are allowed to carry a dependence on the particle orientation. The one-body torque density is therefore the sum of internal and external contributions

$$\mathbf{T}(\mathbf{r}, \hat{\mathbf{u}}) = \mathbf{T}_{\text{int}}(\mathbf{r}, \hat{\mathbf{u}}) + \mathbf{T}_{\text{ext}}(\mathbf{r}, \hat{\mathbf{u}}), \quad (14)$$

with

$$\mathbf{T}_{\text{int}}(\mathbf{r}, \hat{\mathbf{u}}) = - \left\langle \sum_i \delta(\mathbf{r} - \mathbf{r}_i) \delta(\hat{\mathbf{u}} - \hat{\mathbf{u}}_i) \hat{\mathbf{R}}_i u(\mathbf{r}^N, \hat{\mathbf{u}}^N) \right\rangle, \quad (15)$$

$$\mathbf{T}_{\text{ext}}(\mathbf{r}, \hat{\mathbf{u}}) = - \left\langle \sum_i \delta(\mathbf{r} - \mathbf{r}_i) \delta(\hat{\mathbf{u}} - \hat{\mathbf{u}}_i) \hat{\mathbf{R}}_i V_{\text{ext}}(\mathbf{r}_i, \hat{\mathbf{u}}_i) \right\rangle. \quad (16)$$

Using equation (8) the external contribution is simply

$$\mathbf{T}_{\text{ext}}(\mathbf{r}, \hat{\mathbf{u}}) = -\rho(\mathbf{r}, \hat{\mathbf{u}}) \hat{\mathbf{R}} V_{\text{ext}}(\mathbf{r}, \hat{\mathbf{u}}). \quad (17)$$

Further details regarding the derivation of the one-body torque density balance in equilibrium are given in appendix A.

In general, the force and the torque density balance equations are linked via the one-body density distribution. Here, we focus only on the role of the torque balance equation. For this we consider in what follows systems that are homogeneous in space and therefore cases in which the force balance equation does not play any role. In such systems $\rho(\mathbf{r}, \hat{\mathbf{u}}) = \rho_b f(\hat{\mathbf{u}})$, with ρ_b being the bulk density, and $f(\hat{\mathbf{u}})$ being the orientational distribution function. That is, $f(\hat{\mathbf{u}}) d\hat{\mathbf{u}}$ is the probability of finding a particle with orientation $\hat{\mathbf{u}}$ within a solid angle $d\hat{\mathbf{u}}$. The orientational distribution function is therefore normalized such that

$$\int d\hat{\mathbf{u}} f(\hat{\mathbf{u}}) = 1. \quad (18)$$

Using the traditional sampling method, the orientational distribution function can be sampled in computer simulations as

$$f(\hat{\mathbf{u}}) = \frac{1}{N} \left\langle \sum_i \delta(\hat{\mathbf{u}} - \hat{\mathbf{u}}_i) \right\rangle \quad (19)$$

$$= \frac{1}{N} \left\langle \sum_i \frac{1}{\sin \theta_i} \delta(\theta - \theta_i) \delta(\varphi - \varphi_i) \right\rangle. \quad (20)$$

The prefactor $1/N$ ensures the proper normalization of the orientational distribution function.

For spatially homogeneous systems, the one-body torque density balance equation (10) simplifies to

$$0 = -k_B T \rho_b \hat{\mathbf{R}} f(\hat{\mathbf{u}}) + \mathbf{T}(\hat{\mathbf{u}}). \quad (21)$$

Isolating the ideal gas term of equation (21) and integrating appropriately we obtain an expression for the orientational distribution function

$$f(\hat{\mathbf{u}}) = f_0 + (\rho_b k_B T)^{-1} \hat{\mathbf{R}}^{-1} \cdot \mathbf{T}(\hat{\mathbf{u}}). \quad (22)$$

Here, $\hat{\mathbf{R}}^{-1}$ is formally the inverse operator of $\hat{\mathbf{R}}$ and f_0 is an integration constant that ensures the proper normalization of the orientational distribution function. For both, two-dimensional systems and uniaxial three-dimensional systems, the inverse operator $\hat{\mathbf{R}}^{-1}$ reduces to a simple angular integral, see appendix B.

Obtaining the orientational distribution function via the one-body torque density balance has the advantage of treating the ideal gas part explicitly and hence, it avoids the corresponding fluctuations present in the counting method. The only source of statistical inaccuracies is in the sampled one-body torque density which is integrated over in order to obtain the orientational distribution function. As it turns out, this process reduces the statistical noise significantly.

3. Results

As a proof of concept, we test the validity of the torque sampling method with two different systems: (i) two-dimensional rectangular particles following Langevin dynamics and (ii) three-dimensional Gay–Berne particles following overdamped Brownian dynamics.

3.1. Two-dimensional system of rectangular particles

We consider a two-dimensional system of particles with rectangular shape undergoing Langevin dynamics (implemented according to [39]). The interaction between two particles is modeled via a purely repulsive potential $\phi(r) = \epsilon \left(\frac{\sigma}{r}\right)^{12}$. Here, r is the minimum distance between the two particles, σ is our length scale, and ϵ is our energy scale. The potential acts only between the two closest points (one on each particle) located on the particles' perimeter. The interparticle potential generates both an internal force and an internal torque. Details about

the calculation of the forces and the torques, as well as about the integration of the equations of motion are given in the appendix C.

We study a system of $N = 64$ rectangular particles with length $L/\sigma = 10$ and width $D/\sigma = 2$ in a square box of length 100σ and periodic boundary conditions. We set the temperature to $k_B T/\epsilon = 1$ and the integration time step to $\Delta t/\tau = 10^{-3}$ with $\tau = \sigma \sqrt{m/\epsilon}$ and m the mass of one particle. We sample every $10 \Delta t$. Since the system is very diluted, the equilibrium bulk state is isotropic. We induce orientational order via the external potential $V_{\text{ext}}(\varphi)/\epsilon = -0.5 \cos^2 \varphi$, with the angle φ measured anticlockwise with respect to the x -axis. A characteristic snapshot of the system is shown in figure 1.

We initialize the particles randomly and equilibrate the system with a simulation lasting $10^3 \tau$. After equilibration we sample the orientational distribution function via the counting and the torque sampling methods. The results are shown in figure 1 for three different sampling times: 10τ panel (a), $10^3 \tau$ panel (b), and $10^5 \tau$ panel (c). Due to the head-tail symmetry of the particles we represent the orientational distribution function in the interval $\varphi \in [0, \pi]$ only. Torque sampling provides at each time a profile which is closer to the 'true' equilibrium profile than the one provided by the counting method. The 'true' equilibrium profile $f_{\text{eq}}(\varphi)$ is defined here as the arithmetic mean of the profiles obtained with the counting and the torque sampling methods in a long simulation (total simulation time $10^7 \tau$). For all sampling times the statistical noise in the profiles using the counting method is significantly larger than that using the torque sampling method.

To quantify the accuracy of each method, we define an error parameter as the integrated square difference between the 'true' equilibrium profile and the sampled profile

$$\Delta = \int_0^\pi d\varphi [f_s(\varphi) - f_{\text{eq}}(\varphi)]^2. \quad (23)$$

Here, f_s is the profile sampled using the counting or the torque sampling methods. As can be seen in figure 1(e) the error of the torque sampling method is for all sampling times below the error of the counting method. For this particular bin size ($10^{-4} \pi$) one has to sample about ten times longer using the counting method than using the torque sampling method to reach the same accuracy.

In figure 1(f) we investigate the effect of varying the bin size at a fixed sampling time ($10^2 \tau$). By decreasing the bin size we increase the level of detail with which we resolve the orientational distribution function. However, decreasing the bin size obviously increases the number of bins and, as a direct consequence, the error in the traditional counting method also increases. Note that in the counting method the number of events that contribute to each bin is proportional to the bin size. On the other hand, the error in the torque sampling method is essentially independent of the bin size. The error does not increase by decreasing the bin size because the orientational distribution function is not determined by the local number of events. Instead, at each orientation the orientational distribution function is obtained via an orientational integral over the torque density. Analogous behavior occurs also when sampling

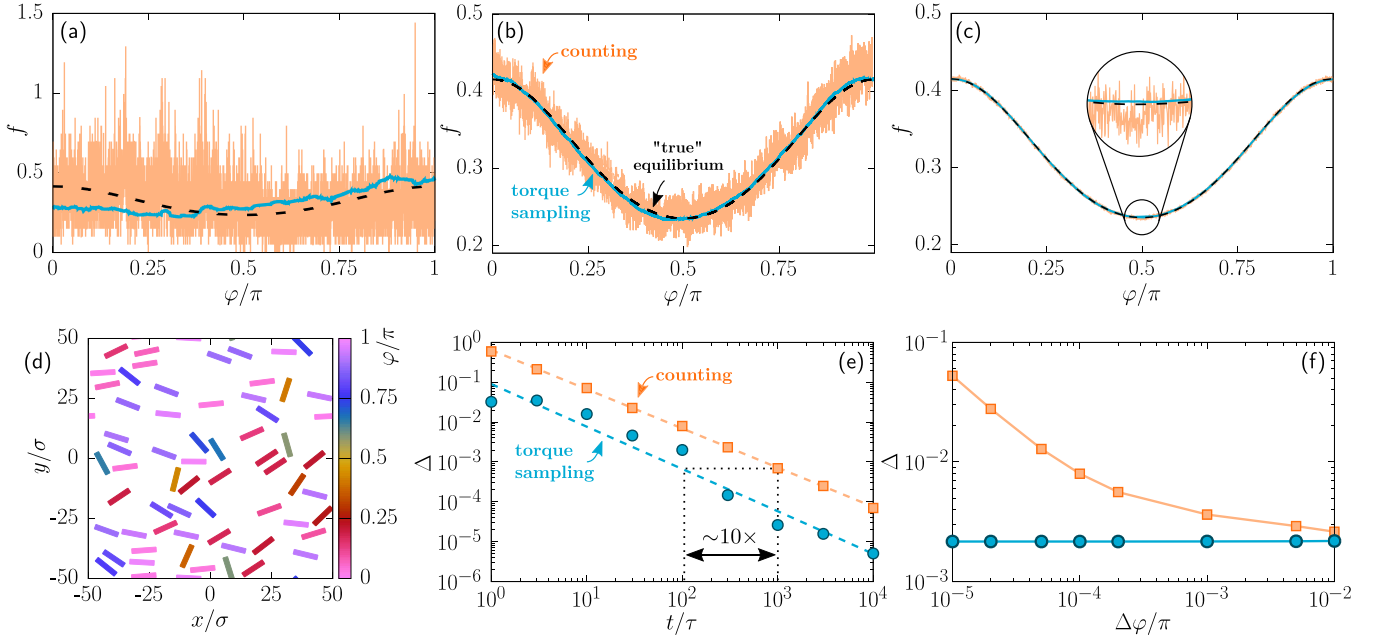


Figure 1. Orientational distribution function sampled with the counting method (orange) and the torque sampling method (blue) for three different sampling times: (a) 10τ , (b) $10^3\tau$, and (c) $10^5\tau$. The black dashed line is the ‘true’ equilibrium profile obtained by sampling over $10^7\tau$ and taking the arithmetic mean of the counting and the torque sampling methods. The bin size is $10^{-4}\pi$. The inset in (c) is a close view of the encircled region. (d) A characteristic snapshot of the system: $N = 64$ particles with rectangular shape subject to a weak external potential that orients the particles along the x -axis. A log – log plot of the error Δ as a function of the sampling time (e) and the error Δ as a function of the bin size (f) using the counting (orange squares) and the torque sampling (blue circles) method. In panel (e) the bin size is fixed to $10^{-4}\pi$ and the dashed lines are linear fits. In panel (f) the sampling time is fixed to $10^2\tau$ and the solid lines are guides for the eye.

the density profile using the force sampling method in systems with only translational degrees of freedom [1, 2, 14].

3.2. Tetratic order

Instead of sampling the complete, angle-resolved, orientational distribution function, it is common to sample only a reduced set of orientational order parameters (moments of the distribution). However, having access to the complete orientational distribution function can help to fully understand the type of order in the system. To illustrate this, we investigate a densely packed system of $N = 290$ particles with length $L/\sigma = 4$ and width $D/\sigma = 2$ in a square box of length 75σ . The equilibration time was $10^4\tau$. Due to their small length-to-width aspect ratio, the particles form in bulk at moderate densities a tetratic phase [40–42]. In the tetratic phase the particles are equally likely oriented along two directions perpendicular to each other. We add an external potential of the form $V_{\text{ext}}(\varphi)/\epsilon = -0.5 \sin^2(\varphi - \varphi_0)$ with $\varphi_0/\pi = 1/4$ and set the temperature to $k_B T/\epsilon = 1$. The external potential breaks the symmetry of the tetratic phase by favoring the orientation along the bottom-right to top-left diagonal of the square simulation box.

A snapshot of the system is shown in figure 2(a). The particles are colored according to their orientation. The resulting orientational distribution function is shown in figure 2(b) for a short sampling time of 1τ and in figure 2(c) for a sampling time of $10^5\tau$. Clearly more particles are aligned along the bottom-right to top-left diagonal ($\varphi/\pi = 0.75$) than along the

other diagonal ($\varphi/\pi = 0.25$) due to the external potential. In this example, the uniaxial order parameter or even the combination of both the uniaxial and the tetratic order parameters would not give enough information about the orientational order in the system.

The distributions sampled with torque sampling are always smoother than those sampled with the counting method. However, torque sampling sometimes produces artifacts for very short sampling times (of the order of 1τ), like the negative values around $\varphi/\pi = 0$ shown in figure 2(b). It might be possible to eliminate these artifacts by either using a combination of linear estimators [43] or the mapped averaging framework [10]. The artifacts are at least partially due to local angular currents originated by fluctuations that do not vanish (on average) due to the short sampling times. The occurrence of these angular currents is apparent when comparing the orientational distribution functions sampled at short, figure 2(b), and long, figure 2(c), sampling times (cf the evolution of the value of the orientational distribution functions at the peaks). For longer sampling times, figure 2(c), the angular current averages to zero for all orientations, and the distribution function calculated with torque sampling is free of artifacts. The profile obtained with torque sampling is more precise than that obtained via counting. Even at very long sampling times, e.g. $10^5\tau$ in 2(c), torque sampling outperforms counting. This is particularly clear when looking at the numerical angular derivative of the distribution function, see inset of figure 2(c).

Sampling the torques is not only useful to improve the sampling of the orientational distribution function but it also

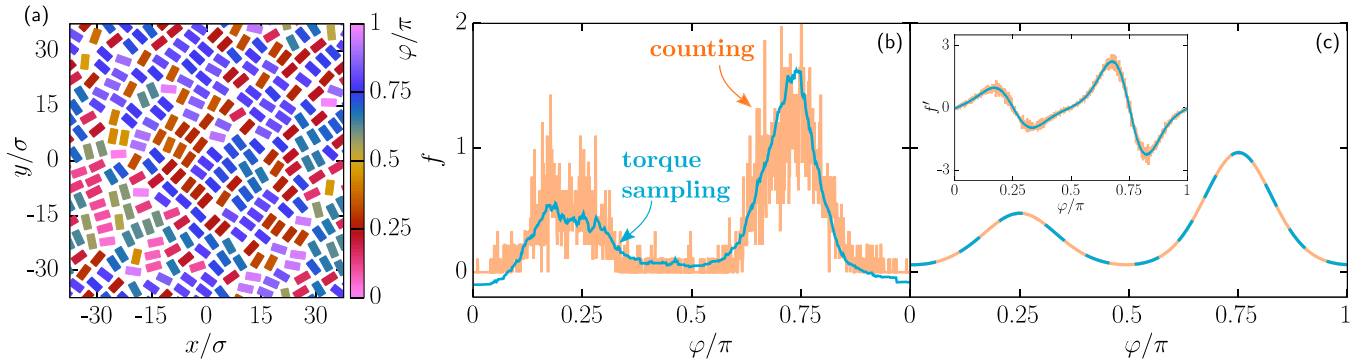


Figure 2. (a) Characteristic snapshot of a Langevin dynamics simulation of $N = 290$ rectangular particles in a square box of side length $L_{\text{box}}/\sigma = 75$ subject to an external potential that favors particle orientations along the bottom-right to top-left diagonal of the box. The particles are colored according to their orientation φ , measured with respect to the x -direction, see colorbar. Orientational distribution $f(\varphi)$ obtained via counting (orange lines) and torque sampling (blue lines) using a bin size of $10^{-3}\pi$ and for two sampling times: 1τ (b) and $10^5\tau$ (c). The inset in (c) shows the numerical angular derivative of the orientational distribution function $f'(\varphi) = df/d\varphi$ using the central difference.

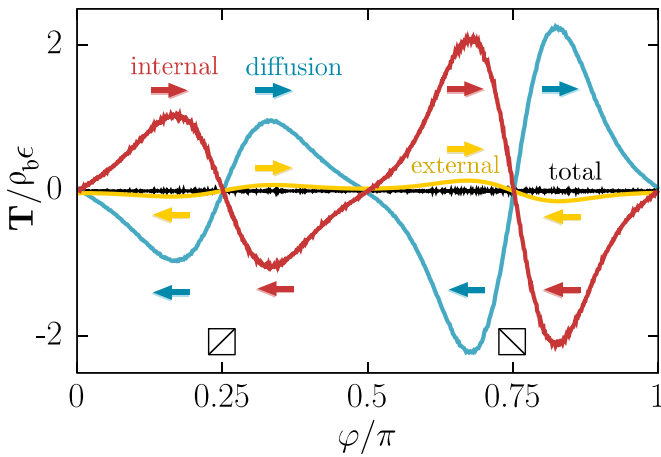


Figure 3. Components of the torque balance equation (normalized with the bulk density ρ_b) as a function of the angle in the tetratic configuration with an external field shown in figure 2. The torques point in the z -direction. Positive (negative) torques try to rotate the particles anticlockwise (clockwise), as indicated at selected angles by the color arrows. The external potential favors particle alignments along the bottom right to top left diagonal ($\varphi/\pi = 0.75$) of the simulation box. The bottom left to top right diagonal is located at $\varphi/\pi = 0.25$. Shown are the internal torque density (red), the diffusive torque density (blue), the external torque density (yellow), and the total torque density (black).

helps to understand the underlying physics. As an illustration, we show in figure 3 the components of the torque balance equation in the system with tetratic ordering and an external potential. The torques point along the z -direction. That is, positive (negative) torques tend to rotate the particles anticlockwise (clockwise), increasing (decreasing) therefore the value of φ . The diffusive torque (blue) always favors an isotropic state by trying to remove the inhomogeneities in the orientational distribution function. In the current configuration, the diffusive torque tries to orient the particles away from the diagonals. The behavior of the internal torque depends on several factors such as the interparticle potential, the temperature, and the density. In the current example,

the internal torque (red) favors tetratic ordering by trying to align the particles along the diagonals. The imposed external torque (yellow) tries to orient the particles along the bottom-right to top-left diagonal ($\varphi/\pi = 0.75$) and it also tries to orient the particles away from the other diagonal at $\varphi/\pi = 0.25$. As dictated by the torque balance equation, the sum of all three components (diffusive, internal, and external) vanishes since the system is in equilibrium, see figure 3 (black line).

3.3. Three-dimensional Gay-Berne fluid

We further test the method in a three-dimensional system of $N = 500$ Gay-Berne particles [44] confined in a box of size lengths $L_x/\sigma_0 = 10$, $L_y/\sigma_0 = 10$, and $L_z/\sigma_0 = 25$ with periodic boundary conditions. We use the parameters σ_0 and ϵ_0 of the Gay-Berne potential as our length and energy scales, respectively. All details about the interparticle potential are presented in appendix D. We set the length-to-width ratio of the particles to three. The particles follow overdamped Brownian dynamics. Time is measured in units of $\tau_0 = \gamma\sigma_0^2/\epsilon_0$, with γ the translational friction coefficient against the implicit solvent. The particles are subject to an external potential $V_{\text{ext}}(\theta)/\epsilon_0 = -0.5 \cos^2(\theta)$, with θ the polar angle. Hence, the external potential favors uniaxial alignment of the particles along the z -axis. The temperature is set to $k_B T/\epsilon_0 = 0.5$. For details regarding the implementation of the overdamped Brownian dynamics see appendix E.

The orientational distribution functions obtained via torque sampling and counting are shown for different sampling times in figure 4. Again, torque sampling provides profiles with better accuracy than counting. The differences between both methods are more acute for small values of the polar angle. The area of the bins on the unit sphere decreases close to the poles. Therefore, less events contribute to each bin, which produces large fluctuations of the profile obtained with the counting method. However, the profile obtained with torque sampling is unaffected by this problem since the error is independent of the bin size.

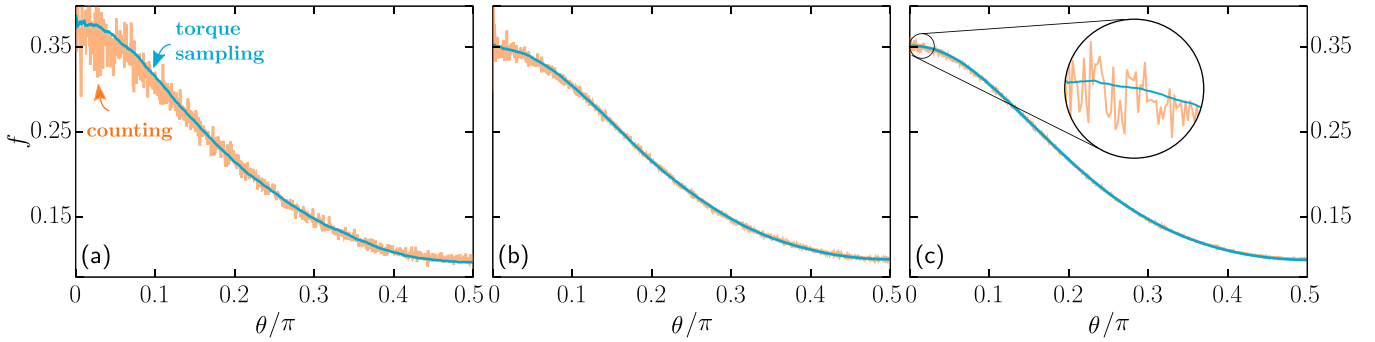


Figure 4. Overdamped Brownian dynamics simulation of $N = 500$ Gay–Berne particles in a three-dimensional box with periodic boundary conditions. Orientational distribution function f as a function of the polar angle θ obtained via counting (orange line) and torque sampling (blue line) using a bin size of $\Delta\theta = 10^{-3}\pi/2$ for different sampling times: $10^3\tau_0$ (a), $10^4\tau_0$ (b), and $10^5\tau_0$ (c). The inset in panel (c) is a close view of the region of small polar angles as indicated.

4. Conclusion

Reduced-variance estimators can be constructed using force sampling methods [14] to measure e.g. the density profile and the radial distribution function in computer simulations with better accuracy than the traditional counting method. We have shown here that in equilibrium systems of interacting anisotropic particles, reduced-variance estimators can be also constructed via torque sampling. By sampling the torques and using the exact torque balance equation of equilibrium many-body systems, we have developed a method to accurately reconstruct the orientational distribution function. Although the cases that we have studied here are arguably toy models, they do cover a wide range of situations, including two- vs three-dimensional systems, dilute vs dense systems, uniaxial vs tetratic orientational order, and Langevin vs overdamped Brownian dynamics. In all cases, torque sampling has outperformed counting.

Force sampling works equally well in Brownian dynamics, molecular dynamics, and Monte Carlo simulations [2]. Hence, although we have used here Brownian and Langevin dynamics, the torque sampling method is expected to also outperform the counting method in molecular dynamics and Monte Carlo simulations.

For small bin sizes, the statistical error for the counting method diverges, while the error for the torque sampling method is independent of the size of the bin. Hence, torque sampling can be particularly useful in cases where a large number of bins might be required such as for example when investigating biaxial nematics in three-dimensional systems [45–47].

We have restricted our study to cases without positional order such that force and torque balance equations are decoupled. There exist several fully inhomogeneous standard situations accessible in computer simulations [48–51] in which both the density profile and the orientational distribution profile depend on the position coordinate, i.e. $\rho(\mathbf{r}, \hat{\mathbf{u}}) = \rho(\mathbf{r})f(\mathbf{r}, \hat{\mathbf{u}})$. These include, among others, the formation of stable bulk phases with both positional and orientational order [52–54], confinement [55–57], sedimentation [58–60],

formation of topological defects [61–64], and nucleation [65] in liquid crystals. The force balance equation and the torque balance equation are then coupled and jointly determine the spatial and the orientational order of the system. The combination of force and torque sampling should be in such cases substantially better than counting which requires filling a multidimensional histogram in both positions and orientations.

The formulation of the torque sampling method presented here cannot be directly applied to hard particle models [66], in which forces arise only due to particle collisions. However, the mapped averaging framework is applicable in hard particle models [67]. Using the torque balance equation as input for the mapped averaging framework might result in reduced-variance estimators for the orientational distribution function. Exact sum rules involving the torques follow from the symmetries of the system [17] and might be also useful in the derivation of reduced-variance estimators in computer simulations of anisotropic particles.

The forces between individual colloidal particles are also accessible experimentally [68]. It might therefore be possible to use force and torque sampling methods for the determination of distribution functions in experimental systems.

Data availability statement

We will send the data upon reasonable request. The data cannot be made publicly available upon publication because they are not available in a format that is sufficiently accessible or reusable by other researchers. The data that support the findings of this study are available upon reasonable request from the authors.

Acknowledgment

We greatly acknowledge Enrique Velasco for helping us during the implementation of the Langevin dynamics simulation code, for suggesting the interaction potential between the rectangles, and for useful discussions. We also thank Daniel Borgis for useful discussions. This work is supported by

the German Research Foundation (DFG) via Project Number 447925252.

Appendix A. Force density and torque density balance equations

The force balance and torque balance equations in the context of density functional theory are shown e.g. in [69]. We sketch here the derivation of the force density and torque density balance equations for many-body systems of particles following overdamped Brownian dynamics. Let $\Psi(\mathbf{r}^N, \hat{\mathbf{u}}^N, t)$ be the many-body probability distribution function of an overdamped system. Then, statistical averages $\langle \cdot \rangle$ within the Fokker–Planck formalism can be computed as

$$\langle \cdot \rangle = \int d\mathbf{r}^N \int d\hat{\mathbf{u}}^N \cdot \Psi(\mathbf{r}^N, \hat{\mathbf{u}}^N, t), \quad (\text{A1})$$

where the integrals cover the complete space of configurations. The velocity \mathbf{v}_i and the angular velocity $\boldsymbol{\omega}_i$ of particle i are given by

$$\gamma \mathbf{v}_i = -k_B T \nabla_i \ln \Psi - \nabla_i u(\mathbf{r}^N, \hat{\mathbf{u}}^N) + \mathbf{f}_{\text{ext}}(\mathbf{r}_i, \hat{\mathbf{u}}_i, t), \quad (\text{A2})$$

$$\gamma_r \boldsymbol{\omega}_i = -k_B T \hat{\mathbf{R}}_i \ln \Psi - \hat{\mathbf{R}}_i u(\mathbf{r}^N, \hat{\mathbf{u}}^N) + \boldsymbol{\tau}_{\text{ext}}(\mathbf{r}_i, \hat{\mathbf{u}}_i, t). \quad (\text{A3})$$

Here, γ and γ_r are the translational and rotational friction constants against the implicit solvent, respectively, and $\boldsymbol{\tau}_{\text{ext}}$ is an external torque field. The current \mathbf{J} and the angular current \mathbf{J}_ω are

$$\mathbf{J}(\mathbf{r}, \hat{\mathbf{u}}, t) = \left\langle \sum_i \mathbf{v}_i \delta(\mathbf{r} - \mathbf{r}_i) \delta(\hat{\mathbf{u}} - \hat{\mathbf{u}}_i) \right\rangle, \quad (\text{A4})$$

$$\mathbf{J}_\omega(\mathbf{r}, \hat{\mathbf{u}}, t) = \left\langle \sum_i \boldsymbol{\omega}_i \delta(\mathbf{r} - \mathbf{r}_i) \delta(\hat{\mathbf{u}} - \hat{\mathbf{u}}_i) \right\rangle. \quad (\text{A5})$$

Multiplying equations (A2) and (A3) by $\delta(\mathbf{r} - \mathbf{r}_i) \delta(\hat{\mathbf{u}} - \hat{\mathbf{u}}_i)$, summing over all particles i , and applying the average in equation (A1) yields directly

$$\gamma \mathbf{J}(\mathbf{r}, \hat{\mathbf{u}}, t) = -k_B T \nabla \rho(\mathbf{r}, \hat{\mathbf{u}}, t) + \mathbf{F}(\mathbf{r}, \hat{\mathbf{u}}, t), \quad (\text{A6})$$

$$\gamma_r \mathbf{J}_\omega(\mathbf{r}, \hat{\mathbf{u}}, t) = -k_B T \hat{\mathbf{R}} \rho(\mathbf{r}, \hat{\mathbf{u}}, t) + \mathbf{T}(\mathbf{r}, \hat{\mathbf{u}}, t). \quad (\text{A7})$$

The above force (A6) and torque (A7) density balance equations hold in full non-equilibrium situations. In equilibrium, the equations simplify further since: (i) the time dependence drops from the density profile, the force density \mathbf{F} , and the torque density \mathbf{T} , (ii) the external force and the external torque are conservative, and (iii) both \mathbf{J} and \mathbf{J}_ω vanish. Hence, in equilibrium equations (A6) and (A7) reduce to equations (9) and (10), respectively.

The equilibrium force and torque balance equations do not change if the particles obey Langevin or molecular dynamics instead of overdamped Brownian dynamics but the derivation is slightly different. To derive the force and the torque balance

equations in Langevin dynamics or molecular dynamics, one needs to time differentiate the current and the angular current, both of which also vanish in equilibrium:

$$\dot{\mathbf{J}}(\mathbf{r}, \hat{\mathbf{u}}) = \frac{d}{dt} \left\langle \sum_i \mathbf{v}_i \delta(\mathbf{r} - \mathbf{r}_i) \delta(\hat{\mathbf{u}} - \hat{\mathbf{u}}_i) \right\rangle = 0, \quad (\text{A8})$$

$$\dot{\mathbf{J}}_\omega(\mathbf{r}, \hat{\mathbf{u}}) = \frac{d}{dt} \left\langle \sum_i \boldsymbol{\omega}_i \delta(\mathbf{r} - \mathbf{r}_i) \delta(\hat{\mathbf{u}} - \hat{\mathbf{u}}_i) \right\rangle = 0. \quad (\text{A9})$$

Here, the average $\langle \cdot \rangle$ is again performed over the complete configuration space which in molecular dynamics includes integrals over the linear and angular momenta in addition to those over the positions and the orientations of the particles. Incorporating the time derivative inside the averages in equations (A8) and (A9) results in the force and torque balance equations. In equilibrium, the integrals over the linear and the angular momenta can be carried out explicitly.

Appendix B. Torque sampling for single angular dependencies

We derive here the expressions for the orientational distribution function as an angular integral over the torques in the system. The rotational operator can be written as

$$\hat{\mathbf{R}} = \hat{\mathbf{u}} \times \nabla_{\hat{\mathbf{u}}} = \mathbf{e}_\varphi \frac{\partial}{\partial \theta} - \mathbf{e}_\theta \frac{1}{\sin \theta} \frac{\partial}{\partial \varphi}, \quad (\text{B1})$$

with \mathbf{e}_φ and \mathbf{e}_θ being the unit vectors on the unit sphere in the azimuthal and in the polar directions, respectively.

B.1. Two-dimensional system

In the two-dimensional system of rectangular particles, the orientational distribution function depends only on the azimuthal angle $f = f(\varphi)$. Hence, using $\theta = \pi/2$, the rotational operator, equation (B1), simplifies to $\hat{\mathbf{R}} = \mathbf{e}_z \partial / \partial \varphi$, and the torque density balance equation (21) is then

$$0 = -k_B T \rho_b \mathbf{e}_z \frac{\partial f(\varphi)}{\partial \varphi} + \mathbf{T}(\varphi), \quad (\text{B2})$$

with \mathbf{T} also directed along the \mathbf{e}_z direction. The orientational distribution function can be then reconstructed with the sampled torques via

$$f(\varphi) = f_0 + \frac{1}{k_B T \rho_b} \int d\varphi \mathbf{T}(\varphi) \cdot \mathbf{e}_z, \quad (\text{B3})$$

with f_0 a normalization constant such that $\int d\varphi f(\varphi) = 1$.

Using equation (17) it follows that

$$\mathbf{T}_{\text{ext}}(\varphi) = -\rho_b f(\varphi) \frac{\partial V_{\text{ext}}(\varphi)}{\partial \varphi} \mathbf{e}_z, \quad (\text{B4})$$

which inserted in equation (B2) can be used to first solve the homogeneous equation analytically and then treat the

internal torque density as an inhomogeneity. We find that both approaches give similar results.

B.2. Three-dimensional uniaxial system

We consider now the three dimensional system of Gay–Berne particles with a uniaxial distribution function, i.e. $f = f(\theta)$ and an external potential $V_{\text{ext}}(\theta)$ that depends also only on the polar angle. Hence the rotational operator, equation (B1), is $\hat{\mathbf{R}} = \mathbf{e}_\varphi \partial / \partial \theta$, which inserted in the torque density balance equation yields

$$0 = -k_B T \rho_b \frac{\partial f(\theta)}{\partial \theta} \mathbf{e}_\varphi + \mathbf{T}, \quad (\text{B5})$$

where $\mathbf{T} = (T_{\text{int}}(\theta) + T_{\text{ext}}(\theta)) \mathbf{e}_\varphi$, from which we obtain

$$f(\theta) = f_0 + \frac{1}{k_B T \rho_b} \int d\theta T(\theta). \quad (\text{B6})$$

The normalization constant f_0 is here such that $\int d\hat{\mathbf{u}} f(\theta) = 1$. Again, it is possible to first analytically solve the homogeneous differential equation of (B5) by writing the external torques explicitly

$$\mathbf{T}_{\text{ext}}(\theta) = -\rho_b f(\theta) \frac{\partial V_{\text{ext}}(\theta)}{\partial \theta} \mathbf{e}_\varphi, \quad (\text{B7})$$

and treat the internal part as the inhomogeneous part.

Appendix C. Interparticle interaction between two rectangles and Langevin dynamics

Two rectangles interact via a purely repulsive pair-potential of the form

$$\phi(r) = \epsilon \left(\frac{\sigma}{r} \right)^{12}, \quad (\text{C1})$$

with r being the minimum distance between the two rectangles. Depending on the positions and the orientations of the particles, there are two possible scenarios, see figure 5: (i) the minimum distance is between a corner of one particle and a point located on an edge of the other particle, or (ii) the minimum distance is between two corners. We introduce a cut-off distance of $r_c = 2L + 3\sigma$ between the centers of mass of the particles. The potential generates a contact force between the two particles. The effect of the contact force between the two closest points is equivalent to apply both a force and a torque on the center of masses of the particles.

The force acting on the center of mass of particle i due to particle j is given by

$$\mathbf{f}_{ij} = -\frac{\partial \phi}{\partial r} \frac{\mathbf{r}}{r} = -\mathbf{f}_{ji}, \quad (\text{C2})$$

and the torque acting on particle i due to particle j is given by

$$\mathbf{t}_{ij} = -\hat{\mathbf{u}}_i \times \frac{\partial \phi}{\partial \hat{\mathbf{u}}_i} = \mathbf{r}_i^c \times \mathbf{f}_{ij}. \quad (\text{C3})$$

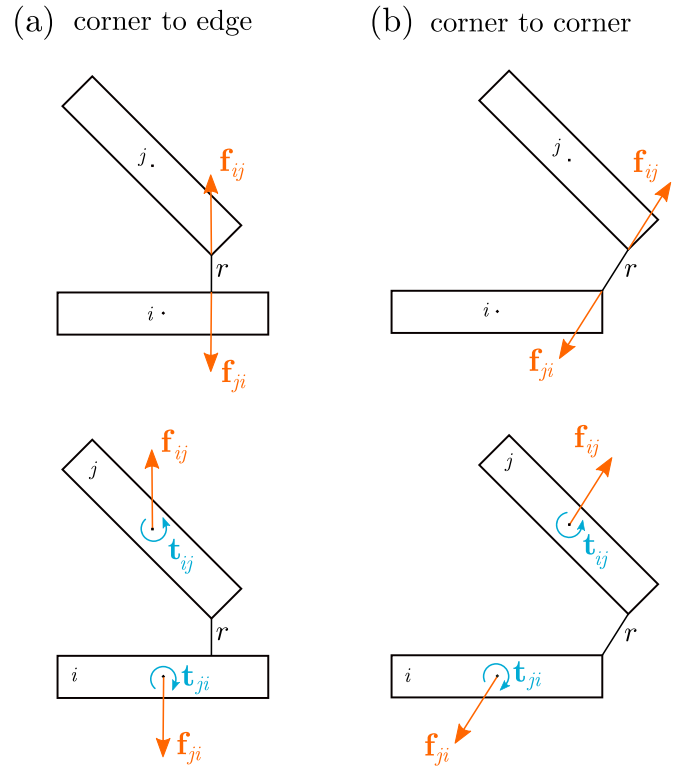


Figure 5. The minimum distance between two rectangles r is either between a corner and an edge (a) or between two corners (b). The effect of the contact force acting on the points of minimum distance (top panels) is equivalent to the effect of the same force and a torque acting on the center of mass (bottom panels).

Here, \mathbf{r} is the vector joining the closest points between particles i and j and $\hat{\mathbf{u}}_i$ denotes the orientation of particle i . The vector \mathbf{r}_i^c joins the center of mass of particle i with the point of application of the force.

To calculate the minimum distance between two particles we calculate all possible corner-corner and corner-edge distances and select the minimum of all of them.

Verlet-type integration algorithm for Langevin dynamics.

We calculate the trajectories following the integration scheme for Langevin dynamics presented in [39] for isotropic particles. The translational equations of motion for particle i are given by

$$\dot{\mathbf{r}}_i = \mathbf{v}_i, \quad (\text{C4})$$

$$m \dot{\mathbf{v}}_i = \mathbf{f}_i - \gamma \mathbf{v}_i + \mathbf{f}_i^{\text{rand}}. \quad (\text{C5})$$

Here \mathbf{r}_i , \mathbf{v}_i , and \mathbf{f}_i are the position, the velocity, and the total force (internal plus external) of particle i (the overdot indicates the time derivative), m is the mass of one particle, γ is the translational friction coefficient, and $\mathbf{f}_i^{\text{rand}}$ is a delta-correlated Gaussian random force (described in detail in appendix E). These equations are integrated with the following Verlet-type scheme [39]

$$\mathbf{r}_i(t + \Delta t) = \mathbf{r}_i(t) + b\Delta t \mathbf{v}_i(t) + \frac{b\Delta t^2}{2m} [\mathbf{f}_i(t) + \mathbf{f}_i^{\text{rand}}(t + \Delta t)], \quad (\text{C6})$$

$$\mathbf{v}_i(t + \Delta t) = a\mathbf{v}_i(t) + \frac{\Delta t}{2m} [a\mathbf{f}_i(t) + \mathbf{f}_i(t + \Delta t)] + \frac{b\Delta t}{m} \mathbf{f}_i^{\text{rand}}(t + \Delta t), \quad (\text{C7})$$

with the parameters $a = (1 - \alpha)/(1 + \alpha)$, $b = 1/(1 + \alpha)$ and $\alpha = \gamma\Delta t/(2m)$.

The equations of motion for the angular degrees of freedom in our two-dimensional system of rectangular particles following Langevin dynamics are given by

$$\dot{\varphi}_i = \omega_i, \quad (\text{C8})$$

$$I\dot{\omega}_i = t_i - \gamma_r\omega_i + t_i^{\text{rand}}. \quad (\text{C9})$$

Here φ_i , ω_i , and t_i are the azimuthal angle, the angular velocity, and the torque (internal and external) of particle i , γ_r is the rotational friction coefficient, t_i^{rand} is a random torque (see details in appendix E), and $I = m(L^2 + D^2)/12$ is the moment of inertia around the axis normal to the particle that passes through the center of mass (the particles are assumed to have a homogeneous mass distribution). The torques and the angular velocity point along the z -direction (normal to the particles). Equations (C8) and (C9) have the same mathematical structure as equations (C4) and (C5). We therefore apply the same integration scheme as for the positional degrees of freedom, replacing the mass m by the moment of inertia I and the translational friction γ by the rotational friction γ_r . For simplicity we set $\gamma_r = \gamma\sigma^2$. The value of the friction constants does not affect the equilibrium properties.

Appendix D. Gay–Berne potential

We use the same implementation of the Gay–Berne potential as that in [44]. The interaction potential between two particles is

$$\phi(\mathbf{r}, \hat{\mathbf{u}}_1, \hat{\mathbf{u}}_2) = 4\epsilon(\mathbf{r}, \hat{\mathbf{u}}_1, \hat{\mathbf{u}}_2) \left[\left(\frac{\sigma_0}{r - \sigma(\mathbf{r}, \hat{\mathbf{u}}_1, \hat{\mathbf{u}}_2) + \sigma_0} \right)^{12} - \left(\frac{\sigma_0}{r - \sigma(\mathbf{r}, \hat{\mathbf{u}}_1, \hat{\mathbf{u}}_2) + \sigma_0} \right)^6 \right]. \quad (\text{D1})$$

with \mathbf{r} the vector joining the centers of mass of the particles, $\hat{\mathbf{u}}_1$ and $\hat{\mathbf{u}}_2$ unit vectors along the long axes of the particles, and the functions $\epsilon(\mathbf{r}, \hat{\mathbf{u}}_1, \hat{\mathbf{u}}_2)$ and $\sigma(\mathbf{r}, \hat{\mathbf{u}}_1, \hat{\mathbf{u}}_2)$ are given by

$$\epsilon(\mathbf{r}, \hat{\mathbf{u}}_1, \hat{\mathbf{u}}_2) = \epsilon_0 (\xi_+ \xi_-)^{-1/2} (\sigma^*(\chi'))^2, \quad (\text{D2})$$

$$\sigma(\mathbf{r}, \hat{\mathbf{u}}_1, \hat{\mathbf{u}}_2) = \sigma_0 (\sigma^*(\chi))^{-1/2}, \quad (\text{D3})$$

with

$$\chi = \frac{l^2 - 1}{l^2 + 1}, \quad (\text{D4})$$

$$\chi' = \frac{\sqrt{d} - 1}{\sqrt{d} + 1}, \quad (\text{D5})$$

$$\sigma^*(\xi) = 1 - \frac{\xi}{2} \left[\frac{(r_u^+)^2}{\xi_+} + \frac{(r_u^-)^2}{\xi_-} \right], \quad (\text{D6})$$

$$\xi_{\pm} = 1 \pm \xi \hat{\mathbf{u}}_1 \cdot \hat{\mathbf{u}}_2, \quad (\text{D7})$$

$$r_u^{\pm} = \mathbf{r} \cdot \hat{\mathbf{u}}_1 \pm \mathbf{r} \cdot \hat{\mathbf{u}}_2. \quad (\text{D8})$$

Here, ξ takes the values χ or χ' and the parameters ϵ_0 and σ_0 set the energy and the length scales. We select a length-to-width ratio $l = 3$, and set the energy ratio between the side-by-side and the tip-to-tip configurations to $d = 5$.

Appendix E. Overdamped Brownian dynamics with orientational degrees of freedom

The equations of motion of particle i are

$$\gamma \mathbf{v}_i = \mathbf{f}_i^{\text{rand}}(t) - \nabla_i u(\mathbf{r}^N, \hat{\mathbf{u}}^N) - \nabla_i V_{\text{ext}}(\mathbf{r}_i, \hat{\mathbf{u}}_i), \quad (\text{E1})$$

$$\gamma_r \boldsymbol{\omega}_i = \mathbf{t}_i^{\text{rand}}(t) - \hat{\mathbf{R}}_i u(\mathbf{r}^N, \hat{\mathbf{u}}^N) - \hat{\mathbf{R}}_i V_{\text{ext}}(\mathbf{r}_i, \hat{\mathbf{u}}_i), \quad (\text{E2})$$

Here, $\mathbf{f}_i^{\text{rand}}$ and $\mathbf{t}_i^{\text{rand}}$ are delta-correlated Gaussian random forces and torques, respectively, with zero means and variances

$$\langle \mathbf{f}_i^{\text{rand}}(t) \mathbf{f}_k^{\text{rand}}(t') \rangle = 2k_B T \gamma \mathbb{1} \delta_{ik} \delta(t - t'), \quad (\text{E3})$$

$$\langle \mathbf{t}_i^{\text{rand}}(t) \mathbf{t}_k^{\text{rand}}(t') \rangle = 2k_B T \gamma_r (\mathbb{1} - \hat{\mathbf{u}} \hat{\mathbf{u}}) \delta_{ik} \delta(t - t'). \quad (\text{E4})$$

Here, the angles denote an average of the noise, $\mathbb{1}$ is the identity matrix, $\hat{\mathbf{u}} \hat{\mathbf{u}}$ indicates the dyadic product, and δ_{ik} is the Kronecker delta. The angular velocity is

$$\boldsymbol{\omega}_i = \hat{\mathbf{u}}_i \times \dot{\hat{\mathbf{u}}}_i. \quad (\text{E5})$$

Using the vector triple product and the fact that $\hat{\mathbf{u}}_i \cdot \dot{\hat{\mathbf{u}}}_i = 0$ due to $\hat{\mathbf{u}}_i \cdot \hat{\mathbf{u}}_i = 1$, it follows directly that

$$\dot{\hat{\mathbf{u}}}_i = \boldsymbol{\omega}_i \times \hat{\mathbf{u}}_i. \quad (\text{E6})$$

Hence, the equations of motion can be integrated in time using the standard Euler algorithm via

$$\mathbf{r}_i(t + \Delta t) = \mathbf{r}_i(t) + \frac{\Delta t}{\gamma} [-\nabla_i u(\mathbf{r}^N, \hat{\mathbf{u}}^N) - \nabla_i V_{\text{ext}}(\mathbf{r}_i, \hat{\mathbf{u}}_i)] + \boldsymbol{\eta}_i(t) \quad (\text{E7})$$

$$\hat{\mathbf{u}}_i(t + \Delta t) = \hat{\mathbf{u}}_i(t) + \frac{\Delta t}{\gamma_r} [-\hat{\mathbf{R}}_i u(\mathbf{r}^N, \hat{\mathbf{u}}^N) - \hat{\mathbf{R}}_i V_{\text{ext}}(\mathbf{r}_i, \hat{\mathbf{u}}_i)] \times \hat{\mathbf{u}}_i(t) + \boldsymbol{\Gamma}_i(t). \quad (\text{E8})$$

Here, $\boldsymbol{\eta}_i$ is a Gaussian random displacement with zero mean and standard deviation $\sqrt{2k_B T \Delta t / \gamma}$, and

$$\boldsymbol{\Gamma}_i = \sqrt{\frac{2k_B T \Delta t}{\gamma_r}} (U_i^1 \hat{\mathbf{w}}_i^1 + U_i^2 \hat{\mathbf{w}}_i^2) \quad (\text{E9})$$

is a random rotation. Here, U_i^1 and U_i^2 are Gaussian random numbers with zero mean and unit width, and $\hat{\mathbf{w}}_i^1 = \mathbf{e}_x \times \hat{\mathbf{u}}_i / |\mathbf{e}_x \times \hat{\mathbf{u}}_i|$, $\hat{\mathbf{w}}_i^2 = \hat{\mathbf{w}}_i^1 \times \hat{\mathbf{u}}_i$, and $\hat{\mathbf{u}}_i$ are orthonormal to each other. We renormalize $\hat{\mathbf{u}}_i$ after each time step such that it remains a unit vector.

We arbitrarily relate the rotational friction coefficient to the translational friction coefficient via $\gamma_r = \gamma \sigma^2$. Also, we use a single translational friction coefficient γ for displacements parallel and perpendicular to the main axis of the particle. The values of the friction coefficients do not play any role in the equilibrium distribution functions. The Euler integration time step is $\Delta t = 10^{-4} \tau$ and we sample every $10^{-2} \tau$. Although we have used here a simple Euler scheme to integrate the equations of motion, it would be useful to extend the recently developed adaptive Brownian dynamics [70] algorithm to systems with orientational degrees of freedom to speed up the simulations.

ORCID iDs

Matthias Schmidt  <https://orcid.org/0000-0002-5015-2972>

Daniel de las Heras  <https://orcid.org/0000-0003-3219-0518>

References

- [1] Borgis D, Assaraf R, Rotenberg B and Vuilleumier R 2013 Computation of pair distribution functions and three-dimensional densities with a reduced variance principle *Mol. Phys.* **111** 3486
- [2] de las Heras D and Schmidt M 2018 Better than counting: density profiles from force sampling *Phys. Rev. Lett.* **120** 218001
- [3] Coles S W, Borgis D, Vuilleumier R and Rotenberg B 2019 Computing three-dimensional densities from force densities improves statistical efficiency *J. Chem. Phys.* **151** 064124
- [4] Sutherland B J, Moore W H D and Manolopoulos D E 2021 Nuclear quantum effects in thermal conductivity from centroid molecular dynamics *J. Chem. Phys.* **154** 174104
- [5] Simon J-M, Krüger P, Schnell S K, Vlugt T J H, Kjølstrup S and Bedeaux D 2022 Kirkwood–Buff integrals: from fluctuations in finite volumes to the thermodynamic limit *J. Chem. Phys.* **157** 130901
- [6] Mangaud E and Rotenberg B 2020 Sampling mobility profiles of confined fluids with equilibrium molecular dynamics simulations *J. Chem. Phys.* **153** 044125
- [7] Moustafa S G, Schultz A J and Kofke D A 2015 Very fast averaging of thermal properties of crystals by molecular simulation *Phys. Rev. E* **92** 043303
- [8] Schultz A J, Moustafa S G, Lin W, Weinstein S J and Kofke D A 2016 Reformulation of ensemble averages via coordinate mapping *J. Chem. Theory Comput.* **12** 1491
- [9] Schultz A J and Kofke D A 2019 Alternatives to conventional ensemble averages for thermodynamic properties *Curr. Opin. Chem. Eng.* **23** 70
- [10] Purohit A, Schultz A J and Kofke D A 2019 Force-sampling methods for density distributions as instances of mapped averaging *Mol. Phys.* **117** 2822
- [11] Moustafa S G, Schultz A J and Kofke D A 2022 Reformulation of expressions for thermoelastic properties of crystals using harmonic mapping *Phys. Rev. B* **106** 104105
- [12] Assaraf R and Caffarel M 1999 Zero-variance principle for Monte Carlo algorithms *Phys. Rev. Lett.* **83** 4682
- [13] Assaraf R, Caffarel M and Scemama A 2007 Improved Monte Carlo estimators for the one-body density *Phys. Rev. E* **75** 035701
- [14] Rotenberg B 2020 Use the force! reduced variance estimators for densities, radial distribution functions and local mobilities in molecular simulations *J. Chem. Phys.* **153** 150902
- [15] Tschopp S M, Sammüller F, Hermann S, Schmidt M and Brader J M 2022 Force density functional theory in- and out-of-equilibrium *Phys. Rev. E* **106** 014115
- [16] Sammüller F, Hermann S and Matthias H S 2023 Comparative study of force-based classical density functional theory *Phys. Rev. E* **107** 034109
- [17] Hermann S and Schmidt M 2021 Noether's theorem in statistical mechanics *Commun. Phys.* **4** 176
- [18] Hermann S and Schmidt M 2022a Variance of fluctuations from Noether invariance *Commun. Phys.* **5** 276
- [19] Hermann S and Schmidt M 2022b Force balance in thermal quantum many-body systems from Noether's theorem *J. Phys. A: Math. Theor.* **55** 464003
- [20] Krekeler C, Agarwal A, Junghans C, Praprotnik M and Delle Site L 2018 Adaptive resolution molecular dynamics technique: down to the essential *J. Chem. Phys.* **149** 024104
- [21] Praprotnik M, Delle Site L and Kremer K 2005 Adaptive resolution molecular-dynamics simulation: changing the degrees of freedom on the fly *J. Chem. Phys.* **123** 224106
- [22] Potestio R, Español P, Delgado-Buscalioni R, Everaers R, Kremer K and Donadio D 2013 Monte Carlo adaptive resolution simulation of multicomponent molecular liquids *Phys. Rev. Lett.* **111** 060601
- [23] Potestio R, Fritsch S, Español P, Delgado-Buscalioni R, Kremer K, Everaers R and Donadio D 2013 Hamiltonian adaptive resolution simulation for molecular liquids *Phys. Rev. Lett.* **110** 108301
- [24] Kirkwood J G and Buff F P 1951 The statistical mechanical theory of solutions. I *J. Chem. Phys.* **19** 774
- [25] Dawass N, Krüger P, Schnell S K, Moulton O A, Economou I G, Vlugt T J H and Simon J-M 2020 Kirkwood–Buff integrals using molecular simulation: estimation of surface effects *Nanomaterials* **10** 771
- [26] Evans R 1979 The nature of the liquid–vapour interface and other topics in the statistical mechanics of non-uniform, classical fluids *Adv. Phys.* **28** 143
- [27] Marconi U M B and Tarazona P 1999 Dynamic density functional theory of fluids *J. Chem. Phys.* **110** 8032
- [28] Archer A J and Evans R 2004 Dynamical density functional theory and its application to spinodal decomposition *J. Chem. Phys.* **121** 4246
- [29] Español P and Löwen H 2009 Derivation of dynamical density functional theory using the projection operator technique *J. Chem. Phys.* **131** 244101

- [30] te Vrugt M, Löwen H and Wittkowski R 2020 Classical dynamical density functional theory: from fundamentals to applications *Adv. Phys.* **69** 121
- [31] Tschopp S M and Brader J M 2022 First-principles superadiabatic theory for the dynamics of inhomogeneous fluids *J. Chem. Phys.* **157** 234108
- [32] Schmidt M and Brader J M 2013 Power functional theory for Brownian dynamics *J. Chem. Phys.* **138** 214101
- [33] de las Heras D and Schmidt M 2020 Flow and structure in nonequilibrium Brownian many-body systems *Phys. Rev. Lett.* **125** 018001
- [34] Schmidt M 2022 Power functional theory for many-body dynamics *Rev. Mod. Phys.* **94** 015007
- [35] de las Heras D, Renner J and Schmidt M 2019 Custom flow in overdamped Brownian dynamics *Phys. Rev. E* **99** 023306
- [36] Renner J, Schmidt M and de las Heras D 2021 Custom flow in molecular dynamics *Phys. Rev. Res.* **3** 013281
- [37] Renner J, Schmidt M and de las Heras D 2022 Shear and bulk acceleration viscosities in simple fluids *Phys. Rev. Lett.* **128** 094502
- [38] Hansen J-P and McDonald I R 2013 *Theory of Simple Liquids With Applications to Soft Matter* (London: Elsevier Science & Technology Books)
- [39] Grønbech-Jensen N and Farago O 2013 A simple and effective Verlet-type algorithm for simulating Langevin dynamics *Mol. Phys.* **111** 983
- [40] Martínez-Ratón Y, Velasco E and Mederos L 2005 Effect of particle geometry on phase transitions in two-dimensional liquid crystals *J. Chem. Phys.* **122** 064903
- [41] Martínez-Ratón Y and Velasco E 2009 Enhanced stability of the tetragonal phase due to clustering *Phys. Rev. E* **79** 011711
- [42] González-Pinto M, Renner J, de las Heras D, Martínez-Ratón Y and Velasco E 2019 Defects in vertically vibrated monolayers of cylinders *New J. Phys.* **21** 033002
- [43] Coles S W, Mangaud E, Frenkel D and Rotenberg B 2021 Reduced variance analysis of molecular dynamics simulations by linear combination of estimators *J. Chem. Phys.* **154** 191101
- [44] Gay J G and Berne B J 1981 Modification of the overlap potential to mimic a linear site-site potential *J. Chem. Phys.* **74** 3316
- [45] Allen M P 1990 Computer simulation of a biaxial liquid crystal *Liq. Cryst.* **8** 499
- [46] Berardi R, Muccioli L, Orlandi S, Ricci M and Zannoni C 2008 Computer simulations of biaxial nematics *J. Phys.: Condens. Matter* **20** 463101
- [47] Berardi R, Lintuvuori J S, Wilson M R and Zannoni C 2011 Phase diagram of the uniaxial and biaxial soft-core Gay-Berne model *J. Chem. Phys.* **135** 134119
- [48] Wilson M R 2005 Progress in computer simulations of liquid crystals *Int. Rev. Phys. Chem.* **24** 421
- [49] Care C M and Cleaver D J 2005 Computer simulation of liquid crystals *Rep. Prog. Phys.* **68** 2665
- [50] Allen M P 2019 Molecular simulation of liquid crystals *Mol. Phys.* **117** 2391
- [51] Zannoni C 2022 *Liquid Crystals and Their Computer Simulations* (Cambridge: Cambridge University Press)
- [52] Veerman J A C and Frenkel D 1990 Phase diagram of a system of hard spherocylinders by computer simulation *Phys. Rev. A* **41** 3237
- [53] McGrother S C, Williamson D C and Jackson G 1996 A re-examination of the phase diagram of hard spherocylinders *J. Chem. Phys.* **104** 6755
- [54] Chiappini M, Drwenski T, van Roij R and Dijkstra M 2019 Biaxial, twist-bend and splay-bend nematic phases of banana-shaped particles revealed by lifting the “smectic blanket” *Phys. Rev. Lett.* **123** 068001
- [55] Wall G D and Cleaver D J 1997 Computer simulation studies of confined liquid-crystal films *Phys. Rev. E* **56** 4306
- [56] Trukhina Y and Schilling T 2008 Computer simulation study of a liquid crystal confined to a spherical cavity *Phys. Rev. E* **77** 011701
- [57] Geigenfeind T, Rosenzweig S, Schmidt M and de las Heras D 2015 Confinement of two-dimensional rods in slit pores and square cavities *J. Chem. Phys.* **142** 174701
- [58] Savenko S V and Dijkstra M 2004 Sedimentation and multiphase equilibria in suspensions of colloidal hard rods *Phys. Rev. E* **70** 051401
- [59] van der Beek D, Schilling T and Lekkerkerker H N W 2004 Gravity-induced liquid crystal phase transitions of colloidal platelets *J. Chem. Phys.* **121** 5423
- [60] Viveros-Méndez P X, Gil-Villegas A and Aranda-Espinoza S 2014 Monte Carlo computer simulation of sedimentation of charged hard spherocylinders *J. Chem. Phys.* **141** 044905
- [61] Dzubiella J, Schmidt M and Löwen H 2000 Topological defects in nematic droplets of hard spherocylinders *Phys. Rev. E* **62** 5081
- [62] Andrienko D, Germano G and Allen M P 2001 Computer simulation of topological defects around a colloidal particle or droplet dispersed in a nematic host *Phys. Rev. E* **63** 041701
- [63] Gârlea I C, Mulder P, Alvarado J, Dammone O, Aarts D G A L, Lettinga M P, Koenderink G H and Mulder B M 2016 Finite particle size drives defect-mediated domain structures in strongly confined colloidal liquid crystals *Nat. Commun.* **7** 12112
- [64] Monderkamp P A, Wittmann R, Cortes L B, Aarts D G, Smalenburg F and Löwen H 2021 Topology of orientational defects in confined smectic liquid crystals *Phys. Rev. Lett.* **127** 198001
- [65] Takahashi K Z, Aoyagi T and ichi Fukuda J 2021 Multistep nucleation of anisotropic molecules *Nat. Commun.* **12** 5278
- [66] Mederos L, Velasco E and Martínez-Ratón Y 2014 Hard-body models of bulk liquid crystals *J. Phys.: Condens. Matter* **26** 463101
- [67] Trokhymchuk A, Schultz A J and Kofke D A 2019 Alternative ensemble averages in molecular dynamics simulation of hard spheres *Mol. Phys.* **117** 3734
- [68] Dong J, Turci F, Jack R L, Faers M A and Royall C P 2022 Direct imaging of contacts and forces in colloidal gels *J. Chem. Phys.* **156** 214907
- [69] Rex M, Wensink H H and Löwen H 2007 Dynamical density functional theory for anisotropic colloidal particles *Phys. Rev. E* **76** 021403
- [70] Sammüller F and Schmidt M 2021 Adaptive Brownian dynamics *J. Chem. Phys.* **155** 134107

Appendices

A Derivation of the one-body force balance equation

We derive here in detail the one-body force density balance equation for a many-body system of uniaxial interacting particles following Newtonian dynamics. We start by time deriving the current \mathbf{J}

$$\begin{aligned} \dot{\mathbf{J}}(\mathbf{r}, \mathbf{u}, t) = & \left\langle \sum_i \delta(\mathbf{r} - \mathbf{r}_i) \delta(\mathbf{u} - \mathbf{u}_i) \dot{\mathbf{v}}_i \right\rangle + \left\langle \sum_i \delta(\mathbf{u} - \mathbf{u}_i) \frac{\partial \delta(\mathbf{r} - \mathbf{r}_i)}{\partial(\mathbf{r} - \mathbf{r}_i)} \cdot \frac{d(\mathbf{r} - \mathbf{r}_i)}{dt} \mathbf{v}_i \right\rangle \\ & + \left\langle \sum_i \delta(\mathbf{r} - \mathbf{r}_i) \frac{\partial \delta(\mathbf{u} - \mathbf{u}_i)}{\partial(\mathbf{u} - \mathbf{u}_i)} \cdot \frac{d(\mathbf{u} - \mathbf{u}_i)}{dt} \mathbf{v}_i \right\rangle. \end{aligned} \quad (\text{A.1})$$

Multiplying by m , inserting Eqs. (7) and (8), and performing similar steps for the partial derivatives and $\dot{\mathbf{u}}_i$ as those used in the derivation of the continuity equation (26) we find

$$\begin{aligned} m\dot{\mathbf{J}} = & \left\langle \sum_i \delta(\mathbf{r} - \mathbf{r}_i) \delta(\mathbf{u} - \mathbf{u}_i) \mathbf{f}_i \right\rangle - \left\langle \sum_i m \nabla \cdot \mathbf{v}_i \mathbf{v}_i \delta(\mathbf{r} - \mathbf{r}_i) \delta(\mathbf{u} - \mathbf{u}_i) \right\rangle \\ & - \left\langle \sum_i m (\mathbf{u}_i \times \nabla_{\mathbf{u}}) \cdot \boldsymbol{\omega}_i \mathbf{v}_i \delta(\mathbf{r} - \mathbf{r}_i) \delta(\mathbf{u} - \mathbf{u}_i) \right\rangle. \end{aligned} \quad (\text{A.2})$$

Splitting the force acting on particle i

$$\mathbf{f}_i = \mathbf{f}_{\text{ext}}(\mathbf{r}_i, \mathbf{u}_i, t) - \nabla_i U(\mathbf{r}^N, \mathbf{u}^N), \quad (\text{A.3})$$

into an external contribution $\mathbf{f}_{\text{ext}}(\mathbf{r}_i, \mathbf{u}_i, t)$ and an internal contribution $-\nabla_i U(\mathbf{r}^N, \mathbf{u}^N)$, with $U(\mathbf{r}^N, \mathbf{u}^N)$ the total potential energy, and pulling the differential operators of the last two terms on the right hand side of Eq. (A.2) outside of the average yields

$$\begin{aligned} m\dot{\mathbf{J}} = & \left\langle \sum_i \delta(\mathbf{r} - \mathbf{r}_i) \delta(\mathbf{u} - \mathbf{u}_i) \mathbf{f}_{\text{ext}}(\mathbf{r}_i) \right\rangle - \left\langle \sum_i \delta(\mathbf{r} - \mathbf{r}_i) \delta(\mathbf{u} - \mathbf{u}_i) \nabla_i u(\mathbf{r}^N) \right\rangle \\ & - \nabla \cdot \left\langle \sum_i m \delta(\mathbf{r} - \mathbf{r}_i) \delta(\mathbf{u} - \mathbf{u}_i) \mathbf{v}_i \mathbf{v}_i \right\rangle - \hat{\mathbf{R}} \cdot \left\langle \sum_i m \boldsymbol{\omega}_i \mathbf{v}_i \delta(\mathbf{r} - \mathbf{r}_i) \delta(\mathbf{u} - \mathbf{u}_i) \right\rangle. \end{aligned} \quad (\text{A.4})$$

Defining the averages on the right hand side of Eq. (A.4) as the external force density $\mathbf{F}_{\text{ext}}(\mathbf{r}, \mathbf{u}, t)$, the internal force density $\mathbf{F}_{\text{int}}(\mathbf{r}, \mathbf{u}, t)$, the kinetic stress tensor $\boldsymbol{\tau}(\mathbf{r}, \mathbf{u}, t)$, and the coupling tensor $\mathbf{C}(\mathbf{r}, \mathbf{u}, t)$, see Table 1, we obtain the non-equilibrium one-body force density balance equation

$$m\dot{\mathbf{J}} = \mathbf{F}_{\text{ext}} + \mathbf{F}_{\text{int}} + \nabla \cdot \boldsymbol{\tau} - m\hat{\mathbf{R}} \cdot \mathbf{C}. \quad (\text{A.5})$$

B Derivation of the one-body torque balance equation

We derive here the torque density balance equation by time deriving the angular current \mathbf{J}_ω

$$\begin{aligned} \dot{\mathbf{J}}_\omega(\mathbf{r}, \mathbf{u}, t) = & \left\langle \sum_i \dot{\boldsymbol{\omega}}_i \delta(\mathbf{u} - \mathbf{u}_i) \delta(\mathbf{r} - \mathbf{r}_i) \right\rangle + \left\langle \sum_i \boldsymbol{\omega}_i \delta(\mathbf{u} - \mathbf{u}_i) \frac{\partial \delta(\mathbf{r} - \mathbf{r}_i)}{\partial(\mathbf{r} - \mathbf{r}_i)} \cdot (-\mathbf{v}_i) \right\rangle \\ & + \left\langle \sum_i \boldsymbol{\omega}_i \delta(\mathbf{r} - \mathbf{r}_i) \frac{\partial \delta(\mathbf{u} - \mathbf{u}_i)}{\partial(\mathbf{u} - \mathbf{u}_i)} \cdot (-\dot{\mathbf{u}}_i) \right\rangle. \end{aligned} \quad (\text{B.1})$$

By inserting Eqs. (12) and (11) and rewriting the derivative acting on the Dirac distribution, similar to what we have done in the derivation of the continuity equation (26), we obtain

$$\begin{aligned} \dot{\mathbf{J}}_\omega = & \left\langle \sum_i \mathbf{t}_i \cdot \mathbf{I}^{-1} \delta(\mathbf{u} - \mathbf{u}_i) \delta(\mathbf{r} - \mathbf{r}_i) \right\rangle - \left\langle \sum_i \boldsymbol{\omega}_i \delta(\mathbf{u} - \mathbf{u}_i) [\nabla \delta(\mathbf{r} - \mathbf{r}_i)] \cdot \mathbf{v}_i \right\rangle \\ & - \left\langle \sum_i \boldsymbol{\omega}_i \delta(\mathbf{r} - \mathbf{r}_i) [\nabla_u \delta(\mathbf{u} - \mathbf{u}_i)] \cdot \dot{\mathbf{u}}_i \right\rangle. \end{aligned} \quad (\text{B.2})$$

The first term on the right hand side of Eq. (B.2) is proportional to the one-body torque $\mathbf{T}(\mathbf{r}, \mathbf{u}, t)$ containing internal and external contributions. The gradient in the second term can be pulled out of the average. For the third term we insert Eq. (4) and change the order of the triple scalar product. The result is

$$\dot{\mathbf{J}}_\omega = \mathbf{T} \cdot \mathbf{I}^{-1} - \nabla_{\mathbf{r}} \cdot \mathbf{C}^t - \left\langle \sum_i (\mathbf{u}_i \times \nabla_u) \cdot \boldsymbol{\omega}_i \boldsymbol{\omega}_i \delta(\mathbf{u} - \mathbf{u}_i) \delta(\mathbf{r} - \mathbf{r}_i) \right\rangle, \quad (\text{B.3})$$

with the superscript t in \mathbf{C}^t denoting the transposed coupling tensor, see Table 1.

Since there is only a contribution to the average if $\mathbf{u} = \mathbf{u}_i$, we can move the rotation operator $\hat{\mathbf{R}} = \mathbf{u} \times \nabla_u$ outside of the average. We multiply then by the inertia tensor \mathbf{I} on both sides of the equation to obtain

$$\dot{\mathbf{J}}_\omega \cdot \mathbf{I} = \mathbf{T} - \nabla_{\mathbf{r}} \cdot \mathbf{C}^t \cdot \mathbf{I} - \hat{\mathbf{R}} \cdot \left\langle \sum_i \boldsymbol{\omega}_i \boldsymbol{\omega}_i \delta(\mathbf{u} - \mathbf{u}_i) \delta(\mathbf{r} - \mathbf{r}_i) \right\rangle \cdot \mathbf{I}. \quad (\text{B.4})$$

Inserting the definition of the angular kinetic stress tensor and splitting the torque density into external and internal contributions, we finally arrive at the non-equilibrium one-body torque density balance equation

$$\dot{\mathbf{J}}_\omega \cdot \mathbf{I} = \mathbf{T}_{\text{ext}} + \mathbf{T}_{\text{int}} - \nabla_{\mathbf{r}} \cdot \mathbf{C}^t \cdot \mathbf{I} - \hat{\mathbf{R}} \cdot \boldsymbol{\tau}_\omega \cdot \mathbf{I}. \quad (\text{B.5})$$

C Inertia tensor of anisotropic particles

Here, we derive the Hamiltonian for uniaxial particles symmetric around a symmetry axis \mathbf{u} . In the following we omit the particle index for convenience since we focus only on one particle. In order to describe the inertia tensor in a convenient way, we construct a local orthonormal basis with the unit vectors \mathbf{u} , $\hat{\mathbf{e}}_{\dot{\mathbf{u}}} = \dot{\mathbf{u}}/|\dot{\mathbf{u}}|$, and $\hat{\mathbf{e}}_{\mathbf{u} \times \dot{\mathbf{u}}} = \mathbf{u} \times \hat{\mathbf{e}}_{\dot{\mathbf{u}}}$. Note that the last two basis vectors can be chosen from the plane

normal to \mathbf{u} and do not necessarily have to point along $\dot{\mathbf{u}}$. Since the basis unit vectors point along the main axes of the particle, we can write the inertia tensor as

$$\mathbf{I} = I_1 \mathbf{u}\mathbf{u} + I_2 \hat{\mathbf{e}}_{\dot{\mathbf{u}}}\hat{\mathbf{e}}_{\dot{\mathbf{u}}} + I_3 \hat{\mathbf{e}}_{\mathbf{u}\times\dot{\mathbf{u}}}\hat{\mathbf{e}}_{\mathbf{u}\times\dot{\mathbf{u}}}, \quad (\text{C.1})$$

with I_i the moment of inertia corresponding to the respective main axis. Rotations around the symmetry axis \mathbf{u} do not contribute to the equations of motion. Due to the rotational symmetry around \mathbf{u} and the orthonormality of the local basis vectors, it follows that $I_2 = I_3 = I$. Hence, we obtain

$$\mathbf{I} = I_1 \mathbf{u}\mathbf{u} + I(\hat{\mathbf{e}}_{\dot{\mathbf{u}}}\hat{\mathbf{e}}_{\dot{\mathbf{u}}} + \hat{\mathbf{e}}_{\mathbf{u}\times\dot{\mathbf{u}}}\hat{\mathbf{e}}_{\mathbf{u}\times\dot{\mathbf{u}}}), \quad (\text{C.2})$$

and the inverse inertia tensor is then

$$\mathbf{I}^{-1} = \frac{1}{I_1} \mathbf{u}\mathbf{u} + \frac{1}{I}(\hat{\mathbf{e}}_{\dot{\mathbf{u}}}\hat{\mathbf{e}}_{\dot{\mathbf{u}}} + \hat{\mathbf{e}}_{\mathbf{u}\times\dot{\mathbf{u}}}\hat{\mathbf{e}}_{\mathbf{u}\times\dot{\mathbf{u}}}). \quad (\text{C.3})$$

We can also rewrite the angular velocity with the local basis vectors, Eq. (3), as

$$\boldsymbol{\omega} = \mathbf{u} \times \dot{\mathbf{u}} = \dot{u} \hat{\mathbf{e}}_{\mathbf{u}\times\dot{\mathbf{u}}}. \quad (\text{C.4})$$

Hence, the rotational part of the kinetic energy using Eqs. (C.4) and (C.2) is

$$\boldsymbol{\omega} \cdot \mathbf{I} \cdot \boldsymbol{\omega} = \dot{u} \hat{\mathbf{e}}_{\mathbf{u}\times\dot{\mathbf{u}}} \cdot \mathbf{I} \cdot \hat{\mathbf{e}}_{\mathbf{u}\times\dot{\mathbf{u}}} \dot{u} = \dot{u} I \dot{u} = \dot{\mathbf{u}} \cdot \mathbf{I} \cdot \dot{\mathbf{u}}. \quad (\text{C.5})$$

In the following, we consider a many-body system of N uniaxial particles and derive the Hamiltonian. We start with the Lagrangian using Eq. (C.4) to obtain

$$\mathcal{L}(\mathbf{r}^N, \dot{\mathbf{r}}^N, \mathbf{u}^N, \dot{\mathbf{u}}^N) = \sum_i \left(\frac{1}{2} m \dot{\mathbf{r}}_i^2 + \frac{1}{2} \dot{\mathbf{u}}_i \cdot \mathbf{I} \cdot \dot{\mathbf{u}}_i - V_{\text{ext}}(\mathbf{r}_i, \mathbf{u}_i) \right) - U(\mathbf{r}^N, \mathbf{u}^N). \quad (\text{C.6})$$

The canonical momenta of particle i are given by

$$\frac{\partial \mathcal{L}}{\partial \dot{\mathbf{r}}_i} = m \dot{\mathbf{r}} = \mathbf{p}_i, \quad (\text{C.7})$$

$$\frac{\partial \mathcal{L}}{\partial \dot{\mathbf{u}}_i} = \dot{\mathbf{u}}_i \cdot \mathbf{I} = \mathbf{p}_i^{\mathbf{u}}, \quad (\text{C.8})$$

exploiting that \mathbf{I} is symmetric by construction. We finally perform a Legendre transform of the Lagrangian, Eq. (C.6) using the canonical momenta, Eqs. (C.7) and (C.8), to obtain the Hamiltonian

$$\mathcal{H}(\mathbf{r}^N, \mathbf{p}^N, \mathbf{u}^N, \mathbf{p}^{\mathbf{u},N}) = \sum_i \left[\frac{1}{2m} \mathbf{p}_i^2 + \frac{1}{2} \mathbf{p}_i^{\mathbf{u}} \cdot \mathbf{I}^{-1} \cdot \mathbf{p}_i^{\mathbf{u}} + V_{\text{ext}}(\mathbf{r}_i, \mathbf{u}_i) \right] + U(\mathbf{r}^N, \mathbf{u}^N). \quad (\text{C.9})$$

Eidesstattliche Versicherung

Hiermit versichere ich an Eides statt, dass ich die vorliegende Arbeit selbstständig verfasst und keine anderen als die von mir angegebenen Quellen und Hilfsmittel verwendet habe.

Weiterhin erkläre ich, dass ich die Hilfe von gewerblichen Promotionsberatern bzw. -vermittlern oder ähnlichen Dienstleistern weder bisher in Anspruch genommen habe, noch künftig in Anspruch nehmen werde.

Zusätzlich erkläre ich hiermit, dass ich keinerlei frühere Promotionsversuche unternommen habe.

Bayreuth, den

Unterschrift

